Naval Research Laboratory

Washington, DC 20375-5320

Study of Sommerfeld and Phase-Integral Approaches for Green's Functions for PEC-terminated Inhomogeneous Media

Deb Chatterjee
Shaun D. Walker

School of Computing and Engineering
University of Missouri Kansas City
Kansas City, Missouri

January 8, 2010

REPORT DOCUMENTATION PAGE

1. REPORT DATE (DD-MM-YYYY) 08-01-2010	2. REPORT TYPE Memorandum Report	3. DATES COVERED (From - To) Jun 2009 - Aug 2009

4. TITLE AND SUBTITLE

Study of Sommerfeld and Phase-Integral Approaches for Green's Functions for PEC-terminated Inhomogeneous Media

5a. CONTRACT NUMBER

5b. GRANT NUMBER

5c. PROGRAM ELEMENT NUMBER
61153N

6. AUTHOR(S)

Deb Chatterjee and Shaun D. Walker

5d. PROJECT NUMBER

5e. TASK NUMBER
EW021-05-43

5f. WORK UNIT NUMBER
53-9450

7. PERFORMING ORGANIZATION NAME(S) AND ADDRESS(ES)

Naval Research Laboratory
4555 Overlook Avenue, SW
Washington, DC 20375-5320

8. PERFORMING ORGANIZATION REPORT NUMBER

NRL/MR5310--10-9240

9. SPONSORING / MONITORING AGENCY NAME(S) AND ADDRESS(ES)

Naval Research Laboratory
4555 Overlook Avenue, SW
Washington, DC 20375-5320

10. SPONSOR / MONITOR'S ACRONYM(S)
NRL

11. SPONSOR / MONITOR'S REPORT NUMBER(S)

12. DISTRIBUTION / AVAILABILITY STATEMENT

Approved for public release; distribution is unlimited.

13. SUPPLEMENTARY NOTES

14. ABSTRACT

In this report, radiation of sources inside layered media backed by a perfect electric conductor were studied. This problem has practical applications to antennas embedded inside composite material media for many applications. The traditional real-axis integration method was employed with a new formulation for calculating the Sommerfeld integral tail. This new method contains effects of the intrinsic wavenumber of the layer and hence appears physically more suitable for understanding effects of the various layers when the observation point moves in a vertical direction from one layer to the other. In addition, a new algorithm was developed to calculate the proper surface wave poles for electrically thick substrates. The discontinuities in the integrand of the Sommerfeld integral were eliminated upon subtraction of the residues at these poles, and subsequent numerical integration posed no difficulties. Additionally, the problem of stratified media was studied via the phase-integral method. It has been shown that the phase-integral method, with its attendant asymptotic expansions, has the potential for providing much improved solutions to the Green's functions for continuously stratified media by including effects across the Stokes lines.

15. SUBJECT TERMS

Layered media	Phase-Integral	WKB
Sommerfeld integrals	Wentzel-Kramers-Brillouin	

16. SECURITY CLASSIFICATION OF:			17. LIMITATION OF ABSTRACT	18. NUMBER OF PAGES	19a. NAME OF RESPONSIBLE PERSON Michael Kluskens
a. REPORT Unclassified	b. ABSTRACT Unclassified	c. THIS PAGE Unclassified	UL	76	19b. TELEPHONE NUMBER (include area code) (202) 404-1818

CONTENTS

EXECUTIVE SUMMARY

In this investigation the fields due to a current source embedded inside a layered media terminated by a perfectly conducting ground plane was studied by evaluating the Sommerfeld integrals along the real axis. The method consists of locating the proper surface wave poles and then calculating their corresponding residues for subtracting the singular behavior of the integrand at the pole locations. Furthermore, a new and improved closed-form expression to calculate the rapidly oscillatory tail part of the Sommerfeld integral was derived that is specifically more appropriate for piecewise multilayer configurations. The numerical results were included for a single layer substrate that showed marked discontinuous behavior in the G_{zx} component of the dyadic Green's function near the air-to-substrate interface. Results for lateral separations $\rho = 10\lambda, 100\lambda$ are included here. An improved method for determining the initial location of the poles for an electrically thick layered media has been developed. The final location of these poles were refined by the well-known Newton-Raphson method. The Sommerfeld integral evaluation was carried out by assuming that the integrand has simple first order poles. It was however concluded that for stacked piecewise constant layers the numerical determination of the pole locations become numerically difficult as the number of layers increases.

For a piecewise constant multilayered media the G_{zx} Green's function can assume different forms as the observation point moves from one layer to the other. This poses difficulty for real-axis integration because its analytic behavior needs to be examined for "smoothing" out the integrand to facilitate numerical calculation of the Sommerfeld integral tail. The procedure thus becomes very complex if a continuously stratified media is replaced by piecewise constant discrete layered media. An alternative approach, the Phase-Integral method which is based on the Wentzel-Kramers-Brillouin (WKB) method, was investigated and it turned out that its application makes it feasible to calculate the Green's function for both piecewise constant or continuously stratified media. In addition, the Phase-Integral method is valid near "turning" points or equivalently the Stokes lines which are identified as regions of difficulty in numerical calculations. For accurate results via the Phase-Integral method both dominant and subdominant terms need to be included. The subdominant term attains much numerical significance near Stokes lines while the dominant term becomes insignificant in the close vicinity of those regions. New asymptotic techniques which can provide far superior numerical results have also been suggested for future work in relation to application of Phase-Integral methods to layered media problems. An alternate method, the hybrid ray-mode technique, appears to have much potential specifically for problems related to antennas in embedded in layered media. In this method the Green's function is decomposed partly into modes and rays which are mutually related via Fourier transforms. The description in terms of both rays and modes captures the far and near fields of radiating sources, and hence can provide an accurate description of the radiation behavior. For continuously stratified media, the hybrid ray-mode Green's function can incorporate the Phase-Integral solution and thus remains valid near Stokes regions.

The investigations and an extensive survey of the literature suggests that various other techniques such as real-axis integration, discrete complex image method (DCIM), finite-difference time-domain (FDTD), and a host of asymptotic techniques are necessary to solve the problem. The DCIM and FDTD have the virtue of generating reference solutions for appropriate cases of interest. The asymptotic techniques are

useful but care must be exercised in their mathematical development. In this context it was found that the existing asymptotic solutions for Sommerfeld integrals are limited in applicability because of the manner in which they were derived in the first place. Improved methods for obtaining more general solutions have been identified. Finally some recommendations have been included in this report to justify further investigations in this area.

STUDY OF SOMMERFELD AND PHASE-INTEGRAL APPROACHES FOR GREEN'S FUNCTIONS FOR PEC-TERMINATED INHOMOGENEOUS MEDIA

1. INTRODUCTION

Electromagnetic and acoustic wave propagation in layered media, an intensely studied topic [1-7], still finds application in many problems such as microstrip antennas [8-13]. A survey of the relevant research work shows that the general aspects of modeling wave propagation in layered media has been treated by the Sommerfeld approach [11-13] for antenna problems, or via the Phase-Integral [14-24] and Wentzel-Kramers-Brillouin (WKB) techniques for microwave propagation in ionospheric and inhomogeneous media [25]. Approaches similar to the Phase-Integral and WKB techniques have been studied for determining the resonant characteristics of seismic wave propagation [26-28]. The subject of this investigation is to examine the various methods for determining electromagnetic wave propagation in layered media with a particular emphasis on Sommerfeld and Phase-Integral approaches.

The problem of interest is shown in Fig. 1. The situation depicted here could mimic the case of embedded antennas on tactical platforms that are physically concealed by reducing physical visibility. Since such embedded antennas radiate from within composites or other materials the radiation mechanism can be understood by a full-wave analysis including the effects of the layered structure. Antenna arrays #1 and #2 contain aperture elements that radiate from within a continuous vertically stratified media media backed by a perfect electric conductor. As a result the intrinsic propagation constant changes continuously for $z \leq H$ and has a constant value of k_0 for $z \geq H$. This abrupt change in the propagation constant causes the wave behavior to change abruptly at the height $z = H$.

From an analysis viewpoint, layered media propagation has been treated adequately for single layer microstrip antenna problems [11-13] where one media is a lossy, non-magnetic dielectric and the other is free space. The full-wave solution, based on the Green's function method, shows that the air-dielectric interface acts a guiding structure for surface waves. The complete solution is described as inverse Fourier transforms, also known as Sommerfeld integrals. However, the dielectric media was assumed to have constant permittivity and not continuously stratified as in the problem of interest. Calculation of the Sommerfeld integrals is a century-old problem and research work is still continuing into its evaluation with consideration to this particular physical problem.

The most significant difficulty with calculation of the Sommerfeld integrals is that in the neighborhood of the plane containing the source, the integrand in the Sommerfeld integral is weakly convergent and oscillatory. The oscillations of the integrand is pronounced as the lateral separation between the source and observation point increases. In addition, the location in the complex spectral plane of the poles of this integrand complicate the numerical calculation. For a single layer problem, as in microstrip antennas, a very good discussion on such issues can be found in Ref. [12].

Figure 2 describes an "equivalent" problem for Fig. 1. In this situation the radiation from any one of the arrays in Fig. 1 is modeled by the equivalent currents placed on a box with 5 sides. The continuously
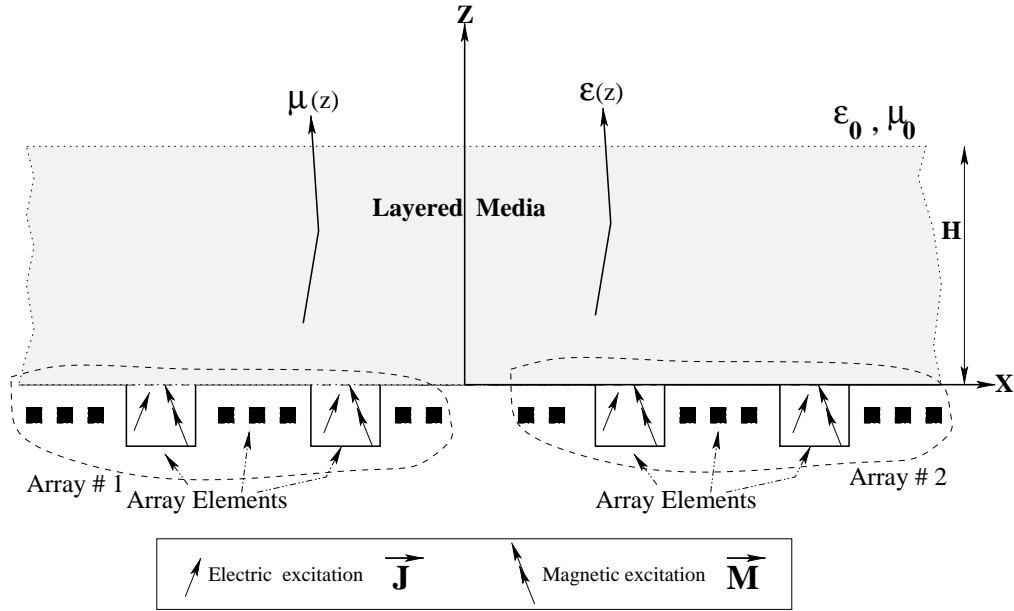
Fig. 1 — Two electrically large arrays #1 and #2 radiating from an infinite ground plane in presence of a continuous vertically stratified media of thickness H, permittivity $\varepsilon(z)$, and permeability $\mu(z)$. The characteristic wavenumber of the continuously stratified medium is $k(z) = \omega\sqrt{\varepsilon(z)\mu(z)}$. Note that the intrinsic wavenumber is $k_0 = \omega\sqrt{\varepsilon_0\mu_0}$ for $z \geq H$, where $\varepsilon_0 = 8.854185 \times 10^{-12}$ Farads/meter and $\mu_0 = 1.256 \times 10^{-12}$ Henries/meter are the constitutive parameters of free-space.
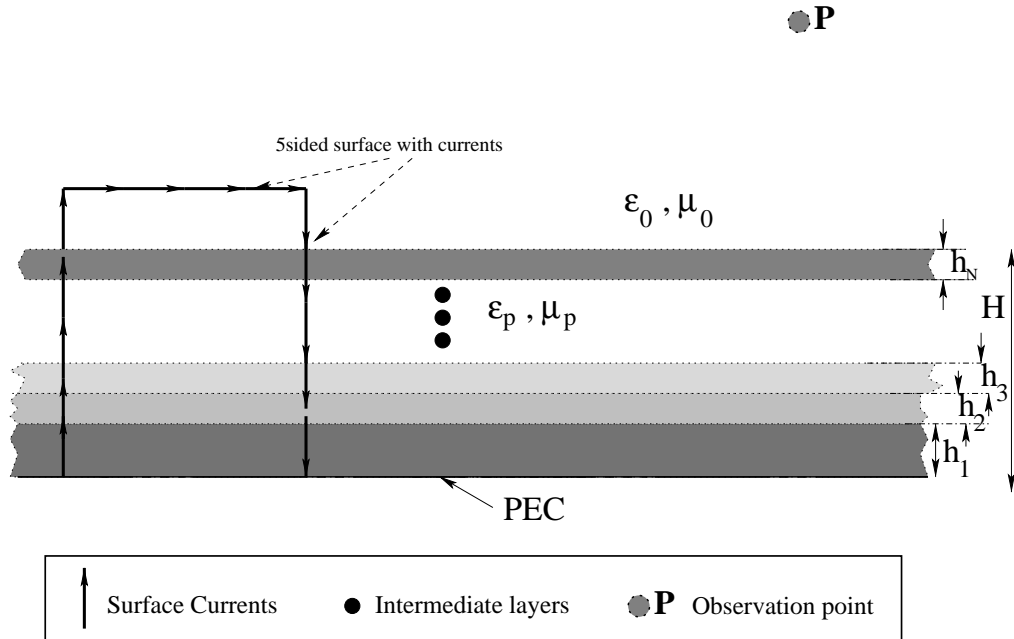
Fig. 2 — Representation of the continuously stratified media by discrete slabs of finite thicknesses. The radiating array has been replaced by a equivalent region of five surfaces with radiating currents on the surfaces. Portions of the region can extend beyond the layered region.

stratified (or layered) media in Fig. 1 is replaced by multiple slabs of varying thicknesses and each with different but constant permittivity and permeability. The observation point, P, is now arbitrarily located as shown in Fig. 2. Thus, to calculate the field at P due to equivalent currents, one needs to find the Green's function for a multilayered media where the number of layers could possibly be large but finite. The propagator (otherwise known as the Green's function) for this discrete multilayer topology has been reported to be a good approximation to the actual layered media which is continuously stratified [1].

Unfortunately, for more than two layers the mathematical form of the Green's function turns out exceedingly complex [2, 11]. In fact, as the point P moves from inside the layered media, crossing the various layers and into free-space, the Green's function (which also contains the Sommerfeld integral) changes [2]. This change is effected by the change in the integrand of the Sommerfeld integral, and hence the Green's function. Thus one of the primary difficulties in calculating the multilayered Green's function is the necessity of accurately calculating the multiple Sommerfeld integrals that result when one approximates a continuously stratified media by discrete layers.

The solution to the Green's function for a continuously stratified media can be obtained by the WKB [1-3] or equivalently Phase-Integral [16-18] methods. The Phase-Integral method solves the one-dimensional wave equation, representative of the direction of stratification, by considering "turning points." Physically, the one-dimensional wave equation is equivalent to that of a one-dimensional, non-uniform transmission line. Methods of obtaining the solutions have been rigorously developed in Refs. [16-20]. Compared to the discrete multilayer approximation of the continuously stratified media, the Green's function directly obtained for a continuously stratified media does not assume various different forms. However, to account for continuous uniaxial stratifcation, special *non-elementary* functions [17] appear inside integrand of the Green's function (the Airy functions themselves exhibit completely different behavior for positive and negative real arguments and hence appear appropriate to describe wave propagation in such situations). Depending on the nature of the stratification, the Phase-Integral solution [16] may contain other non-elementary forms such as Weber's parabolic cylinder or Whittaker's confluent hypergeometric functions [18, 20].

From a computational viewpoint handling one single Green's function accounting for continuous stratification is not much more complicated than evaluating several Green's functions for discrete multilayered media. This perspective suggests that a comparison between the two approaches be done for an appraisal of the various approaches. To that end, the primary purpose of this investigation is to compare Green's functions containing the Sommerfeld integral for discrete multilayered media versus the actual Green's function for a continuously stratified media.

The earliest application of Sommerfeld theory to submarine communication was reported in Ref. [29]. The radiation behavior of a dipole immersed inside sea-water (a conducting medium) was explained by the behavior of the Sommerfeld integral about the branch-cut. This problem was especially distinct from the traditional Sommerfeld solution [30]. Computational strategies for electromagnetic wave propagation in multilayered media and structures depends heavily on analytic approaches [31-32]. In fact, the method of moments formulation as outlined in Refs. [33, 34] emphasizes the importance of the analytic form of the multilayered Green's function, because analytic approaches provide substantial savings in computational resources. In Ref. [35] the analytic approach to Green's function formulation for various electromagnetic boundary value problems is available. The focus of Ref. [35] is to develop a electric network approach in deriving the Green's functions. This is accomplished by synthesizing the three-dimensional Green's function from its three one-dimensional Green's functions. These one-dimensional Green's functions are the solutions to the one-dimensional Sturm-Liouville problems. In Ref. [35] the one-dimensional Green's

functions are interpreted as solutions to the transmission line equations [36, chap. 7; 37, chap. 8]. The final methodology involves use of a double contour integral [35, p. 285, Eq. 37; 38, p. 86, Eq. 76]. This "network" approach is particularly helpful for stratified or piecewise constant media, and is the preferred approach studied here in Chapter 3.

Some relevant work involving the Green's function for layered media [31, 32] involves asymptotic evaluation of integrals of the various inverse-Fourier transforms. Such methods traditionally involve rigorous application of analytic function theory to boundary value problems. General methods of treating various boundary value problems in acoustic [4] and oceanic [5] media can generally be found in Refs. [39-46] which also includes various useful practical techniques of asymptotic evaluation of integrals [42, 43] for numerical calculation of the Green's functions.

The study of efficient numerical approaches for calculation of the Green's function for microstrip and other layered media has been studied extensively. The selected Refs. [47-59] contain information of continuing importance. The information gleaned from these sources indicate considerable effort in the direct numerical calculation of the Sommerfeld integral without resorting to approximate (asymptotic) techniques [31, 32]. In particular, the real axis integration of Sommerfeld integrals [56, 57] is extensively employed in Chapter 2 for the numerical calculation of the Green's function for the vertical electric field of a horizontal electric dipole (G_{zx}). The difficulty of real axis integration is realized when the relative vertical separation between source and observer locations decreases. This difficulty is further compounded by the fact that for mutual coupling between elements in a microstrip antenna array, the lateral separation could be very large and oscillatory behavior of the integrand in the Sommerfeld integral causes divergence. To that end Ref. [51] has developed some closed form approaches for calculation of the "infinite" tail part of the Sommerfeld integral but the approach applies to piecewise constant media and is limited by the fact that when the observation point moves vertically from one layer to the other (see Fig. 2) the changes in electrical characteristics due the different individual discrete layers is not properly captured. Various closed form results involving Bessel functions [60] with judicious choice of numerical integration [61] and formulas for Laplace transforms [62] appear useful in numerical calculation for multilayer problems.

In contrast to the direct numerical calculations, such as in Ref. [57], computationally efficient forms for Sommerfeld integrals for specialized source and observer locations have been developed for PEC-backed single and double layer dielectric substrates [63-65]. Though these are of limited utility, they are computationally extremely efficient within their domains of validity. In particular the result in Ref. [63] has been reported to reduce the computational time of a full-wave Method of Moments (MoM) formulation by several orders of magnitude when applied to electrically large microstrip arrays that have very widely separated elements. However, these solutions cannot be generalized to arbitrary topologies as was observed in Refs. [31, 32]. The other limitation of these asymptotic solutions is that they do not apply to multilayer media having more than two layers with arbitrary electrical constitutive parameters. In fact, the double layer solution in Ref. [64] has restrictions on the relative vertical separations between source and observer locations. Regardless of these restrictions, as noted in Ref. [34], unless some form of analytic reduction is worked out for the Sommerfeld integrals a MoM strategy becomes computationally expensive particularly at high-frequencies.

An interesting approach, the Discrete Complex Image Method (DCIM) [66-68], formally avoids the direct calculation of the Sommerfeld integrals because it uses the Sommerfeld-Weyl identity and after some mathematical manipulations expresses the entire result as a finite series of exponentials. The coefficients of the series are calculated by the matrix pencil method in Refs. [67, 68] based on Ref. [59]. This is a particularly appealing alternative and appears to have much promise in solving multilayer problems. However, the

extension of DCIM to continuously stratified media does not appear to be available. The DCIM approach can furnish the reference solution which can be compared to solutions from other analytically-dominant techniques. A review of other recent approaches reported in Refs. [69-73] suggests a renewed emphasis on obtaining closed-form solutions. However, it is interesting to note that closed-form solutions can also be complicated in their mathematical form and may require evaluation of Lipschitz-Hankel integrals. Also, Refs. [66-73] do not address the continuous stratification case.

For either real-axis integration or asymptotic evaluation of Sommerfeld integrals there exists poles in the integrand whose location and residues need to be evaluated. The technique pursued in Chapter 2 utilizes the calculation of the residues upon locating the poles for direct numerical calculation of the Sommerfeld integral (this technique is based on the approach suggested in Ref. [12]). To that end, there are various considerations regarding the type of the pole. Most of the research has centered around microstrip antennas which are electrically thin planar topologies. As discussed in Refs. [6, 12, 13] there exists one proper TM surface wave pole, because the thickness of the PEC-backed substrate for microstrip problems is around $0.01\,\lambda$. However, as the thickness increases the number of poles that need to be considered increases. Additionally, for asymptotic evaluation of Sommerfeld integrals [63-65] the real-axis contour is deformed and made to pass from the top (proper) to the bottom (improper) Riemann sheet, because of the presence of a branch cut at the free-space wavenumber k_0. In doing so improper poles lying on the bottom sheet may be captured or crossed by the steepest descent path. The residues at these improper poles are needed for accurate evaluation. Thus pole location plays a very important role and representative techniques are reported in Refs. [74-79]. However, for electrically thick substrates the information in Ref. [52] appears very relevant. Sophisticated techniques have been reported in Ref. [75] but as expected its implementation can consume significant computation times.

For layered media a computationally efficient form the Green's function is available in Refs. [80-85]. This technique synthesizes the Green's function in terms of finite number of rays and modes through the use of the Poisson sum formula. The process involves asymptotic evaluation of integrals [42, 43]. This ray-mode approach in deriving the Green's function appears physically most appealing for layered media because a layered media can have various types of modes (trapped, surface, leaky, lateral waves) plus rays. Often one form (ray or mode) is inadequate and a combination of both is therefore a judicious choice. This ray-mode approach has been pursued for only few practical problems in Ref. [85] and hence it would be worth investigating its application to the topology shown in Fig. 1.

Finally, Refs. [86-100] provide new aspects on asymptotic evaluation of integrals, which are at the heart of development of computationally efficient techniques for layered media problems. The information in these papers is more advanced than that available in Refs. [42, 43]. The reason is that a new technique *hyperasymptotics* has been developed in Refs. [88, 90, 95] whose salient feature is to provide numerical accuracy. In the past the techniques in Refs. [42, 43] focused on obtaining closed-form solution to the various integrals without considering the accuracy of the final result. Thus, discrepancies could not be easily explained when numerical comparisons were performed between exact and asymptotic solutions. Often the errors could not be accounted for because of mathematical intractability. The information in Refs. [99, 100] specifically addresses this problem. It is shown that the numerical errors in asymptotic expansion happen around Stokes lines when the dominant and subdominant solutions interchange roles. These references are included here because of their potential utility in future investigations.

The contents and contributions of the various chapters in this report are briefly discussed next. In Chapter 2, a *new improved* method for direct real-axis integration of Sommerfeld integral tail is developed. Unlike

Ref. [51], this method can be applied to discrete multilayer media and this approach can accurately capture the physical characteristics of the problem. This chapter contains implementation of the algorithm utilizing the information in Ref. [52] to locate the proper surface wave poles (for real-axis integration, the path of integration stays always on the top sheet which is why only proper surface wave poles that satisfy Sommerfeld radiation condition need to be considered).

In Chapter 3, the overall approach to the continuously stratified media is developed following contour integral representations [35]. The WKB and Phase-Integral solutions for the characteristic Green's function along the z-stratification is discussed primarily from the information available in Ref. [17]. It is shown through some simple examples that the Phase-Integral method is a general case when conventional WKB solutions fail at the turning points. The situation is salvaged by generalizing the solution to include non-elementary special functions [16-20] that remain valid at the turning points and reduce to the conventional WKB solutions when the observation point moves away from the turning points (or Stokes lines). The complete specific solution is not obtained but the overall approach is discussed here.

Chapter 4 discusses the various approaches and contains suggestions regarding future work. This is followed by conclusions of this investigation and an extensive list of references followed by some important appendices relevant to the various aspects of the information in this report.

2. G_{zx} GREEN'S FUNCTION FOR SINGLE AND DOUBLE LAYER PEC-TERMINATED MEDIA

In this chapter the G_{zx} Green's function for single and double layer PEC-terminated substrates, shown in Fig. 3, is calculated for large lateral separations. The calculations follow the traditional real axis integration of Sommerfeld integrals [11, 56-59] as shown in Fig. 4 without any recourse to special contour deformations or asymptotic formulations [55, 63-65]. The advantage of real axis integration is that the process is tractable. However, for extremely large lateral separations on the order of thousands of wavelengths the existing methods involving real axis integration become numerically unstable. This is due to the divergent oscillatory behavior of the Sommerfeld integrand. The convergence behavior becomes very slow when the observation point is close to the interfaces in Fig. 3.

The scope of the numerical results is limited to the calculation of only the G_{zx} component of the dyadic Green's function for single layer media. Specific numerical results for the double layer media could not be included due to time constraints. The results were generated using the software *MATHEMATICA* for the purpose of demonstrating the feasibility of real-axis integration for large lateral separations. In general, the dyadic Green's function due to a horizontal electric dipole has nine components. For a multilayer media, each of these components has complicated mathematical forms due to the presence of the infinite integrals involving Bessel function plus multilayer effects in the integrand. To explicitly evaluate all the nine components of the Green's function is therefore a formidable task and for that reason attention is directed in this report to illustrate the features of the general method of computation for the G_{zx} component only.

The primary objective is to generate a reference solution for G_{zx} which can be compared against various other techniques to be investigated later. The present method of real-axis integration for calculating the single and double layer G_{zx} Green's function component involves the following steps:
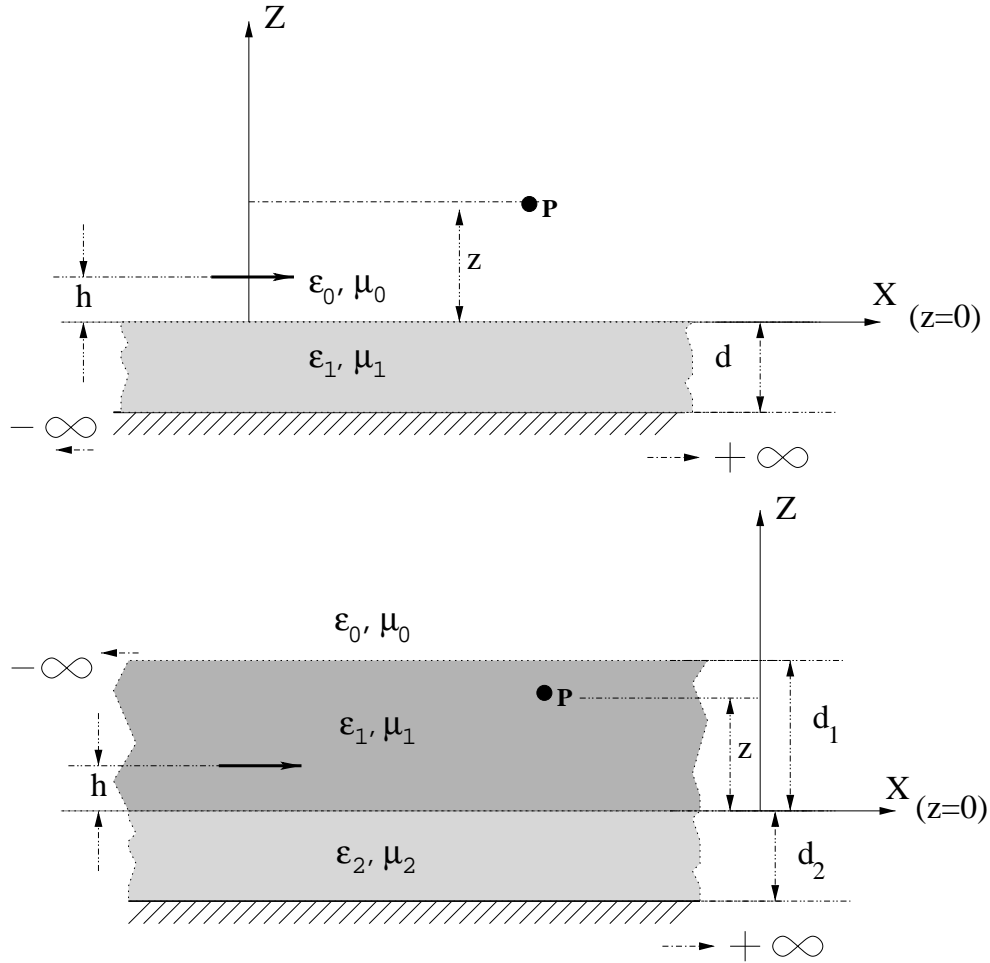
Fig. 3 — A $\hat{x}$ oriented horizontal electric current element (Hertzian dipole) radiating on the air-dielectric interface of a single layer and from inside a double layer media, both terminated by a PEC ground plane.

(1) Divide the real-axis integration into three distinct regions: (a) $0 \leq \xi \leq k_0$, (b) $k_0 \leq \xi \leq \xi_A$, and (c) $\xi_A \leq \xi < +\infty$. Determination of the "breakpoint" ξ_A [57] is most critical for real axis integration (discussed later in this chapter).

(2) Locate the *proper* surface wave poles that are close to the integration path on the real axis, calculate the residues at these poles, and subtract the effects of the pole singularities from the original Sommerfeld integrand. These proper surface wave poles lie in region (b) of step (1).

(3) Identify the asymptotic behavior of the Sommerfeld integrand for the spectral variable $\xi \to +\infty$; it turns out that the asymptotic behavior is appropriate in region (c) of step (1). This is called the "tail" part of the integration which can be evaluated analytically. This further comprises of the following steps, assuming the determination of the "breakpoint" ξ_A [57], as below:

   (a) Numerical integration of the portion of the tail from $\Re e(k_1) \leq \xi \leq \xi_A$

   (b) Analytic, closed-form integration of the remainder of the "tail" from $\xi_A \leq \xi \leq +\infty$.
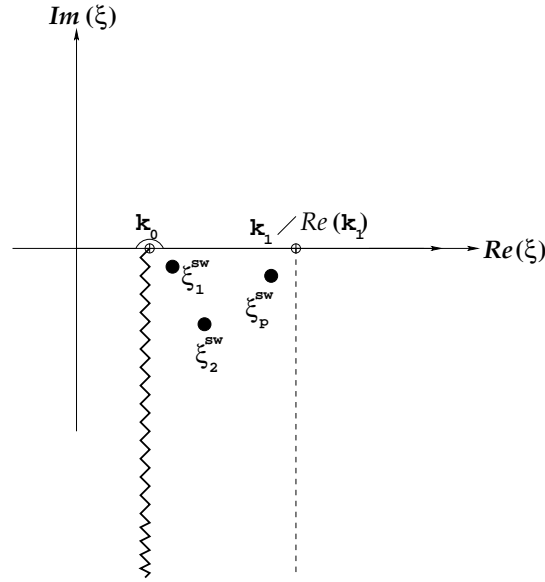
Fig. 4 — Sommerfeld contour for $\Re e(\xi)$ integration. The path of integration always stays on the top (proper) Riemann sheet. All poles of the Sommerfeld integrand for G_{zx} lie with the range: $k_0 \leq \xi \leq \Re e[k_0\sqrt{\varepsilon_r}]$. These poles, denoted by $\xi_{1,2,\cdots,p}^{\text{sw}}$ in the figure, lie on the top (proper) sheet and hence are proper surface wave poles satisfying the Sommerfeld radiation condition.

These aspects are detailed in the sections below. The discussion begins with a single layer PEC-terminated substrate followed by the double layer problem.

2.1   Analytic Nature of the G_{zx} Green's function

This section begins with the formulas for the G_{zx} Green's function for a single layer followed by a double layer geometry. The objective is to identify the analytic nature of the Sommerfeld integrands. No attempt is made to perform contour deformation subsequently followed by steepest-descent methods traditionally found in the literature. Instead, our primary focus is on real-axis integration of the Sommerfeld integral [56]. The real-axis integration will have only proper surface wave poles lying on the proper Riemann sheet, *i.e.*, the sheet on which the Sommerfeld radiation condition is satisfied. The leaky-wave poles, which do not satisfy the Sommerfeld radiation condition, are not encountered when performing real-axis integration because the real-axis integration range, *viz.*, $0 \leq \xi \subset \infty$, *always* stays on the top (proper) Riemann sheet.

However, asymptotic formulations, especially like Refs. [63, 64], do consider leaky-wave poles which lie on the bottom (or improper Riemann sheet). These improper leaky wave poles do not satisfy the well-known Sommerfeld radiation condition, but are encountered when the real-axis is deformed across branch cuts so these poles are encountered. The steepest descent contour in Ref. [63] must cross the branch cut and hence has to traverse from the top to the bottom and back to the top sheet in a two-sheeted Riemann surface. In such a traversal, the steepest descent path encroaches improper poles of the Sommerfeld integrand that lie on the bottom sheet. The authors of Ref. [63], in their development of an uniform asymptotic formulation, considered improper poles that come close to the saddle point for the special location when both the source and observer points are exactly on the air-dielectric interface.

The limitation of the preceding approach and the ones pursued here is that we assume that the poles of the Sommerfeld integrand are *simple, first order* type. Majority of the literature on pole location in layered media [6, 10-12, 74-79] involving evaluation of Sommerfeld integrals is restricted to microstrip antenna problems. Recent work in Ref. [79] is related to the development of an algorithm for pole locations in a planarly layered media close to the topology in Fig. 3, but with no PEC termination. The information gleaned from Ref. [79] indicates that locating poles (of all orders and types) in a layered media is still a subject of continuing investigation.

Normally the thickness of microstrip antennas is less than 0.1 λ and for real-axis integration only one proper surface wave pole is adequate in most cases [55, 56]. However, for arbitrary electrically thick layered media such simplifications are inadmissable. Unfortunately, due to limitations in available resources, we have not investigated in detail the nature of the poles for single and double layer substrates for arbitrary electrical thickness and constitutive electrical properties.

2.1.1 G_{zx} Green's function for a Single Layer PEC-backed Substrate

The G_{zx} Green's function for the single layer geometry shown in Fig. 3 is directly obtainable from Ref. [10, pp. 53-54]. For a horizontal electric dipole, oriented along the x-axis and located at the origin one can write

$$\vec{J} = \hat{x} I_0 \Delta l \, \delta(x) \delta(y) \delta(z) = \hat{x} p_x \delta(x) \delta(y) \delta(z). \tag{1}$$

The z-components of the electric fields generated by Eq. (1) are different in different layer regions in Fig. 3. In Eq. (1), $\hat{x} p_x = \hat{x} I_0 \Delta l$ is the electric current moment. The fields can be calculated by obtaining the scalar Green's function [35, chaps. 2, 3, 5]. The representation of the fields relating the propagator (Green's function) matrix to the source Eq. (1) is given by

$$\begin{bmatrix} E_{xx} \\ E_{yx} \\ E_{zx} \end{bmatrix} = -jk\eta_0 \begin{bmatrix} G_{xx} & G_{xy} & G_{xz} \\ G_{yx} & G_{yy} & G_{yz} \\ G_{zx} & G_{zy} & G_{zz} \end{bmatrix} \bullet \begin{bmatrix} p_x \\ 0 \\ 0 \end{bmatrix} \tag{2}$$

where (E_{xx}, E_{yx}, E_{zx}) is the electric field generated by a x-directed horizontal electric dipole. The z-component of the electric field, E_{zx}, radiated by a $\hat{x}$ oriented horizontal electric dipole, for both single and double layer PEC-backed substrates are available in Ref. [10, pp. 53-54, Eqs. 3.3-3.16]. From these expressions, the corresponding G_{zx} Green's function can be easily found using Eq. (2). For a single layer dielectric with the horizontal electric dipole at the air-dielectric interface and field point in air as in Fig. 3 this reads as follows

$$G_{zx}^0 = \frac{j}{2\pi k_0^2} \cos\phi \int_0^{+\infty} \xi^2 J_1(\rho\xi) e^{-j\kappa_0|z|} \left[\frac{\kappa_1 \tan(\kappa_1 d)}{\varepsilon_{r1}\kappa_0 + j\kappa_1 \tan(\kappa_1 d)} \right] d\xi, \quad \text{for } 0 \le z \le +\infty, \tag{3}$$

and for the field point inside the substrate the same Green's function takes the form

$$G_{zx}^1 = \frac{-j\varepsilon_{r1}}{2\pi k_0^2} \cos\phi \int_0^{+\infty} \xi^2 J_1(\rho\xi) \left[\frac{\cos(\kappa_1[d-|z|])}{\cos(\kappa_1 d)} \frac{\kappa_0}{\varepsilon_{r1}\kappa_0 + j\kappa_1 \tan(\kappa_1 d)} \right] d\xi, \quad \text{for } -d \le z \le 0. \tag{4}$$

In Eqs. (3) and (4), the z-directed propagation constants are

$$
\kappa_m = \begin{cases} \sqrt{k_m^2 - \xi^2}, & \text{for } k_m \geq \xi, \\ -j\sqrt{\xi^2 - k_m^2}, & \text{for } \xi \geq k_m. \end{cases} \tag{5}
$$

In Eqs. (3–5), $m = 0$ and 1 designate the location of field points in air and inside the substrate, respectively. We note that $k_0 = \omega\sqrt{\varepsilon_0 \mu_0}$ is the instrinsic wavenumber in air and $k_1 = k_0\sqrt{\varepsilon_{r1} \mu_{r1}}$ is the intrinsic wavenumber inside the substrate. The relative permittivity and permeability of the substrate are ε_{r1} and μ_{r1}, respectively. In this report, and specifically in this chapter, we have chosen a non-magnetic lossy dielectric substrate ($\mu_{r1} = 1$, $\varepsilon_{r1} = |\varepsilon_{r1}|[1 - j\tan\delta]$). The loss tangent of the dielectric is $\tan\delta$.

It is interesting to note that as the observer point P moves from inside the substrate ($m = 1$) into the air ($m = 0$), the form of the Green's function changes. The surface wave poles lie in the range $k_0 \leq \xi \leq \Re e(k_1)$. This aspect is discussed in Refs. [6, 7, 11, 38]. However, when $\xi \geq k_0$, we have $\kappa_0 = -j\sqrt{\xi^2 - k_0^2}$, but $\kappa_1 = \sqrt{k_1^2 - \xi^2}$. Substituting these in the denominators in Eqs. (3) and (4), one notes that the *proper* surface wave poles are given by the roots of

$$
D_{\text{TM}}(\xi) = -\varepsilon_{r1}\sqrt{\xi^2 - k_0^2} + \sqrt{k_1^2 - \xi^2}\tan[d\sqrt{k_1^2 - \xi^2}] \equiv 0. \tag{6}
$$

Solutions to Eq. (6) are discussed in the next section for the single layer case.

The integrands in Eqs. (3) and (4) have branch points defined by $\kappa_{0,1} = 0$. But due to the presence of the factor $\kappa_1 \tan(\kappa_1 d)$ in both numerators and/or denominators in Eqs. (3) and (4), near $\kappa_1 \approx 0$ the term $\kappa_1 \tan(\kappa_1 d) \approx d\kappa_1^2 = d(k_1^2 - \xi^2)$; this indicates that the product is an *even* function of the spectral parameter ξ near the branch point located at $\xi = \pm k_1$. The even function nature indicates that the near the branch point $\xi = \pm k_1$ the multivalued nature is non-existent. Consequently, the branch point at $\kappa_1 = 0$ doesn't contribute to any specific analytic singularity. However, additional inspection of the nature of the integrands in Eqs. (3) and (4) shows that the branch point at $\xi = \pm k_0$ does contribute, and is the only contributing branch point singularity. Finally, the existence of the cosine functions in Eq. (4) indicates that they are even functions near $\kappa_1 = 0$ branch point locations and thus their ratio is *not* multivalued near the branch point at $\xi = \pm k_1$. Next, we investigate the asymptotic behavior of the Sommerfeld integrand as $\xi \to +\infty$.

To that end, the integrands in Eqs. (3) and (4) are identified as products of "slab" terms and a spatial function involving lateral separation between observation and source location.

$$
\overline{\mathscr{F}}_{zx}^{0,1} = \xi^2 J_1(\xi\rho) \times \begin{cases} e^{-j\kappa_0|z|}\overline{\mathscr{T}}_s^0(\xi, d), & \text{point P in Fig. 3 in air,} \\ \frac{\cos[\kappa_1(d-|z|)]}{\cos(\kappa_1 d)}\overline{\mathscr{T}}_s^1(\xi, d), & \text{point P in Fig. 3 inside substrate.} \end{cases} \tag{7}
$$

The slab functions in Eq. (7) are defined as

$$
\overline{\mathscr{T}}_s^{0,1}(\xi, d) = \begin{cases} \frac{\kappa_1 \tan(\kappa_1 d)}{D_{\text{TM}}(\xi)}, & \text{point P in Fig. 3 in air,} \\ \frac{\varepsilon_{r1}\kappa_0}{D_{\text{TM}}(\xi)}, & \text{point P in Fig. 3 inside substrate.} \end{cases} \tag{8}
$$

The denominator, $D_{TM}(\xi)$, in Eq. (8) is defined in Eq. (6) for $\xi \geq k_0$, or can be identified easily from the term common to the denominators in Eqs. (3) and (4).

The choice of the breakpoint, ξ_A, is determined by the asymptotic nature of the integrand in Eqs. (7) and (8) that dominates beyond $\xi \geq \xi_A$. In Ref. [57] the asymptotic nature of the Bessel function was utilized for the weighted average algorithm to calculate the tail part beyond the breakpoint. The objective in Ref. [57] was to capture the oscillatory behavior of the integrand in the Sommerfeld integral (for $\xi \to \infty$) and thus evaluate the tail in closed form. Also, the oscillatory behavior of the Bessel function was subtracted out from the original integrand and a subsequent smoother function was used for numerical integration in the range $0 \leq \xi \leq \xi_A$. In this report, the Bessel function is retained as it is, but the $\overline{\mathscr{T}}_s^{0,1}(\xi, d)$ slab functions are approximated for $\xi \to \infty$. A closed form result is subsequently obtained following some simple manipulations, using a variant of the Sommerfeld-Weyl identity derived in Appendix A.

From Eq. (5) it follows that as $\xi \to \infty$, $\kappa_{0,1} \to -j\xi$, and hence $\tan(\kappa_1 d) \approx \tan(-j\xi d) = -j\tanh(\xi d)$. Further, for $\xi \to \infty$, one has $\tanh(\xi d) \approx 1$. Using these results (valid for $\xi \geq \xi_A^m$) one has the following "asymptotic" forms for the slab functions in Eq. (8)

$$\overline{\mathscr{T}}_s^m(\xi \to \infty, d) = \begin{cases} \dfrac{-j\xi \times -j}{\varepsilon_{r1} \times -j\xi + j \times -j\xi \times -j} \equiv \dfrac{-j}{\varepsilon_{r1}+1}, & m = 0 \text{ point P in Fig. 3 in air,} \\[2mm] \dfrac{\varepsilon_{r1} \times -j\xi}{\varepsilon_{r1} \times -j\xi + j \times -j\xi \times -j} \equiv \dfrac{\varepsilon_{r1}}{\varepsilon_{r1}+1}, & m = 1 \text{ point P in Fig. 3 inside substrate.} \end{cases} \tag{9}$$

From Eq. (9) one may therefore define the following constants

$$\overline{\mathscr{K}}_m^\infty = \overline{\mathscr{T}}_s^m(\xi \to \infty, d) = \frac{1}{\varepsilon_{r1}+1} \times \begin{cases} -j, & m = 0 \text{ point P in Fig. 3 in air,} \\[2mm] \varepsilon_{r1}, & m = 1 \text{ point P in Fig. 3 inside substrate.} \end{cases} \tag{10}$$

The interesting aspect is that in Eq. (10) the $\overline{\mathscr{K}}_m^\infty$ changes *discontinuously*. This can be understood if one considers ε_{r1} for a pure real - lossless substrate. As the observation point P moves from inside the substrate to air, the constant in Eq. (10) changes from pure real to imaginary for lossless ε_{r1}. This happens rapidly across the air-substrate interface and is also known as a manifestation of the Stokes phenomenon [88, 89]. For $\xi \geq \xi_A$, via analytic continuation one then has

$$e^{-j\kappa_0|z|} \equiv e^{-|z|\sqrt{\xi^2-k_0^2}},$$

$$\frac{\cos[\kappa_1(d-|z|)]}{\cos(\kappa_1 d)} = \frac{\cosh[\sqrt{\xi^2-k_1^2}(d-|z|)]}{\cosh[d\sqrt{\xi^2-k_1^2}]}. \tag{11}$$

In Eq. (11), set $t = d - |z|$, and note that $t \geq 0$. Using the definitions of hyperbolic functions

$$\cosh[t\sqrt{\xi^2-k_1^2}] = \frac{1}{2}\left\{\exp(t\sqrt{\xi^2-k_1^2}) + \exp(-t\sqrt{\xi^2-k_1^2})\right\}$$

$$\approx \frac{1}{2}\exp(t\sqrt{\xi^2-k_1^2}), \qquad \text{since } t \geq 0 \text{ and } \xi \to \infty,$$

$$\cosh[d\sqrt{\xi^2-k_1^2}] \approx \frac{1}{2}\exp(d\sqrt{\xi^2-k_1^2});$$

therefore,

$$\frac{\cos[\kappa_1(d-|z|)]}{\cos(\kappa_1 d)} \approx e^{-|z|\sqrt{\xi^2-k_1^2}}. \tag{12}$$

Finally, for the full integrand given in Eq. (7) one can "extract" the asymptotic behavior using Eqs. (10) and (12)

$$\overline{\mathscr{F}}_{zx}^{m}(\xi \geq \xi_{A}^{m}) \approx \overline{\mathscr{K}}_{m}^{\infty}[\xi^2 J_1(\xi\rho)e^{-|z|\sqrt{\xi^2-k_m^2}}]. \tag{13}$$

The locations of the observation point P in air or inside the substrate are given by $m = 0$ and 1, respectively, as in Fig. 3. The relation Eq. (13) shall be used later for numerical evaluation of the $G_{zx}^{0,1}$ Green's function. Next, we analyze the $G_{zx}^{0,1}$ for the double layer case.

2.1.2 G_{zx} Green's Function for a Double Layer PEC-backed Substrate

The Green's function for the double layer case with an horizontal electric dipole can be written in the generic form as

$$G_{zx}^{n} = \frac{j\cos\phi}{2\pi k_0^2 \varepsilon_{r2}} \int\limits_{0}^{+\infty} \overline{\mathscr{F}}_{zx}^{n}(\xi,\rho,z,d_1,d_2)d\xi. \tag{14}$$

We also define the z-directed and substrate propagation constants, generically, via Eq. (5) with the index replacement $m \rightarrow n$ and $n = 0,1,2$ therein for the double layer geometry. Here air ($n = 0$), layer # 1 ($n = 1$) and layer # 2 ($n = 2$), for the geometry shown in Fig. 3. The integrand in Eq. (14) reads, for the various layers, designated by the superscript, n, as

$$\overline{\mathscr{F}}_{zx}^{0} = \xi^2 J_1(\xi\rho)e^{-j\kappa_0 z}\left\{\frac{\sin(\kappa_2 d_2)}{\Lambda_1}e^{+j\kappa_0 d_1}\right\}, \qquad\qquad \text{for } d_1 \leq z \subset \infty,$$

$$\overline{\mathscr{F}}_{zx}^{1} = \xi^2 J_1(\xi\rho)\left\{\frac{\sin(\kappa_2 d_2)}{\Lambda_1}\left[\frac{1}{\varepsilon_{r1}}\cos[\kappa_1(d_1-z)] + \frac{\kappa_0}{\kappa_1}\sin[\kappa_1(d_1-z)]\right]\right\}, \qquad \text{for } 0 \leq z \leq d_1,$$

$$\overline{\mathscr{F}}_{zx}^{2} = \xi^2 J_1(\xi\rho)\left\{\frac{j\cos[\kappa_2(d_2+z)]}{\kappa_2\Lambda_1}\left[\kappa_0\cos(\kappa_1 d_1) + j\frac{\kappa_1}{\varepsilon_{r1}}\sin(\kappa_1 d_1)\right]\right\}, \qquad \text{for } -d_2 \leq z \leq 0. \tag{15}$$

The preceding functional forms of the integrands can be found in Ref. [10, pp. 53-54]. In Eq. (15), the quantity

$$\Lambda_1 = \overline{\mathscr{T}}_{11} + \overline{\mathscr{T}}_{12},$$

is given by

$$\overline{\mathscr{T}}_{11} = \frac{j}{\varepsilon_{r2}}\cos(\kappa_1 d_1)\sin(\kappa_2 d_2) + \frac{j}{\varepsilon_{r1}}\frac{\kappa_1}{\kappa_2}\sin(\kappa_1 d_1)\cos(\kappa_2 d_2),$$

$$\overline{\mathscr{T}}_{12} = -\frac{\varepsilon_{r1}}{\varepsilon_{r2}}\frac{\kappa_0}{\kappa_1}\sin(\kappa_1 d_1)\sin(\kappa_2 d_2) + \frac{\kappa_0}{\kappa_2}\cos(\kappa_1 d_1)\cos(\kappa_2 d_2). \tag{16}$$

We examine the branch point contributions from $\kappa_{0,1,2}$ to the Sommerfeld integral Eq. (14). To that end, one can write

$$\frac{\sin(\kappa_2 d_2)}{\Lambda_1} = \frac{1}{\overline{\mathscr{X}}_{11} + \overline{\mathscr{X}}_{12}},$$

where

$$\overline{\mathscr{X}}_{11} = \frac{j}{\varepsilon_{r2}}\left\{\cos(\kappa_1 d_1) + \kappa_1 \sin(\kappa_1 d_1)\frac{\cot(\kappa_2 d_2)}{\kappa_2}\right\},$$

$$\overline{\mathscr{X}}_{12} = \kappa_0\left\{-\frac{\varepsilon_{r1}}{\varepsilon_{r2}}\frac{\sin(\kappa_1 d_1)}{\kappa_1} + \cos(\kappa_1 d_1)\frac{\cot(\kappa_2 d_2)}{\kappa_2}\right\}. \tag{17}$$

By inspecting the functional form of $\overline{\mathscr{X}}_{11,12}$ in Eq. (17) one can conclude, with the help of Eq. (5), that the term

$$\frac{\sin(\kappa_2 d_2)}{\Lambda_1}$$

is an *even* function of the spectral parameter ξ. This can be inferred by examining the Taylor series representations for $\cos(\kappa_1 d_1)$ and $\kappa_1 \sin(\kappa_1 d_1)$, and the Mittag-Leffler form [45, p. 168] for $\cot(\kappa_2 d_2)/\kappa_2$. It will turn out that these representations are in even powers of $\kappa_{1,2}$ and hence not multivalued near branch points defined by $\kappa_{1,2} = 0$. Thus, this term which is also present as a factor in Eq. (15) has no branch point contributions from $\kappa_{1,2}$ propagation constants. Further inspection of the functional behavior of each of the integrands $\overline{\mathscr{F}}_{zx}^{0,1}$, as defined in Eq. (15), show that the branch points at $\kappa_{1,2} = 0$ *do not* contribute to any form of analytic singularity. For the $\overline{\mathscr{F}}_{zx}^{2}$ term in Eq. (15), it remains necessary to examine the nature (*i.e.*, even or odd) of the term $\kappa_2\Lambda_1$. It can be established, multiplying the various terms in Eq. (17) by κ_2 that it is indeed an even function of the term κ_2. Thus to all the integrands in Eq. (15) the branch points defined by $\kappa_{1,2} = 0$ *do not* contribute. The only branch point that contributes to all $\overline{\mathscr{F}}_{zx}^{0,1,2}$ in Eq. (15) is defined by $\kappa_0 = 0$. Hence, the G_{zx} defined by Eq. (14) has the sole branch point contribution from κ_0. Since the branch point contribution results in a continuous spectrum [35, chap. 5] in the radiation zone, this implies that the other layers act to trap waves at propagation constants $\kappa_{1,2}$.

Referring to the last equation in Eq. (15), the term

$$\frac{j\cos(\kappa_2[d_2 + z])}{\kappa_2\Lambda_1}$$

can be shown not to have any branch point contributions from $\kappa_{1,2} = 0$. This can be verified by noting that the denominator $\kappa_2\Lambda_1 = (\overline{\mathscr{X}}_{11} + \overline{\mathscr{X}}_{12})\kappa_2 \sin(\kappa_2 d_2)$ is an *even* function of the z-directed spectral wavenumbers $\kappa_{1,2}$, because, from Eq. (17) it follows that $\overline{\mathscr{X}}_{11,12}$ is an even function of $\kappa_{1,2}$. Thus the ratio of two even functions is an even function, which results in the deduction that branch points, defined by $\kappa_{1,2} = 0$ *do not* contribute to the integrands defined in Eq. (15). The only branch point contribution comes from the location $\kappa_0 = 0$. The asymptotic behavior of the integrands in Eq. (15) is described next.

It turns out that the quantities

$$\frac{\sin(\kappa_2 d_2)}{\Lambda_1} \text{ and } \frac{j\cos(\kappa_2[d_2+z])}{\kappa_2\Lambda_1}$$

need to be examined first for their asymptotic ($\xi \to \infty$) behavior since these appear in the various integrands defined in Eq. (15). Following the usual technique for the single layer case, one notes from Eq. (5) that $\kappa_{1,2} \to -j\xi$ as $\xi \to \infty$. Using the circular to hyperbolic cosine and sine transformations, one obtains the following sequence of relationships, valid for $\xi \to \infty$,

$$\overline{\mathscr{T}}_{11}^{\infty} = \mathscr{T}_{11}(\xi \to \infty) \approx \frac{e^{\xi(d_1+d_2)}}{4}\left[\frac{1}{\varepsilon_{r1}} + \frac{1}{\varepsilon_{r2}}\right],$$

$$\overline{\mathscr{T}}_{12}^{\infty} = \mathscr{T}_{12}(\xi \to \infty) \approx \frac{e^{\xi(d_1+d_2)}}{4}\left[1 + \frac{\varepsilon_{r1}}{\varepsilon_{r2}}\right],$$

$$\Lambda_1^{\infty} = \overline{\mathscr{T}}_{11}^{\infty} + \overline{\mathscr{T}}_{12}^{\infty} \approx \frac{e^{\xi(d_1+d_2)}}{4}\left[1 + \left\{\frac{1}{\varepsilon_{r1}} + \frac{1}{\varepsilon_{r2}}\right\} + \frac{\varepsilon_{r1}}{\varepsilon_{r2}}\right],$$

$$\left.\frac{\sin(\kappa_2 d_2)}{\Lambda_1}\right|_{\xi\to\infty} \approx \frac{-j}{2}\frac{e^{\xi d_2}}{\Lambda_1^{\infty}}; \text{ for } 0 \le z \subset \infty \text{ in Fig. 3,}$$

$$\left.\frac{j\cos[\kappa_2(d_2+z)]}{\kappa_2\Lambda_1}\right|_{\xi\to\infty} \approx -\frac{e^{\xi(d_2+z)}}{2\xi\Lambda_1^{\infty}}; \text{ for } -d_2 \le z \le 0 \text{ in Fig. 3.} \qquad (18)$$

We now investigate the asymptotic behavior of the various terms within $\{\cdots\}$ in Eq. (15) using Eq. (18). To that end, it is a simple matter to obtain the following forms

$$\left.\left\{\frac{\sin(\kappa_2 d_2)}{\Lambda_1}\right\}\right|_{\xi\to\infty} \approx \overline{\mathscr{K}}_0^{\infty}, \qquad\qquad \text{for } d_1 \le z \subset \infty;$$

$$\left.\frac{\sin(\kappa_2 d_2)}{\Lambda_1}\left\{\frac{1}{\varepsilon_{r1}}\cos[\kappa_1(d_1-z)] + j\frac{\kappa_0}{\kappa_1}\sin[\kappa_1(d_1-z)]\right\}\right|_{\xi\to\infty} \approx \overline{\mathscr{K}}_1^{\infty}e^{-z\sqrt{\xi^2-k_1^2}}, \quad \text{for } 0 \le z \le d_1;$$

$$\left.\left[\frac{j\cos(\kappa_2[d_2+z])}{\kappa_2\Lambda_1}\left\{\kappa_0\cos(\kappa_1 d_1) + j\frac{\kappa_1}{\varepsilon_{r1}}\sin(\kappa_1 d_1)\right\}\right]\right|_{\xi\to\infty} \approx \overline{\mathscr{K}}_2^{\infty}e^{-z\sqrt{\xi^2-k_2^2}}, \quad \text{for } -d_2 \le z \le 0. \quad (19)$$

In the above, the "asymptotic" slab constants are

$$\overline{\mathscr{K}}_0^{\infty} = \frac{-2j}{\overline{C}_0},$$

$$\overline{\mathscr{K}}_1^{\infty} = \frac{-j(1+\frac{1}{\varepsilon_{r1}})}{\overline{C}_0},$$

$$\overline{\mathscr{K}}_2^{\infty} = -\overline{\mathscr{K}}_1^{\infty},$$

where

$$\overline{C}_0 = \left[1 + \left\{ \frac{1}{\varepsilon_{r1}} + \frac{1}{\varepsilon_{r2}} \right\} + \frac{\varepsilon_{r1}}{\varepsilon_{r2}} \right]. \tag{20}$$

It is interesting to note that the slab constants are independent of the individual physical thicknesses as $\xi \to \infty$. In view of the relations Eqs. (17–20) one finds that the asymptotic form of the integrands in Eq. (15) are *identical* to that in Eq. (13), with the subscript/superscript index m in Eq. (13) replaced by n, where $n = 0, 1, 2$ for the double layer case.

2.2 Location of Poles for the Integrand of the G_{zx} Green's function

In this section, the poles of the Sommerfeld integrand for single layer substrates are investigated. One of the fundamental aspects of real-axis integration of Sommerfeld integration is the location of the proper surface wave poles. A review of the recent investigations reported in Refs. [74-79] suggests the problem remains unresolved, particularly for electrically thick substrates. The results for single layer are included in this section. Similar analysis for double layer substrates, though straightforward is complicated and it appears that application of some of the existing methods [79] could lead to intractability. Thus, the results for double layer are deferred for future work.

2.2.1 Proper Surface Wave Poles for Single Layer Substrates

For a single layer substrate the proper surface wave poles are given by an equivalent form of Eq. (6) that reads

$$D_{TM}(\xi) = -\varepsilon_{r1} \sqrt{\xi^2 - k_0^2} \cos[d\sqrt{k_1^2 - \xi^2}] + \sqrt{k_1^2 - \xi^2} \sin[d\sqrt{k_1^2 - \xi^2}] \equiv 0. \tag{21}$$

Since exact analytic solutions to the above are not available [6, 11, 12, 74-79], one needs to determine an 'initial guess' for the roots and then use Newton-Raphson algorithm (or other root finding techniques) to obtain better estimates for solutions to Eq. (21). This is a standard procedure [12]. However, it is important to note that the convergence to the desired solution depends on the initial guess for Eq. (21).

The literature contains extensive information for solutions to Eq. (21) but for microstrip antennas, which implies $d/\lambda \leq 0.1$. For layered media, the preceding condition may not be valid. Thus the behavior of the integrands, $\overline{\mathscr{F}}_{zx}^{0,1}(\xi)$, given via Eqs. (7) and (8) in the range $0 \leq \xi \subset \infty$ is important. A practical approach is to depict this information graphically. To that end, some representative behavior of the integrand in Eqs. (3) and (4) is presented in Figs. 5 through 9 (additional results for $\rho = 1000\lambda$ are included in Appendix B). In all these figures, depicting the behavior of the integrand in the Sommerfeld integral, the independent spectral variable, ξ has the units of m^{-1}. Other information are included in the figure captions themselves and hence are omitted here for brevity.

The existence of the proper surface wave poles is seen by the spikes in the integrand. These poles occur in the range $k_0 \leq \xi \leq \Re e(k_1)$. The results in Figs. 5 to 9 (and Figs. B1 to B5 in Appendix B) were generated for a frequency of 5 GHz. Thus the wavelength $\lambda = 2.997925 \times 10^8 / 5.0 \times 10^9 = 0.0599585$ meters; this results in the intrinsic free-space wavenumber $k_0 = 2\pi/\lambda = 104.79 m^{-1}$ and $\Re e(k_1) \equiv \Re e[k_0 \sqrt{|\varepsilon_{r1}|}] = 328.051 m^{-1}$. Therefore, all surface wave poles lie between $104.79 \leq \xi \leq 328.051$ for the single layer case as shown in the figures. This is evidenced by the spikes in either real or imaginary parts of the integrand.
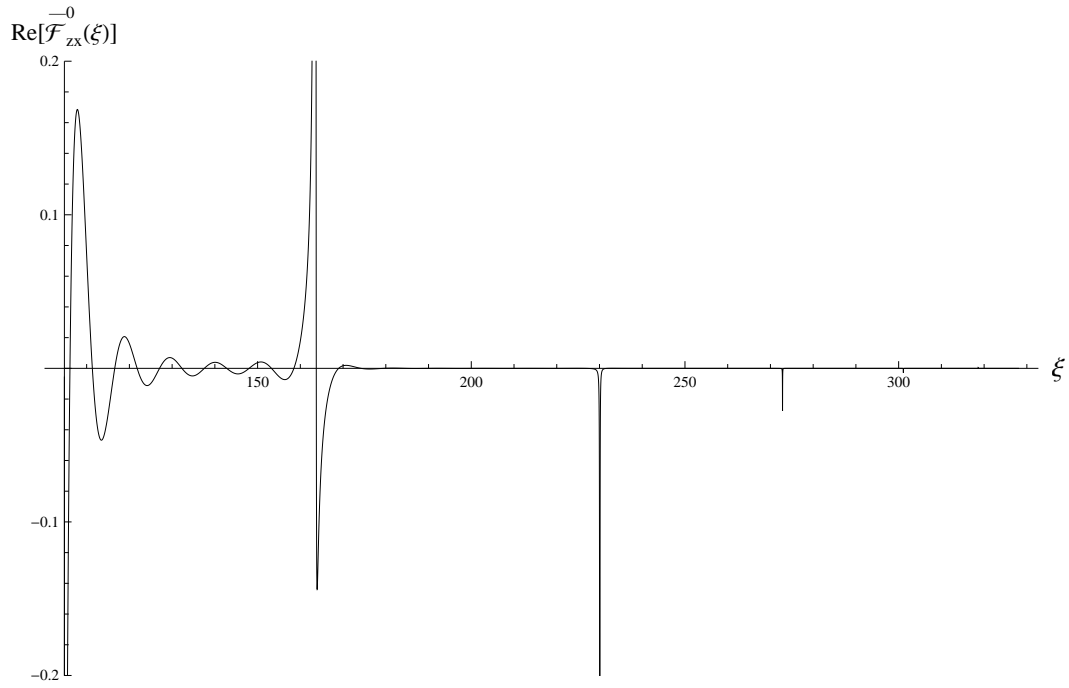
Re[$\overline{\mathcal{F}}^{\,0}_{zx}(\xi)$]

Fig. 5 — Behavior of integrand in Eq. (3) for observation point in air (region # 0) in Fig. 3 for
$\rho = 10\lambda$, $z = +\lambda/2$, $\tan\delta = 0.0001$, $d = \lambda$, and $|\varepsilon_{r1}| = 9.8$
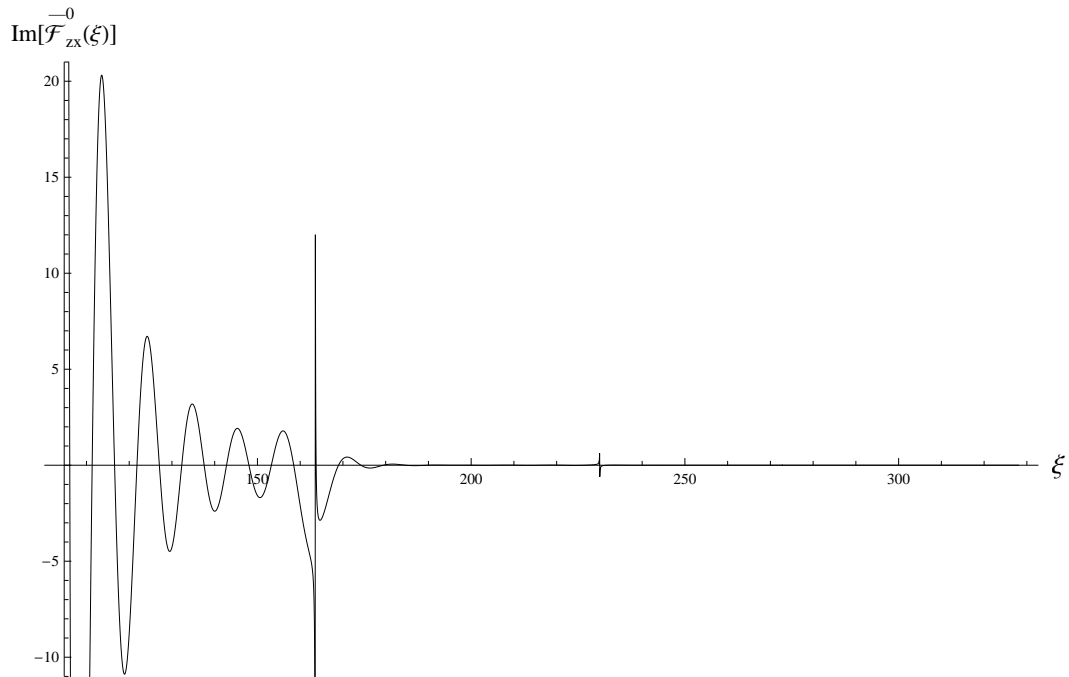
Im[$\overline{\mathcal{F}}^{\,0}_{zx}(\xi)$]

Fig. 6 — Behavior of integrand in Eq. (3) for observation point in air (region # 0) in Fig. 3 for
$\rho = 10\lambda$, $z = +\lambda/2$, $\tan\delta = 0.0001$, $d = \lambda$, and $|\varepsilon_{r1}| = 9.8$
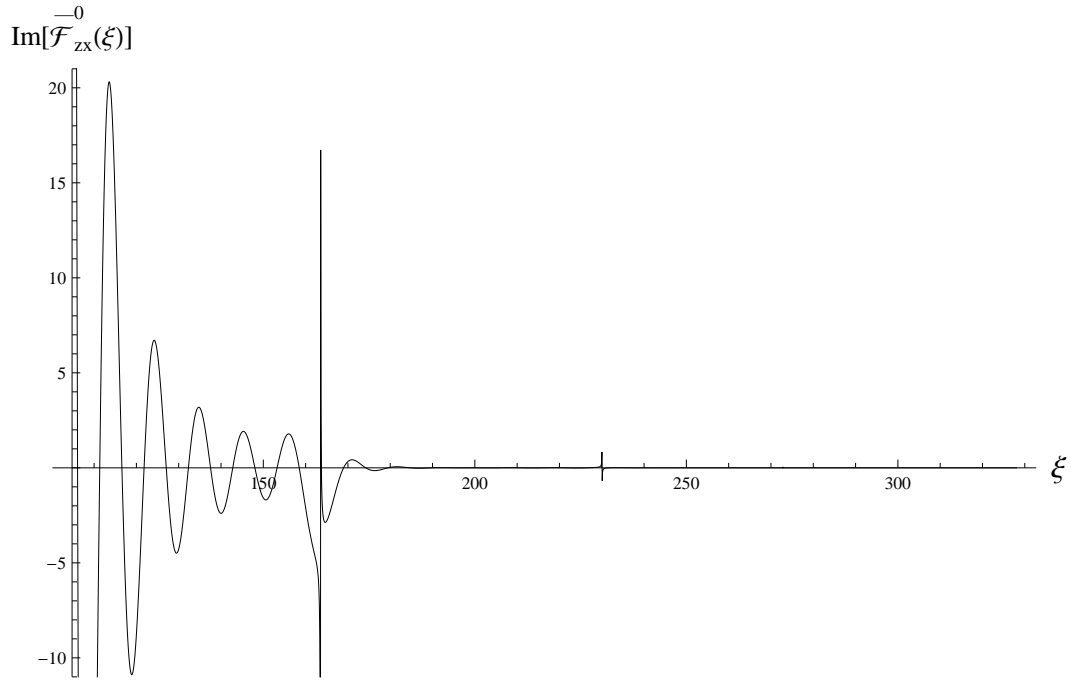
Fig. 7 — Behavior of integrand in Eq. (3) for observation point in air (region # 0) in Fig. 3. All data same as in Fig. 6, except for the lossless case $\tan \delta = 0$.
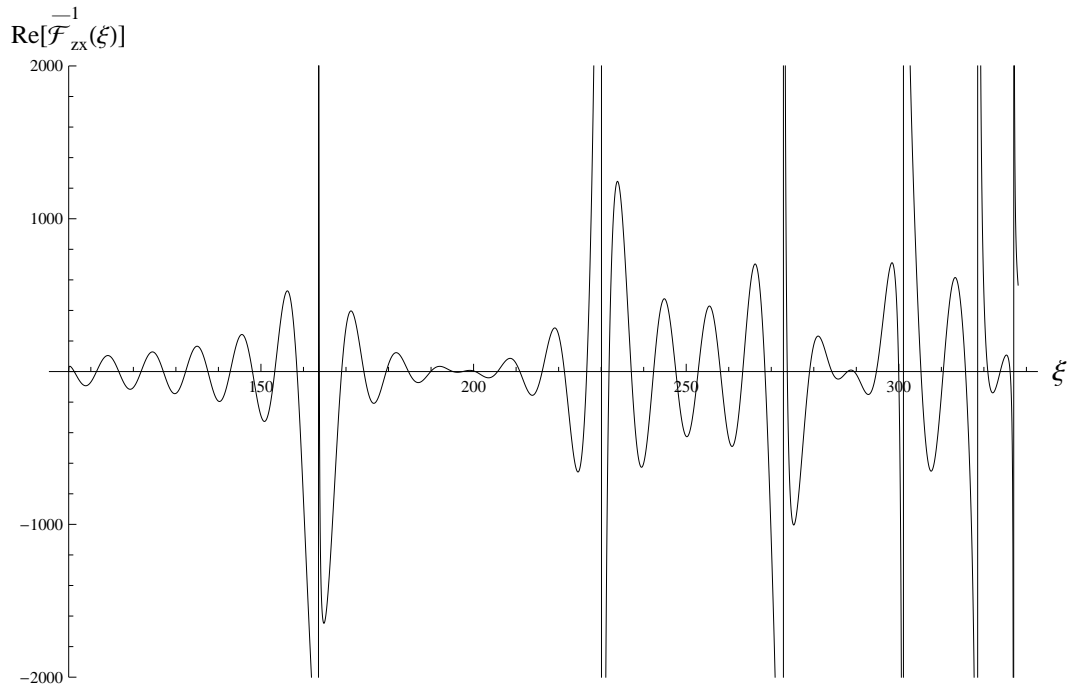

Fig. 8 — Behavior of integrand in Eq. (4) for observation point in substrate (region # 1) in Fig. 3 for $\rho = 10\lambda$, $z = -\lambda/2$, $\tan \delta = 0.0001$, $d = \lambda$, and $|\varepsilon_{r1}| = 9.8$
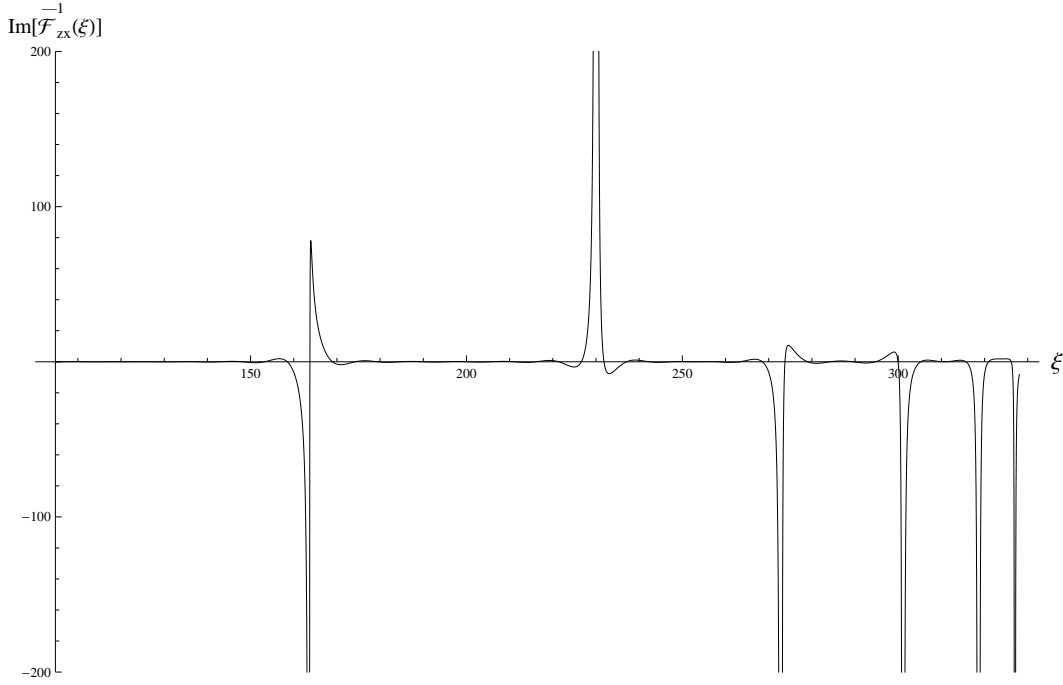
Fig. 9 — Behavior of integrand in Eq. (4) for observation point in substrate (region # 1) in Fig. 3 for
$\rho = 10\lambda$, $z = -\lambda/2$, $\tan\delta = 0.0001$, $d = \lambda$, and $|\varepsilon_{r1}| = 9.8$.

The number of spikes is indicative of the number of first order proper surface wave poles. This suggests that the effects of the poles need to be eliminated to perform any numerical integration (this is shown later in this chapter).

The solution to Eq. (21) can be found by obtaining a "polynomial" form from the original transcendental form, following closely the approach in Ref. [52]. To that end, substitute $u = d\sqrt{k_1^2 - \xi^2}$ and $v = d\sqrt{\xi^2 - k_0^2}$ with $r^2 = u^2 + v^2 = d^2(k_1^2 - k_0^2)$ in Eq. (21), to obtain

$$\varepsilon_{r1} v \cos(u) - u \sin(u) = 0. \tag{22}$$

Next we utilize the convergent (Taylor) power series forms for the sine and cosine in Eq. (22) with the following set of relationships

$$\cos(u) = \sum_{n=0}^{\infty} c_n (r^2 - v^2)^n,$$

$$u \sin(u) = \sum_{n=0}^{\infty} s_n (r^2 - v^2)^{n+1},$$

$$c_n = \frac{(-1)^n}{(2n)!},$$

$$s_n = \frac{(-1)^n}{(2n+1)!}. \tag{23}$$

Using these results in Eq. (22) we get

$$\varepsilon_{r1} v \sum_{n=0}^{+\infty} c_n (r^2 - v^2)^n - \sum_{n=0}^{+\infty} s_n (r^2 - v^2)^{n+1} = 0.$$ (24)

Now the barriers at $\xi = k_0$ and $\xi = \Re e(k_1)$ form the strip within which the proper surface wave poles lie. This equivalently implies that the barriers are defined 'asymptotically' at $v \to 0$ and $u \to 0$. Consequently, in Eq. (24), we shall have roots/solutions when $(r^2 - v^2) \to 0$ and $v \to 0$. This observation allows application of the binomial theorem, *viz.*,

$$v(r^2 - v^2)^n = \sum_{p=0}^{+\infty} \binom{n}{p} (-1)^p r^{2(n-p)} v^{2p+1},$$

$$(r^2 - v^2)^{n+1} = \sum_{p=0}^{+\infty} \binom{n+1}{p} (-1)^p r^{2(n+1-p)} v^{2p}.$$ (25)

Using Eq. (25) in Eq. (24) and truncating both the infinite series at the Nth term, we have the "polynomial" form of the equation that reads

$$\varepsilon_{r1} \sum_{p=0}^{N} v^{2p+1} (-1)^p \sum_{n=p}^{N} c_n \binom{n}{p} r^{2(n-p)} - \sum_{p=0}^{N+1} v^{2p} (-1)^p \sum_{n=p}^{N} s_n \binom{n+1}{p} r^{2(n+1-p)} = 0.$$ (26)

Eq. (26) is solved to find the approximate location of the roots for v, and hence ξ_p the location of the pth pole in the complex ξ plane. Once ξ_p is found, then from the conditions, *viz.*, $k_0 \le \xi_p \le \Re e(k_1)$ and $\Im m(\kappa_0 \equiv \sqrt{k_0^2 - \xi_p^2}) \le 0$, the appropriate poles can be chosen. Satisfying these conditions implies the choice of poles shall yield only the *proper surface wave* poles, which is required for real-axis integration of Sommerfeld integrals.

Once the determination has been made via the above criterion, the Newton-Raphson method can be applied to further refine these pole locations. Figure 10 shows that the order of the polynomial in Eq. (26) increases with both ε_{r1} and electrical thickness d/λ. The result in Fig. 10 indicates the difficulty of determining relevant pole locations for electrically thick substrates. Surveying the relevant literature [74-79], this issue remains an open-problem. The difficulty is that while numerically rigorous methods [75, 79] exist, their implementation increases the computational burden. From a practical perspective, this still remains an open problem.

The total (integer) number of proper surface wave poles, N_p, lying in the range $k_0 \le \xi_p \le \Re e(k_1)$ is determined *approximately* from the relationship

$$N_p = \texttt{Int} \left[\frac{k_0 d \sqrt{|\varepsilon_{r1}| - 1}}{\pi} \right] + 1.$$ (27)

Thus, for $\varepsilon_{r1} = 9.8$, $d = \lambda$, we get $N_p = \texttt{Int}[5.932958] + 1 = 5 + 1 = 6$ (see Fig. 10). The information gleaned from the results in Figs. 10 to 12 may be summarized to indicate that surface wave pole locations
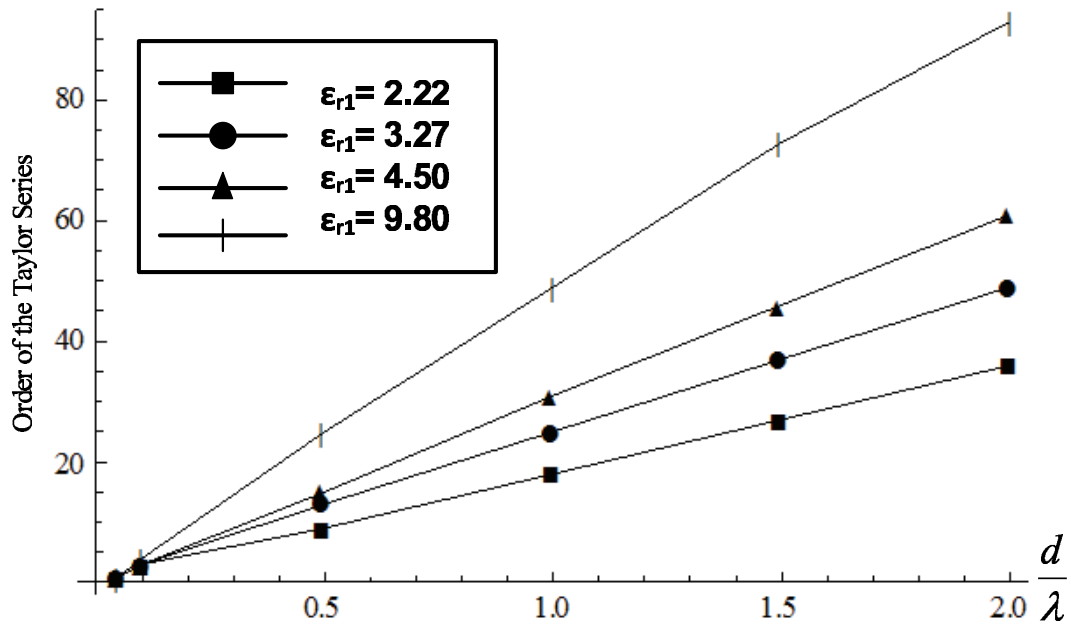
Fig. 10 — Order N of the Taylor polynomial equation in Eq. (26) vs. electrical thickness of the substrate d/λ for various substrate permittivities.
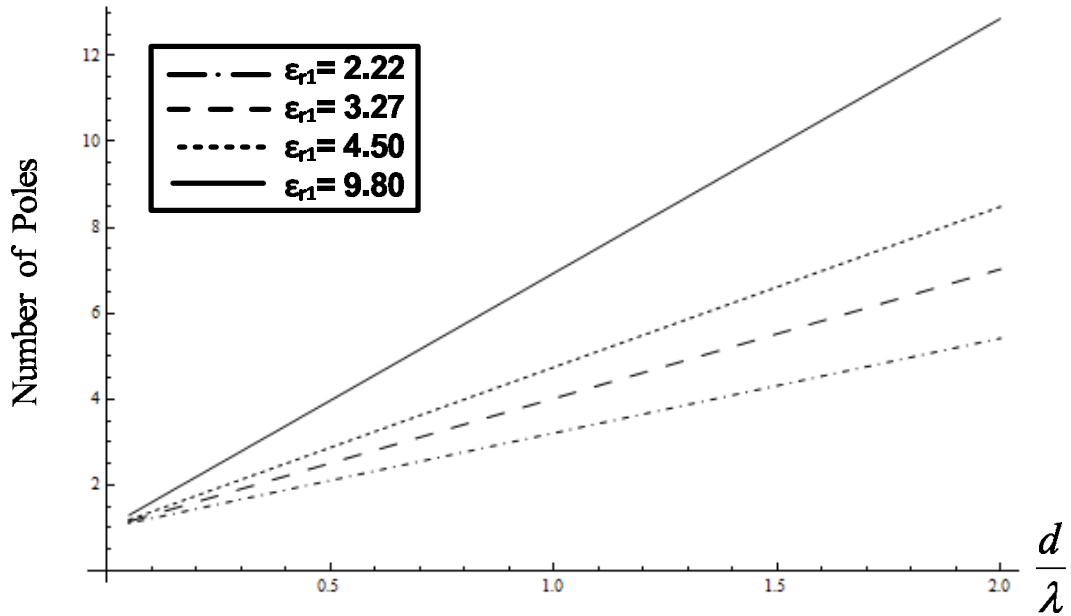

Fig. 11 — Number of proper surface wave poles vs. electrical thickness of the substrate d/λ for various substrate permittivities.
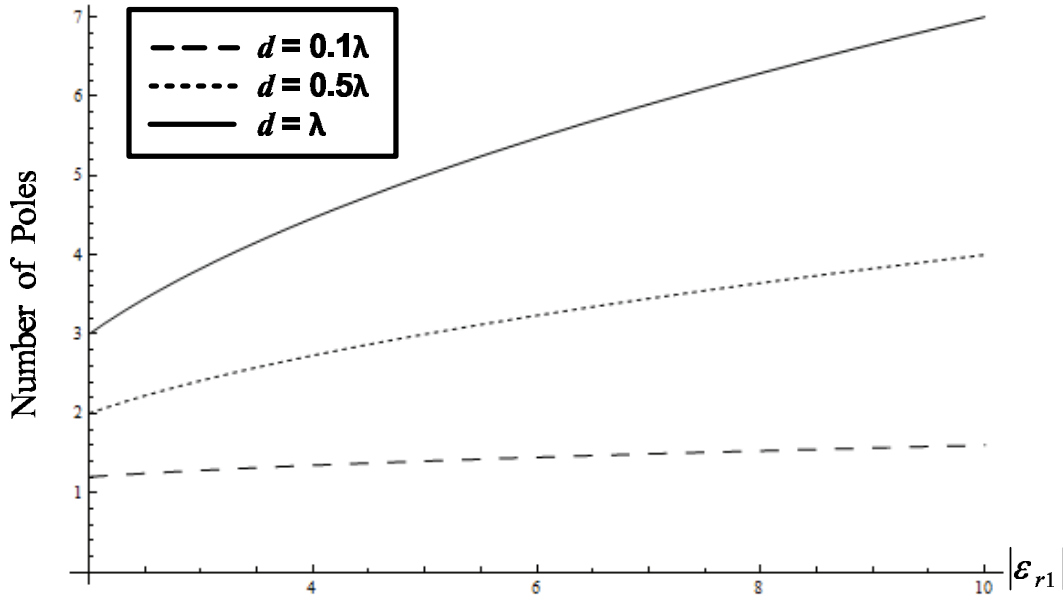
Fig. 12 — Number of proper surface wave poles vs. substrate permittivities $|\varepsilon_{r1}|$ for various electrical thickness of the substrate d/λ.

for arbitrarily electrically thick media is a difficult computational problem. A practical guideline needs to be determined for such situations.

The dispersion characteristics of the proper surface wave poles with permittivity loss is shown in Figs. 13 to 16. The total number of poles in each of these figures remains the same, following Eq. (27). However, as the substrate becomes optically dense, *viz.*, $\varepsilon_{r1} = 2.22 \rightarrow 9.8$, with $d/\lambda = 0.25$, the poles can be seen to migrate away from the $\Re e(\xi/k_0)$ axis in Figs. 13 to 14.

Similar remarks apply to the nature of results Figs. 15 and 16. Thus, increase of loss in the material causes surface wave poles to move away from the $\Re e(\xi/k_0)$ axis for optically dense or electrically thick materials. The movement of poles away from the $\Re e(\xi)$ axis for the lossy case suggests that real-axis numerical integration is much stable for the lossy case than the lossless case.

2.3 Real Axis Integration of Sommerfeld Integrals for the G_{zx} Green's function

In this section, the algorithm for calculating the Sommerfeld integrals in the G_{zx} function in both single and double layer situations is presented comprehensively. This is suggested by observing a lot of commonality in their respective functional behavior over the range of integration $0 \leq \xi \subset \infty$. There are three regions as identified in the begining of this chapter. To that end, the two categories of singular behavior of the Sommerfeld integrand are: (a) simple pole singularities and (b) oscillatory behavior over the tail part of the integrand.

We just rewrite Eq. (13), with a slight change in notation as follows

$$\overline{\mathscr{F}}_{zx}^{n\infty}(\xi \geq \xi_A^n) = \overline{\mathscr{K}}_n^{\infty}[\xi^2 J_1(\xi\rho)\exp(-z\sqrt{\xi^2 - k_n^2})]. \tag{28}$$

Im $[\xi/k_0]$

Re$[\xi/k_0]$

Fig. 13 — TM surface pole dispersion diagram vs. substrate loss tangents for a single layer PEC-backed substrate with thickness $d/\lambda = 0.25$ and $|\varepsilon| = 2.22$; $\tan\delta = 0.000(\triangle)$, $\tan\delta = 0.0001(\star)$, $\tan\delta = 0.001(\bigcirc)$, and $\tan\delta = 0.01(\square)$.

Im $[\xi/k_0]$

Re$[\xi/k_0]$

Fig. 14 — TM surface pole dispersion diagram vs. substrate loss tangents for a single layer PEC-backed substrate with thickness $d/\lambda = 0.25$ and $|\varepsilon| = 9.8$; $\tan\delta = 0.000(\triangle)$, $\tan\delta = 0.0001(\star)$, $\tan\delta = 0.001(\bigcirc)$, and $\tan\delta = 0.01(\square)$.

Fig. 15 — TM surface pole dispersion diagram vs. substrate loss tangents for a single layer PEC-backed substrate with thickness $d/\lambda = 1.0$ and $|\varepsilon| = 2.22$; $\tan\delta = 0.000(\triangle)$, $\tan\delta = 0.0001(\star)$, $\tan\delta = 0.001(\bigcirc)$, and $\tan\delta = 0.01(\square)$.
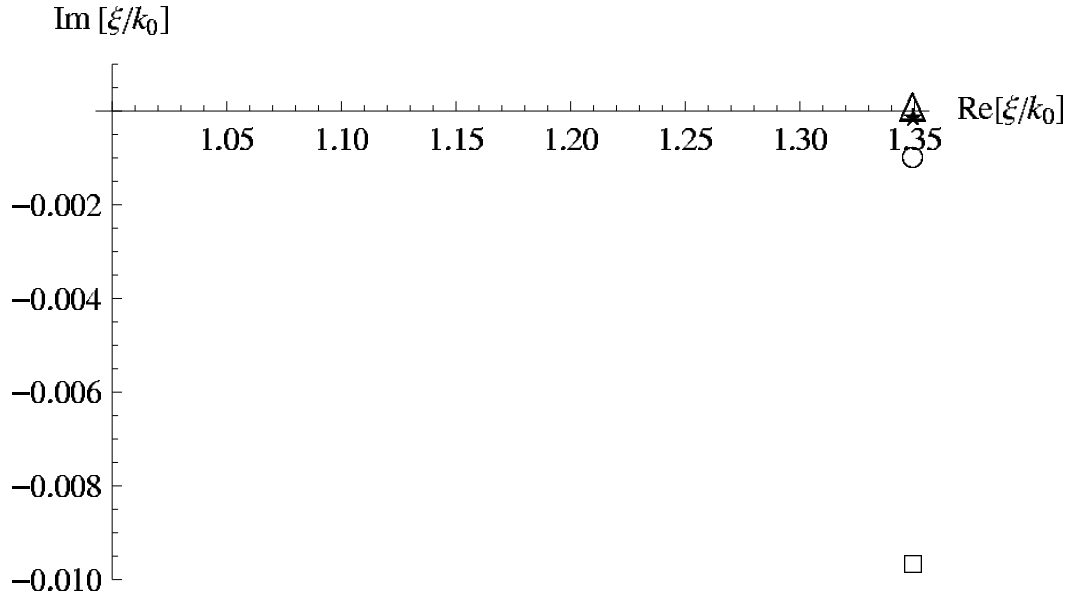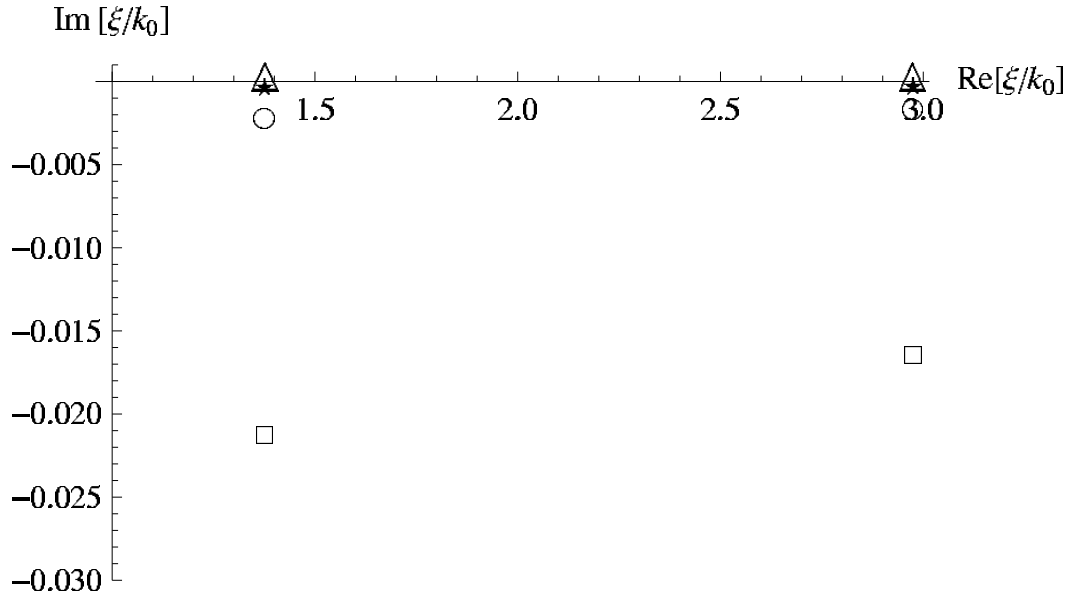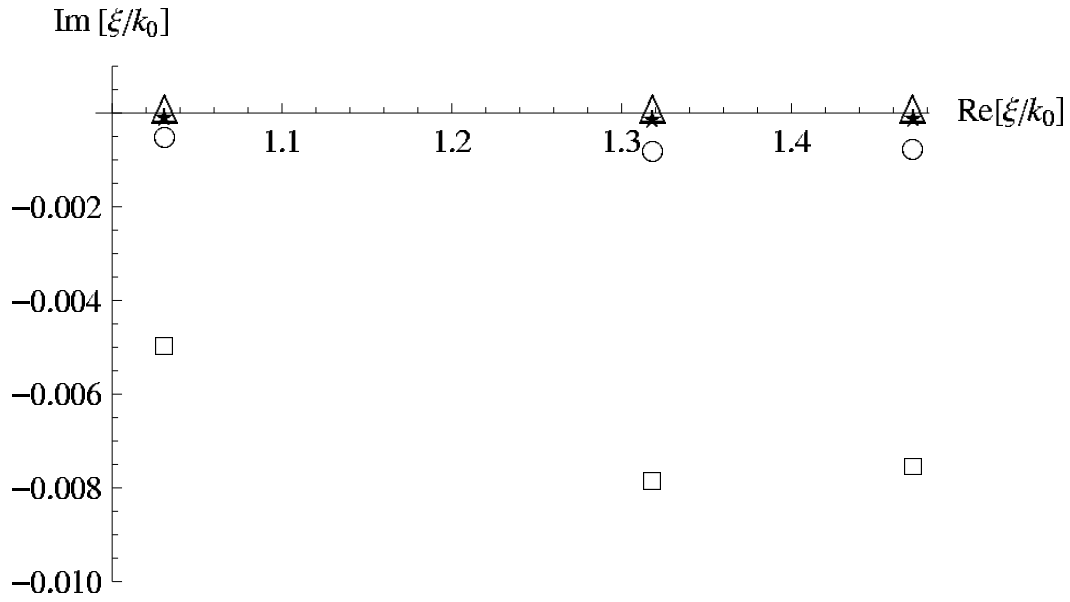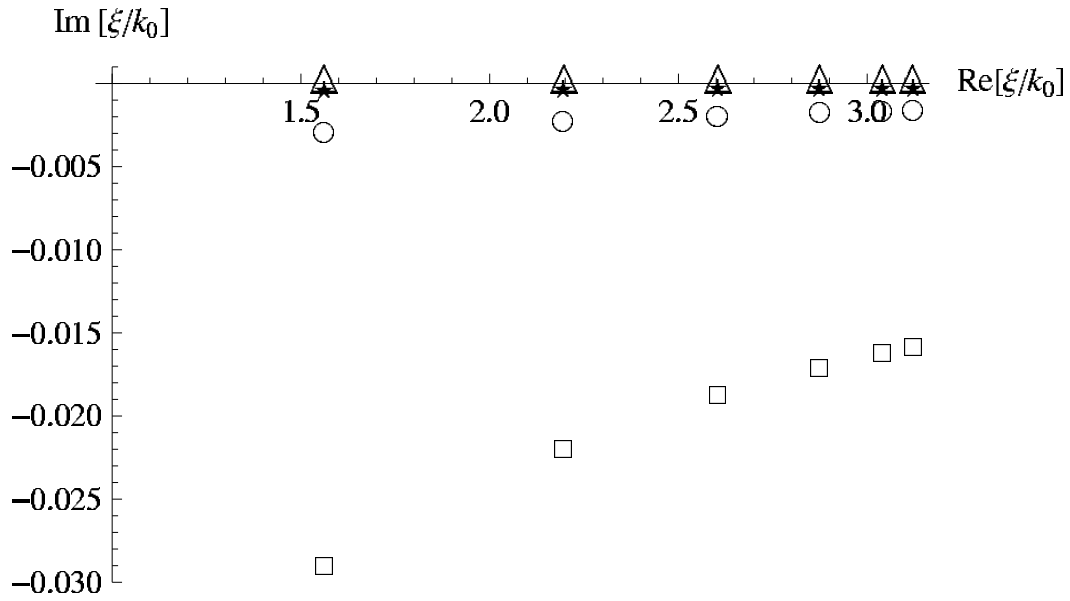

Fig. 16 — TM surface pole dispersion diagram vs. substrate loss tangents for a single layer PEC-backed substrate with thickness $d/\lambda = 1.0$ and $|\varepsilon| = 9.8$; $\tan\delta = 0.000(\triangle)$, $\tan\delta = 0.0001(\star)$, $\tan\delta = 0.001(\bigcirc)$, and $\tan\delta = 0.01(\square)$.

In Eq. (28), $n = 0, 1$ for a single and $n = 0, 1, 2$ double layer substrates, and $\overline{\mathscr{K}}_n^\infty$ are given by Eq. (10) for single and Eq. (20) for double layer cases, respectively. Next, one needs to define the "breakpoint" ξ_A^n for applying the result in Eq. (28) for numerical calculations. While several choices might exist [57], for the purposes of this report it is convenient to first define the range: $k_{min} \leq \xi \leq k_{max}$ This is the region within which *all* poles defined by $D_{TM}(\xi) = 0$ (single layer) and $\Lambda_1(\xi) = 0$ (double layer) cases lie (one needs to refer to Eqs. (6) and (16) for explicit functional forms in determining the poles). To that end, one defines

(a) $k_{min} = \min \subseteq \Re e(k_n)$ and $k_{max} = \max \subseteq \Re e(k_n)$, where, $n = 0, 1$ (single layer) and $= 0, 1, 2$ (double layer), as appropriate,

(b) $\xi_A^n \approx 1.5 k_{max} = \xi_A$ is chosen as the fixed breakpoint for all layers instead of being variable.

Inspecting the exact forms of the integrands in Eqs. (7) and (15), it turns out that one can *generically* write both single and double layer cases as follows

$$\overline{\mathscr{F}}_{zx}^n(\xi) = \frac{\overline{\mathscr{N}}_{zx}^n(\xi)}{\overline{\mathscr{D}}(\xi)}. \tag{29}$$

In Eq. (29), $\overline{\mathscr{D}}(\xi) = D_{TM}(\xi)$ for single and $\overline{\mathscr{D}}(\xi) = \Lambda_1(\xi)$ for double layer cases, respectively. As stated before, one of the main assumptions is that the proper surface wave poles lying in the region defined by $k_{min} \leq \xi \leq k_{max}$, are *simple, first order* poles. The residue at the pth first order pole is given by [45, p. 145]

$$\overline{\mathscr{R}}_p \equiv \lim_{\xi \to \xi_p} \left\{ (\xi - \xi_p) \frac{\overline{\mathscr{N}}_{zx}^n(\xi)}{\overline{\mathscr{D}}(\xi)} \right\} = \frac{\overline{\mathscr{N}}_{zx}^n(\xi_p)}{\left. \frac{dD}{d\xi} \right|_{\xi = \xi_p}}. \tag{30}$$

In Eq. (30)

$$\frac{d\overline{\mathscr{D}}}{d\xi} = -j\xi \left[\cos(d\sqrt{k_1^2 - \xi^2}) \left\{ d + \frac{\varepsilon_{r1}}{\sqrt{k_1^2 - \xi^2}} \right\} + \sin(d\sqrt{k_1^2 - \xi^2}) \left\{ \frac{1 + d\varepsilon_{r1}\sqrt{k_1^2 - \xi^2}}{\sqrt{k_1^2 - \xi^2}} \right\} \right], \tag{31}$$

for the single layer case. The $\overline{\mathscr{N}}_{zx}^n(\xi_p)$ in Eq. (30) can be found via inspection from Eqs. (9) and (15). If we assume further that there are a *finite* number of such poles, then one can subtract the effects of the pole singularities in the appropriate region [6, pp. 161-164; 10; 12, pp. 167-169]. This requires calculation of the residues at the simple poles via Eqs. (30) and (31). This creates a smooth functional behavior over that region, and the behavior of the thus modified integrand is shown here. In addition, beyond the breakpoint, one can subtract the form Eq. (29) to reduce the effects of the large oscillations due to the Bessel function. The oscillatory behavior is very critical when the observation point is near the interfaces, *i.e.*, $z \approx 0$. Considering

all the aspects, we can write the integral

$$
G_{zx}^n = \overline{C}^n \int_0^\infty \overline{\mathscr{F}}_{zx}^n(\xi)\,d\xi,
$$

$$
= \overline{C}^n \left\{ \int_0^{\xi_A} \overline{\mathscr{F}}_{zx}^n(\xi)\,d\xi + \int_{\xi_A}^{+\infty} \overline{\mathscr{F}}_{zx}^n(\xi)\,d\xi \right\},
$$

$$
\approx \overline{C}^n \left\{ \int_0^{\xi_A} [\overline{\mathscr{F}}_{zx}^n(\xi) - \overline{\mathscr{F}}_{zx}^{n\infty}(\xi \geq \xi_A^n)]\,d\xi + \rho z \frac{e^{-jk_n r}}{r^5}[3 + 3jk_n r - (k_n r)^2] \right\}. \tag{32}
$$

The last line in Eq. (32) follows from Eq. (A10) in Appendix A. The $\overline{C}^n$ term is a constant. The finite integral in Eq. (32) expands to

$$
\int_0^{\xi_A} [\overline{\mathscr{F}}_{zx}^n(\xi) - \overline{\mathscr{F}}_{zx}^{n\infty}(\xi \geq \xi_A^n)]\,d\xi = \int_0^{k_{min}} [\overline{\mathscr{F}}_{zx}^n(\xi) - \overline{\mathscr{F}}_{zx}^{n\infty}(\xi \geq \xi_A^n)]\,d\xi
$$

$$
+ \int_{k_{min}}^{k_{max}} \left[\overline{\mathscr{F}}_{zx}^n(\xi) - \overline{\mathscr{F}}_{zx}^{n\infty}(\xi \geq \xi_A^n) - \sum_{p=1}^P \frac{\overline{\mathscr{R}}_p}{\xi - \xi_p} \right] d\xi
$$

$$
+ \sum_{p=1}^P \overline{\mathscr{R}}_p \int_{k_{min}}^{k_{max}} \frac{d\xi}{\xi - \xi_p} + \int_{k_{max}}^{\xi_A} [\overline{\mathscr{F}}_{zx}^n(\xi) - \overline{\mathscr{F}}_{zx}^{n\infty}(\xi \geq \xi_A^n)]\,d\xi. \tag{33}
$$

Following Ref. [6, pp. 161-164] the integral in Eq. (33), *viz.*,

$$
\int_{k_{min}}^{k_{max}} \frac{d\xi}{\xi - \xi_p} = \ln\left[\frac{k_{max} - \xi_p}{\xi_p - k_{min}} \right] - j\pi.
$$

In arriving at the preceding result, use has been made of the definition $\ln(-1) = -j\pi$ [6, p. 163]. Consequently, based on the results from the analysis of the behavior of the integrands, one can easily use simple numerical integration routines because the singular behavior resulting from pole and oscillatory nature of the integrands have been eliminated. In fact, this is the fundamental basis of a wide class of techniques for semi-infinite integration of functions with various types of singularities. Thus, the G_{zx}^n given in Eqs. (3), (4), and (14) as improper spectral (inverse Fourier transform) integrals can be numerically integrated, if the proper pole locations can accurately be calculated.

Some remarks regarding the analytic nature of the integrands needs clarification for this numerical calculations. First, use must be made of Eq. (5) in the analytic form for $\overline{\mathscr{F}}_{zx}^n(\xi)$ in carrying out the integration. This ensures that the analytic continuation is preserved that is consistent with Sommerfeld radiation condition. Second, the functional form of $\overline{\mathscr{F}}_{zx}^{n\infty}(\xi)$ contains an exponent term. This term must also be modified

in appropriate regions by the important analytic continuation result in Eq. (5). If these are not observed carefully, numerical errors shall accrue and incorrect (and sometimes intractable) answers may be obtained.

2.3.1   Numerical Results and Discussion

In this final subsection, the behavior of the *singularity-extracted* and *original* integrand appearing in Eq. (32), *viz.*,

$$\overline{\mathscr{Z}}(\xi) = \overline{\mathscr{F}}^n_{zx}(\xi) - \overline{\mathscr{F}}^{n\infty}_{zx}(\xi \geq \xi^n_A), \text{ when } \xi \leq k_{min},$$

$$= \overline{\mathscr{F}}^n_{zx}(\xi) - \overline{\mathscr{F}}^{n\infty}_{zx}(\xi \geq \xi^n_A) - \sum_{p=1}^{P} \frac{\overline{\mathscr{R}}_p}{\xi - \xi_p}, \text{ when } k_{min} \leq \xi \leq k_{max},$$

$$= \overline{\mathscr{F}}^n_{zx}(\xi) - \overline{\mathscr{F}}^{n\infty}_{zx}(\xi \geq \xi^n_A), \text{ when } \xi \geq k_{max} = \xi_A, \tag{34}$$

is shown in Figs. 17 and 18 (additional results for $\rho = 1000\lambda$ are included in Figs. B6 and B7). The evident importance of the singularity subtraction is seen in these figures and thus one can use straightforward numerical integration methods to evaluate the resulting integral(s) appearing in the G^n_{zx} in Eq. (32). The results of real-axis numerical integration, for $G^{n=0,1}_{zx}$, is shown in Figs. 19 to 26. In these figures, all data is included and hence are omitted here to avoid tedium. The plots are for observation point inside ($n = 1$) to outside ($n = 0$) the substrate and depicted here as a function of z/λ for $\rho/\lambda = 10$ and 100.

To investigate the computational efficiency of the singularity-subtraction algorithm in Eq. (32), the in-built numerical integration routines in *MATHEMATICA* were used. Of course the algorithm in Eq. (32) was
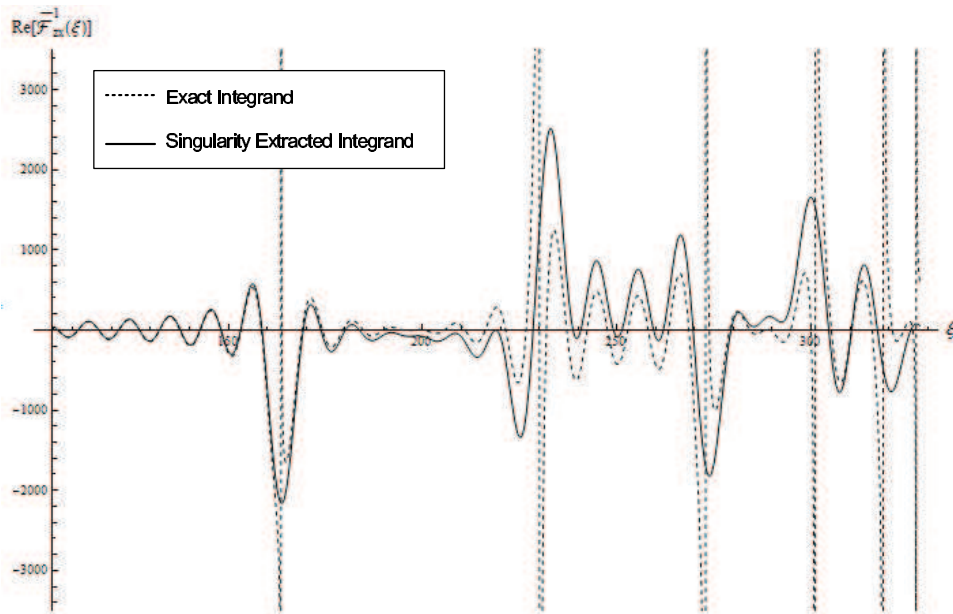
Fig. 17 — Behavior of the integrand in the Sommerfeld integral for the $G_{zx}(\rho, z, \phi)$ Green's function in Eqs. (32) and (33). Here $d = \lambda$, $\rho = 10\lambda$, $\phi = 0°$, $z = -\lambda/2$, $\tan \delta = 0$, and $|\varepsilon_{r1}| = 9.8$. The observation point is inside the substrate. The imaginary part of the integrand identically vanishes.
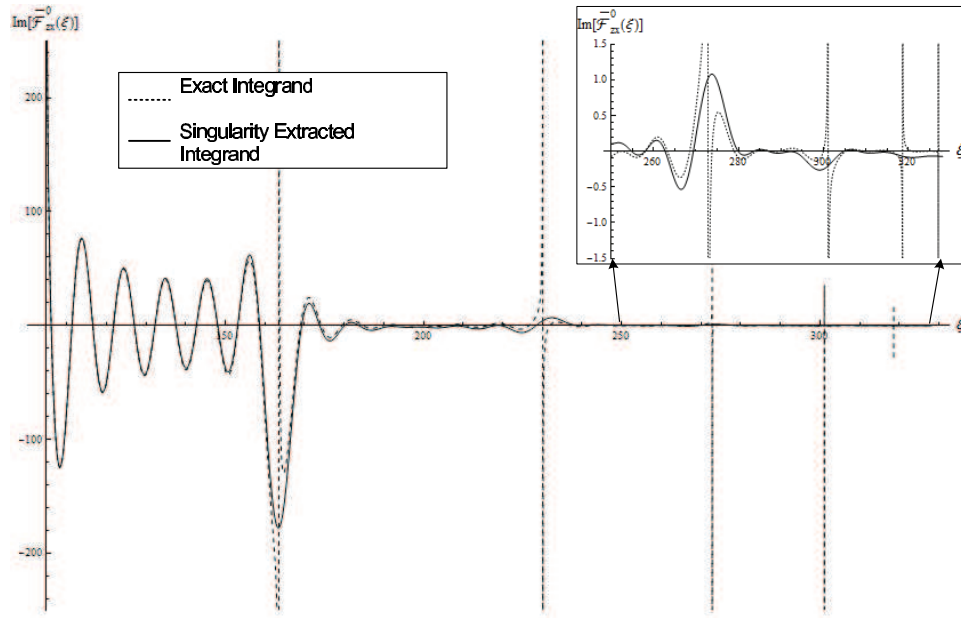
Fig. 18 — Behavior of the integrand in the Sommerfeld integral for the $G_{zx}(\rho, z, \phi)$ Green's function in Eqs. (32) and (33). Here $d = \lambda$, $\rho = 10\lambda$, $\phi = 0°$, $z = +\lambda/2$, $\tan\delta = 0$, and $|\varepsilon_{r1}| = 9.8$. The observation point is outside the substrate. The real part of the integrand identically vanishes.

Fig. 19 — Behavior of the $G_{zx}(\rho, z, \phi)$ Green's function vs. z/λ when observation point is inside the substrate. Here $d = \lambda$, $\rho = 10\lambda$, $\phi = 0°$, $\tan\delta = 0.0001$ and $|\varepsilon_{r1}| = 9.8$. The crosses ($\times$) refer to Eq. (32) and the triangles ($\triangle$) refer to direct *MATHEMATICA* computations. For Eq. (32), the breakpoint $\xi_A = k_{max} = \Re e(k_1)$.

$\mathrm{Re}[G^0_{\mathrm{ZX}}]$

Fig. 20 — Behavior of the $G_{zx}(\rho, z, \phi)$ Green's function vs. z/λ when observation point is outside the substrate. Here $d = \lambda$, $\rho = 10\lambda$, $\phi = 0°$, $\tan\delta = 0.0001$, and $|\varepsilon_{r1}| = 9.8$. The crosses ($\times$) refer to Eq. (32) and the triangles ($\triangle$) refer to direct *MATHEMATICA* computations. For Eq. (32), the breakpoint $\xi_A = \mathrm{k}_{max} = \Re e(\mathrm{k}_1)$.

$\mathrm{Im}[G^1_{\mathrm{ZX}}]$

Fig. 21 — Behavior of the $G_{zx}(\rho, z, \phi)$ Green's function vs. z/λ when observation point is inside the substrate. Here $d = \lambda$, $\rho = 10\lambda$, $\phi = 0°$, $\tan\delta = 0.0001$, and $|\varepsilon_{r1}| = 9.8$. The crosses ($\times$) refer to Eq. (32) and the triangles ($\triangle$) refer to direct *MATHEMATICA* computations. For Eq. (32), the breakpoint $\xi_A = \mathrm{k}_{max} = \Re e(\mathrm{k}_1)$.

Fig. 22 — Behavior of the $G_{zx}(\rho, z, \phi)$ Green's function vs. z/λ when observation point is outside the substrate. Here $d = \lambda$, $\rho = 10\lambda$, $\phi = 0°$, $\tan\delta = 0.0001$, and $|\varepsilon_{r1}| = 9.8$. The crosses ($\times$) refer to Eq. (32) and the triangles ($\triangle$) refer to direct *MATHEMATICA* computations. For Eq. (32), the breakpoint $\xi_A = k_{max} = \Re e(k_1)$.
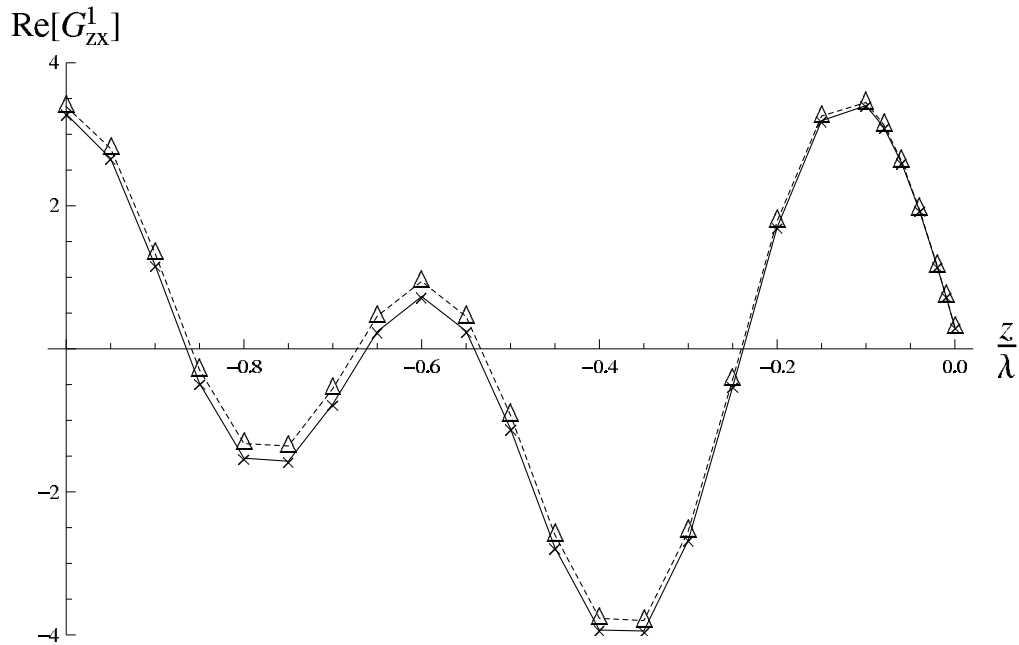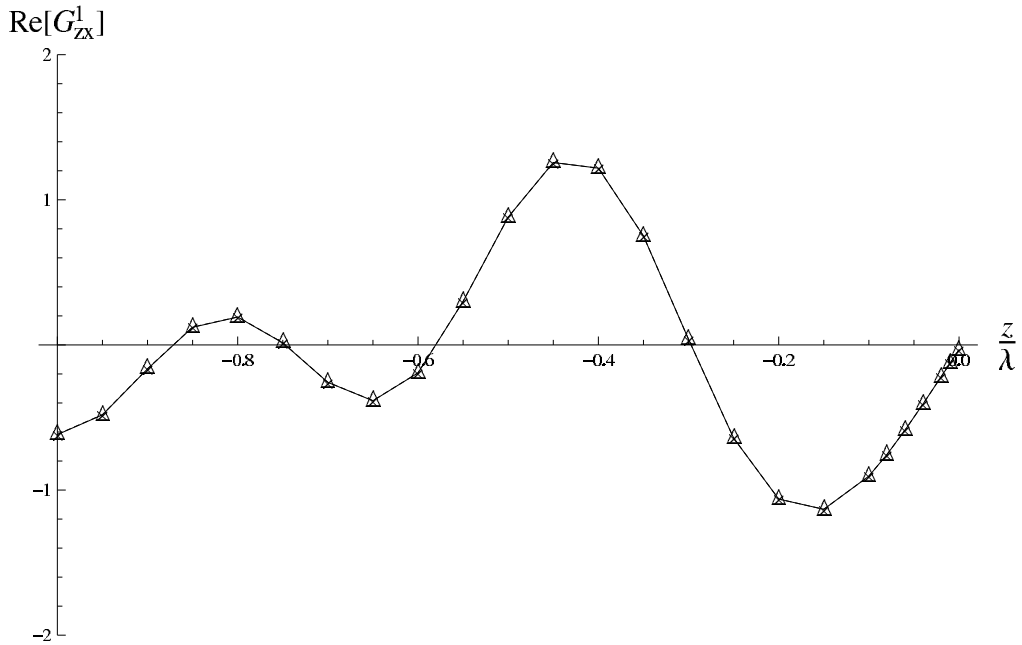

Fig. 23 — Behavior of the $G_{zx}(\rho, z, \phi)$ Green's function vs. z/λ when observation point is inside the substrate. Here $d = \lambda$, $\rho = 100\lambda$, $\phi = 0°$, $\tan\delta = 0.0001$, and $|\varepsilon_{r1}| = 9.8$. The crosses ($\times$) refer to Eq. (32) and the triangles ($\triangle$) refer to direct *MATHEMATICA* computations. For Eq. (32), the breakpoint $\xi_A = k_{max} = \Re e(k_1)$.
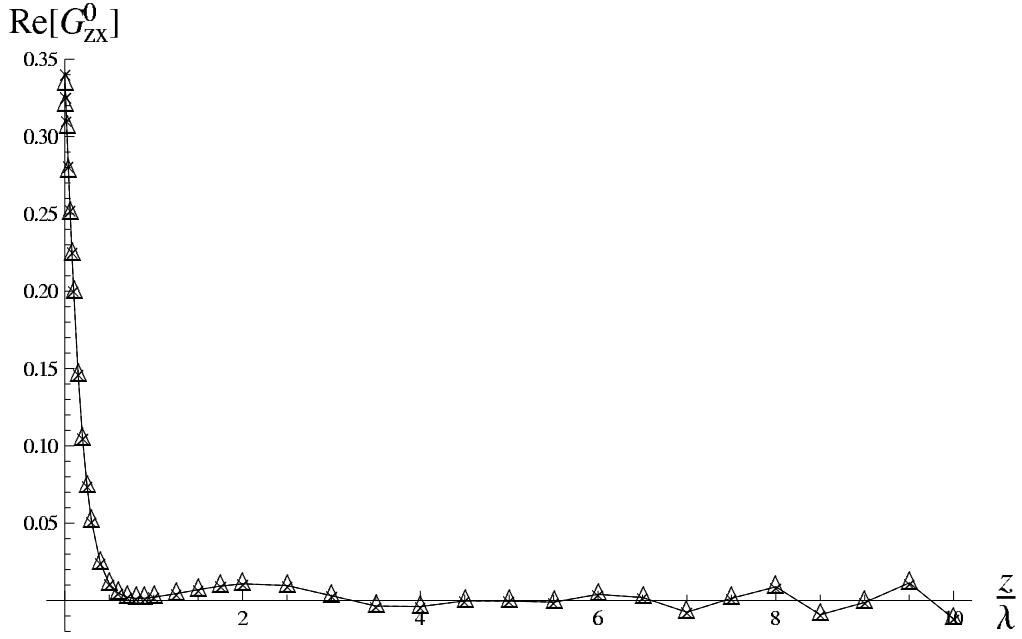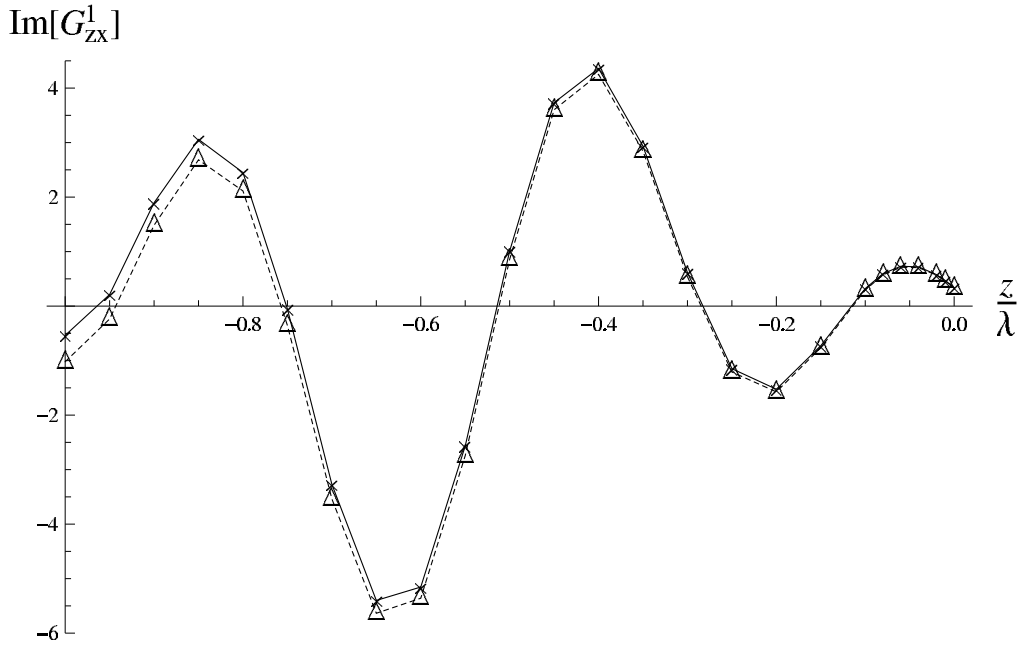
$\mathrm{Re}[G^0_{zx}]$
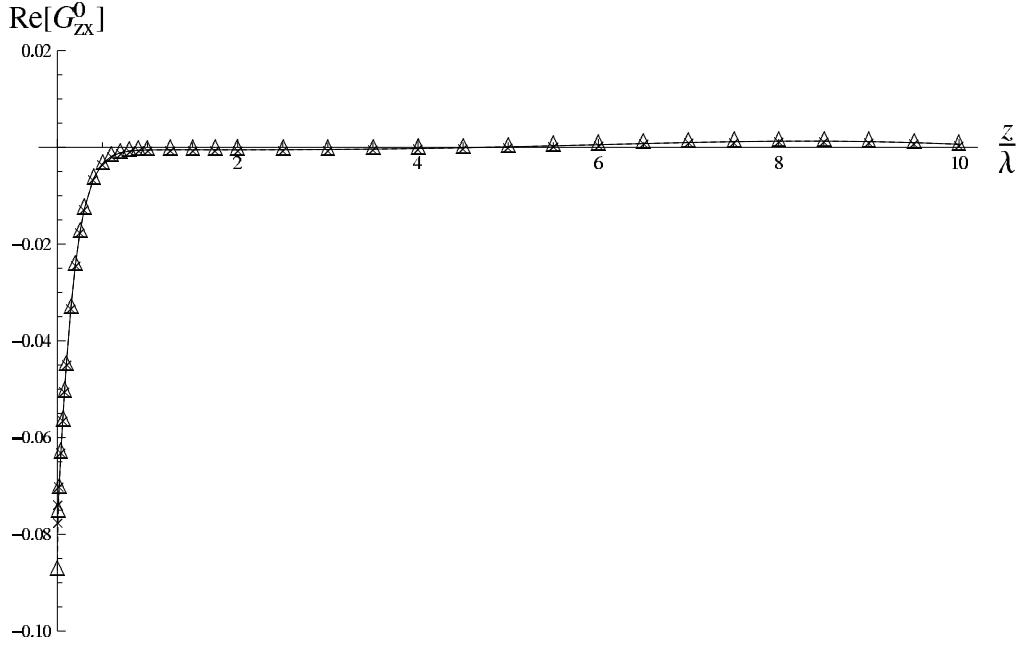
Fig. 24 — Behavior of the $G_{zx}(\rho, z, \phi)$ Green's function vs. z/λ when observation point is outside the substrate. Here $d = \lambda$, $\rho = 100\lambda$, $\phi = 0°$, $\tan\delta = 0.0001$, and $|\varepsilon_{r1}| = 9.8$. The crosses ($\times$) refer to Eq. (32) and the triangles ($\triangle$) refer to direct *MATHEMATICA* computations. For Eq. (32) the breakpoint $\xi_A = \mathrm{k}_{max} = \Re e(\mathrm{k}_1)$.

$\mathrm{Im}[G^1_{zx}]$

Fig. 25 — Behavior of the $G_{zx}(\rho, z, \phi)$ Green's function vs. z/λ when observation point is inside the substrate. Here $d = \lambda$, $\rho = 100\lambda$, $\phi = 0°$, $\tan\delta = 0.0001$, and $|\varepsilon_{r1}| = 9.8$. The crosses ($\times$) refer to Eq. (32) and the triangles ($\triangle$) refer to direct *MATHEMATICA* computations. For Eq. (32), the breakpoint $\xi_A = \mathrm{k}_{max} = \Re e(\mathrm{k}_1)$.

Fig. 26 — Behavior of the $G_{zx}(\rho, z, \phi)$ Green's function vs. z/λ when observation point is outside the substrate. Here $d = \lambda$, $\rho = 100\lambda$, $\phi = 0°$, $\tan\delta = 0.0001$, and $|\varepsilon_{r1}| = 9.8$. The crosses ($\times$) refer to Eq. (32) and the triangles ($\triangle$) refer to direct *MATHEMATICA* computations. For Eq. (32), the breakpoint $\xi_A = k_{max} = \Re e(k_1)$.
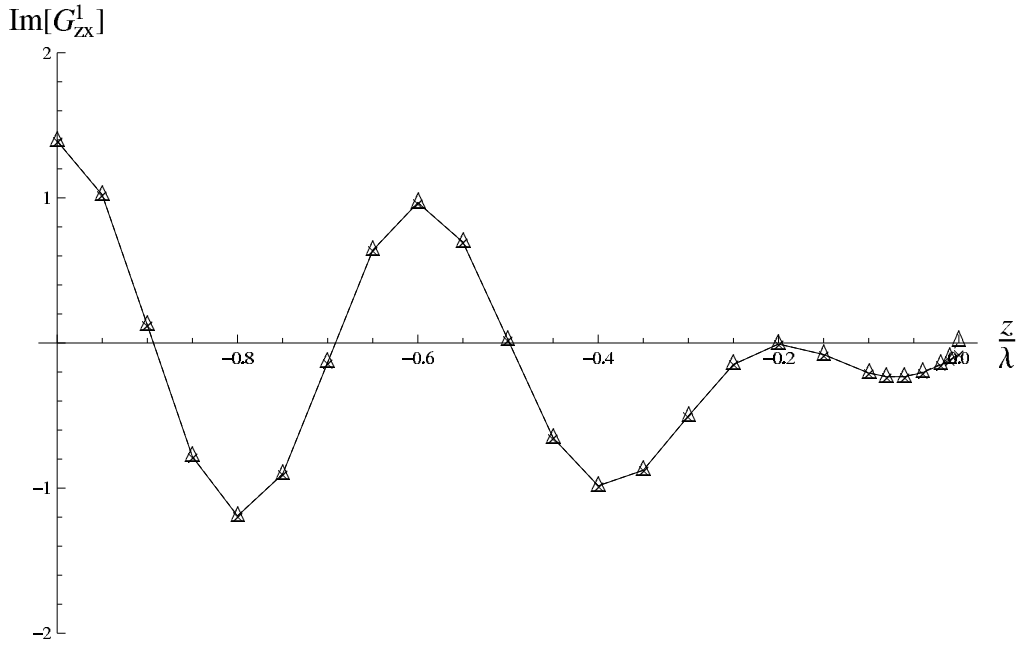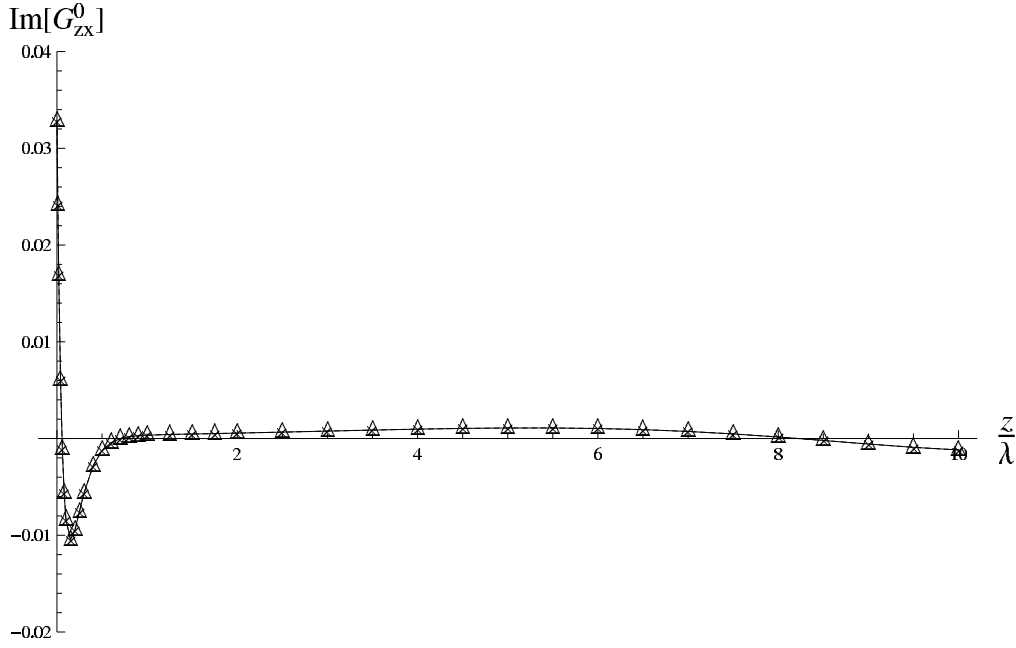
also implemented in *MATHEMATICA*. The difference in executing the two cases was that in direct numerical integration via *MATHEMATICA*, the pole locations needed to be defined as input. In the former case this was not necessary, as the singularity subtraction generates a smooth behavior of the integrand.

The results in these figures show remarkably good agreement between the two approaches. The interesting feature in these results is noticeable in the change in the nature of both $\Re e[G_{zx}(\rho, z, \phi)]$ and $\Im m[G_{zx}(\rho, z, \phi)]$ near $z/\lambda \approx 0$ or at the interface. This distinction is obvious by the rapid transition in the functional behavior, and can be attributed to the Stokes phenomenon [88, 89] (this Stokes behavior will be investigated in more details for the double layer case, in a later report). Obviously, if there were additional layers then such "discontinuities" (rapid transitions) would be more pronounced and capturing accurately this behavior would be difficult for multiple-layers.

The computational differences in the two approaches is obvious from the results in Fig. 27, from which one can easily conclude that the real-axis integration employing the singularity subtraction method would be much more efficient. This method, *i.e.* Eq. (32), takes significantly less time compared to direct numerical integration for large ρ and hence appears better suited for calculations involving large lateral separations. For direct numerical integration, the traditional real axis integration [56] can be modified to move the portion of the contour "slightly above" the $\Re e(\xi)$ axis as in Ref. [57] to avoid computation of the poles. In that case, if the *MATHEMATICA* software was used, it would not require any a-priori input for the pole locations. However, it was verified that in this case direct integration via *MATHEMATICA* would still be more time consuming then the algorithm in Eq. (32).
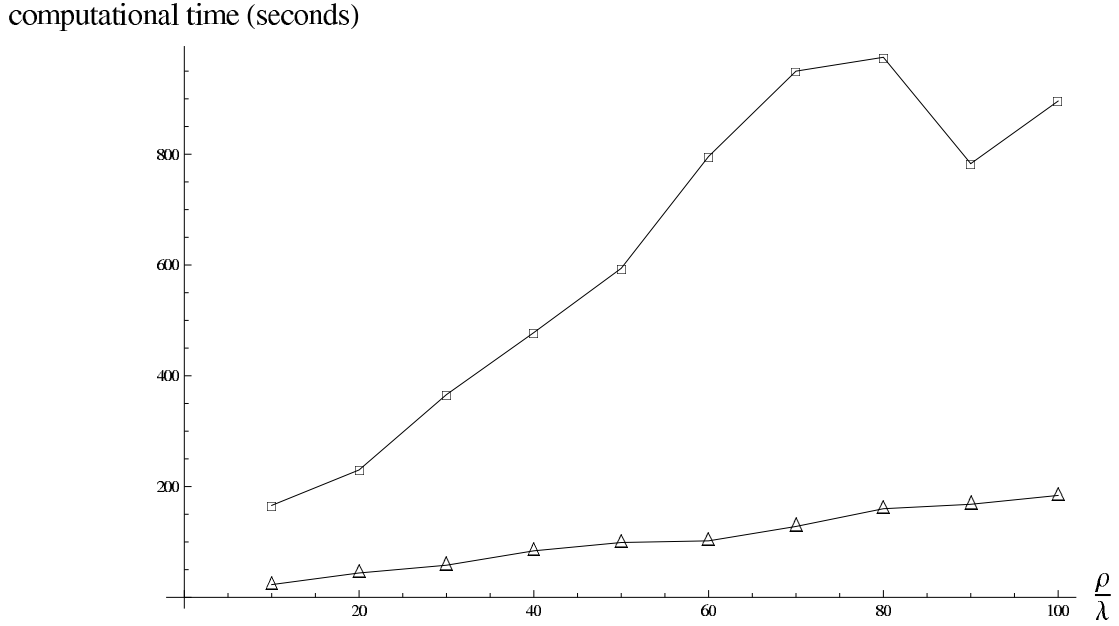
computational time (seconds)

Fig. 27 — Comparison of cpu times between direct *MATHEMATICA* ($\square - \square$) computation and the algorithm based on Eq. (32)($\triangle - \triangle$) with variation in lateral distance $\frac{\rho}{\lambda}$. The data refers to $|\varepsilon_r| = 9.8$, $\tan \delta = 0.0001$, $d/\lambda = 1$; for each value of ρ, the G_{zx} was calculated for $\phi = 0°$, and 63 datapoints in the range $-\lambda \leq z \leq 10\lambda$.

Some observations regarding the real-axis integration of Sommerfeld integrals via equations Eqs. (32) and (33) appear important. Though Eq. (32) is stable because the resulting integrand (as shown in Figs. 17 and 18) is well-behaved after singularity subtraction, the oscillatory behavior for $\xi\rho \rightarrow \infty$ cannot be completely eliminated. In Ref. [57] the asymptotic behavior of $J_0(\xi\rho)$ was used for closed form evaluation of the tail beyond the chosen breakpoint ξ_A; however, it does not appear that the method is well suited for values of lateral separations where $\rho \approx 1000\lambda$. This is because the oscillatory behavior dominates for very small values of the spectral parameter ξ and hence can "corrupt" any direct numerical evaluation of Sommerfeld integral. The only exceptions appear to be the discrete complex image method [66-68] in conjunction with the matrix pencil method [58, 59], where no numerical evaluation of Sommerfeld integral is necessary.

To that end, it appears important that an analytical solution (even with its attendant approximations) for $\xi\rho \rightarrow \infty$ is relevant. Limited useful analytical formulations are available [63, 64]. The solution in Ref. [63] is valid only when both the source and observer are exactly on the air-substrate interface and for single layer substrate. Similarly the solution in Ref. [64] has restrictions in terms of locations of source and observer points. Thus Refs. [63, 64] are directly *inapplicable* for arbitrary variations in z/λ shown in Figs. 19 to 26. But, both Refs. [63, 64] are valid for large ρ separations. To obtain a *single* solution that is simultaneously valid for continuous z/λ *and* also when $\rho \rightarrow \infty$ is a challenging task because results in this chapter show that an accurate solution near the Stokes surfaces needs to account for arbitrary electrical thickness and optical densities (*i.e.*, arbitrary values of ε_r and μ_r). This aspect requires application of more sophisticated asymptotic techniques such as in Refs. [42-44, 87, 88, 90, 94-100] for improved evaluation of the Sommerfeld integrals in a multilayered media.

3.   PHASE-INTEGRAL TECHNIQUE FOR THE G_{zx} GREEN'S FUNCTION IN CONTINUOUSLY STRATIFIED PEC-TERMINATED MEDIA

The G_{zx} Green's function for a horizontally oriented Hertzian electric current element in a single or multilayered PEC-terminated media contains Sommerfeld integrals, as shown in Chapter 2, and takes different mathematical forms depending on the location of the observation position. If the media is continuously stratified, say along the z-direction, the representation of the fields, for arbitrary source and observer locations, through the use of Sommerfeld integrals becomes very tedious. The reason is that the continuously stratified media then needs to be discretized into several layers each with different complex wavenumbers. The information gleaned from the analysis in Chapter 2 indicates that such an attempt to obtain electromagnetic fields through discretization of a continuously layered media is an extensively laborious task. If the number of layers exceed three, the computational process becomes very complicated.

In this chapter, a mathematically rigorous alternative [16-20] known as the *Phase-Integral* method is developed that utilizes the continuously varying nature of the wavenumber. This means that for a z-stratified media the wavenumber variation along the z-direction is continuous and is retained without any discretization of the layered media. Earlier work [1-5, 14, 21-27] on wave propagation in layered media had extensively utilized the Phase-Integral approach.

In what follows, the electromagnetic fields due to a Hertzian electric current element is derived for a medium which has continuously varying constitutive parameters, *i.e.*, $\varepsilon(z)$ and $\mu(z)$, along the z-direction. The various scalar components of the corresponding dyadic Green's functions for a continuously varying media are also obtained. This is followed by the contour integral representation of the three-dimensional Green's function for a z-stratified media. The one dimensional characteristic Green's function is derived for the z-stratified media, and this derivation utilizes the Phase-Integral or Wentzel-Kramers-Brillouin (WKB) method accounting for the continuous profile of the relevant constitutive parameters. The mathematical aspects of the general formulation for stratified media are presented here from Ref. [35], and from Refs. [16, 17] for the WKB and Phase-Integral solutions to ordinary differential equations.

3.1   Green's Functions Due to a x-Directed Horizontal Electric Dipole in a Continuously z-Stratified Media

The electric field due to an arbitrarily oriented electric and/or magnetic Hertzian current element is given in terms of electric and magnetic Hertz potentials, $\Pi_{e,m}$, from Ref. [35, p. 573] that read

$$\vec{\mathbf{E}}(\vec{r},\vec{r}') = \frac{\varepsilon(z')}{\varepsilon(z)}\{\nabla \times \nabla \times \hat{\mathbf{z}}\Pi_e\} - j\omega\mu(z')\{\nabla \times \hat{\mathbf{z}}\Pi_m\}. \tag{35}$$

The ∇ differential operator in Eq. (35) operates on the observation (unprimed) point coordinates. The continuous variation of the constitutive parameters along the z-direction indicates the electrical or optical inhomogeneity of the ambient medium (a similar relation for the magnetic field can be found in Ref. [35, p. 573, Eq. 1b], but is irrelevant here and thus omitted for brevity). If both electric and magnetic current elements (Hertzian dipoles) are considered as sources for the electromagnetic fields, then the corresponding

Hertz potentials are given by Ref. [35, p. 573, Eqs. 1c, 1d]

$$j\omega\varepsilon(z')\Pi_e = \frac{1}{j\omega\varepsilon(z')}\{\vec{\mathbf{J}}_0 \bullet \nabla' \times \nabla' \times \hat{\mathbf{z}}\zeta_e\} - \{\vec{\mathbf{M}}_0 \bullet \nabla' \times \hat{\mathbf{z}}\zeta_e\},$$

$$j\omega\mu(z')\Pi_m = \{\vec{\mathbf{J}}_0 \bullet \nabla' \times \hat{\mathbf{z}}\zeta_m\} + \frac{1}{j\omega\mu(z')}\{\vec{\mathbf{M}}_0 \bullet \nabla' \times \nabla' \times \hat{\mathbf{z}}\zeta_m\}. \tag{36}$$

Unlike ∇ in Eq. (35), ∇' operates on the coordinates of the source (primed) location. The $\bullet$ indicates a vector dot (scalar) product. Our objective is to show how the preceding formulation would reduce to the general expressions for the electric fields for a single layered, PEC-backed microstrip patch antenna as in Ref. [65, Eqs. 1-13]. In Eq. (36) the $\zeta_{e,m}$ are the *scalar* electric (e) and magnetic (m) potentials. To that end, for an electric source, *i.e.*, setting $\vec{\mathbf{M}}_0 = 0$ in Eq. (36), one performs the following algebraic operations for an arbitrarily oriented Hertzian electric current element, $\vec{\mathbf{J}}_0 = \vec{\mathbf{J}}_t + \hat{\mathbf{z}}\mathbf{J}_z$, that are

$$\nabla' \times \nabla' \times \hat{\mathbf{z}}\zeta_e = \nabla'_t\left(\frac{\partial\zeta_e}{\partial z'}\right) - \hat{\mathbf{z}}(\nabla'^2_t\zeta_e),$$

$$\vec{\mathbf{J}}_0 \bullet (\nabla' \times \nabla' \times \hat{\mathbf{z}}\zeta_e) = \vec{\mathbf{J}}_t \bullet \left(\nabla'_t\frac{\partial\zeta_e}{\partial z'}\right) - \mathbf{J}_z\nabla'^2_t\zeta_e,$$

$$\vec{\mathbf{J}}_0 \bullet \nabla' \times \hat{\mathbf{z}}\zeta_m = [\vec{\mathbf{J}}_t \bullet (\nabla' \times \hat{\mathbf{z}}) + \hat{\mathbf{z}} \bullet (\nabla' \times \hat{\mathbf{z}})\mathbf{J}_z]\zeta_m$$

$$= [\vec{\mathbf{J}}_t \bullet (\nabla' \times \hat{\mathbf{z}})]\zeta_m$$

$$= [\vec{\mathbf{J}}_t \bullet (\nabla'_t \times \hat{\mathbf{z}}) + \vec{\mathbf{J}}_t \bullet (\hat{\mathbf{z}}\frac{\partial}{\partial z'} \times \hat{\mathbf{z}})]\zeta_m$$

$$= -(\vec{\mathbf{J}}_t \times \hat{\mathbf{z}}) \bullet \nabla'_t\zeta_m. \tag{37}$$

In the preceding equations, $\nabla \equiv \nabla_t + \hat{\mathbf{z}}\frac{\partial}{\partial z}$ and $\nabla' \equiv \nabla'_t + \hat{\mathbf{z}}\frac{\partial}{\partial z'}$. In Eq. (37), one notes the application of the following vector identities, *viz.*,

$$\hat{\mathbf{z}} \bullet (\nabla' \times \hat{\mathbf{z}}) = \nabla' \bullet (\hat{\mathbf{z}} \times \hat{\mathbf{z}}) = 0,$$

$$\vec{\mathbf{J}}_t \bullet (\nabla'_t \times \hat{\mathbf{z}}) = \nabla'_t \bullet (\hat{\mathbf{z}} \times \vec{\mathbf{J}}_t) = -(\vec{\mathbf{J}}_t \times \hat{\mathbf{z}}) \bullet \nabla'_t,$$

has been used to simplify some of the intermediate steps. For the case of a x-directed Hertzian electric current element, $\mathbf{J}_z = 0$ and $\vec{\mathbf{J}}_t = \hat{\mathbf{x}}\mathbf{P}_e$. Using Eq. (37) one finds the reduced forms for the Hertz potentials for a x-directed Hertzian current element from Eq. (36) are given by

$$\Pi_e = \mathbf{P}_e\frac{1}{[j\omega\varepsilon(z')]^2}\frac{\partial^2\zeta_e}{\partial x'\partial z'},$$

$$\Pi_m = \mathbf{P}_e\frac{1}{j\omega\mu(z')}\frac{\partial\zeta_m}{\partial y'}. \tag{38}$$

The scalar version of Eq. (35) reads in terms of the Hertz potentials, upon its reduction, as

$$E_x = \frac{\varepsilon(z')}{\varepsilon(z)}\frac{\partial^2 \Pi_e}{\partial x \partial z} - j\omega\mu(z')\frac{\partial \Pi_m}{\partial y},$$

$$E_y = \frac{\varepsilon(z')}{\varepsilon(z)}\frac{\partial^2 \Pi_e}{\partial y \partial z} - j\omega\mu(z')\frac{\partial \Pi_m}{\partial y},$$

$$E_z = -\frac{\varepsilon(z')}{\varepsilon(z)}\nabla_t^2 \Pi_e. \tag{39}$$

In Ref. [35, p. 573, Eq. 2] the Green's function for a continuous, uniaxially z-stratified media, corresponding to scalar Hertz potentials $\zeta_{e,m}$ are defined as

$$\nabla_t^2 \zeta_e = -j\omega\varepsilon(z')\mathscr{G}_e(r,r'),$$

$$\nabla_t^2 \zeta_m = -j\omega\mu(z')\mathscr{G}_m(r,r'). \tag{40}$$

Substituting Eq. (38) into Eq. (39) for Π_e and interchanging the primed (source) and unprimed (observation) differential operators, one can obtain the following

$$E_z = P_e \frac{1}{j\omega\varepsilon(z)\,j\omega\varepsilon(z')}\frac{\partial^2}{\partial x \partial z'}[\nabla_t^2 \zeta_e] \tag{41}$$

In arriving at Eq. (41) use has been made of the artifice $\partial/\partial x = -\partial/\partial x'$. One can obtain, in a similar manner, the following expressions using Eq. (38) that reads

$$\frac{\varepsilon(z')}{\varepsilon(z)}\frac{\partial^2 \Pi_e}{\partial y \partial z} = \frac{-P_e}{j\omega\varepsilon(z)\,j\omega\varepsilon(z')} \times \frac{\partial^2}{\partial x \partial y}\left(\frac{\partial^2 \zeta_e}{\partial z \partial z'}\right)$$

$$j\omega\mu(z')\frac{\partial \Pi_m}{\partial x} = -P_e\frac{\partial^2 \zeta_m}{\partial x \partial y}$$

$$\frac{\varepsilon(z')}{\varepsilon(z)}\frac{\partial^2 \Pi_e}{\partial x \partial z} = \frac{-P_e}{j\omega\varepsilon(z)\,j\omega\varepsilon(z')} \times \frac{\partial^2}{\partial x^2}\left(\frac{\partial^2 \zeta_e}{\partial z \partial z'}\right)$$

$$j\omega\mu(z')\frac{\partial \Pi_m}{\partial y} = -P_e\frac{\partial^2 \zeta_m}{\partial y^2}$$

$$= -P_e[-\nabla_t^2 \zeta_m + \frac{\partial^2 \zeta_m}{\partial x^2}] \tag{42}$$

In arriving at Eq. (42) use has been made of the relationship, $\partial/\partial t = -\partial/\partial t'$, where the label $t \implies x, y, z$. Substituting Eq. (42) in Eq. (39), one obtains the electric fields due to the x-directed horizontal electric dipole, *i.e.*, for which $\vec{J}_0 = \vec{J}_t = \hat{x}P_e$. Once these fields are obtained the scalar components of the dyadic Green's functions for the continuously stratified media can be obtained from Eq. (2) in Chapter 2, with $P_e = p_x$ and setting $p_y = 0$ identically, therein. Additionally in Eq. (2), in view of Eq. (39) one performs the

following replacements: $E_{xx} \to E_x$, $E_{yx} \to E_y$, and $E_{zx} \to E_z$. Then, in their final forms, the complete scalar Green's functions reads

$$G_{xx} = \frac{j}{k\eta_0} \left[\nabla_t^2 \zeta_m - \frac{\partial^2}{\partial x^2} \left(\zeta_m + \frac{1}{j\omega\varepsilon(z) j\omega\varepsilon(z')} \frac{\partial^2 \zeta_e}{\partial z \partial z'} \right) \right]$$

$$G_{yx} = \frac{-j}{k\eta_0} \left[\frac{\partial^2}{\partial x \partial y} \left(\zeta_m + \frac{1}{j\omega\varepsilon(z) j\omega\varepsilon(z')} \frac{\partial^2 \zeta_e}{\partial z \partial z'} \right) \right]$$

$$G_{zx} = \frac{j}{k\eta_0} \left[\frac{1}{j\omega\varepsilon(z) j\omega\varepsilon(z')} \frac{\partial^2}{\partial x \partial z'} (\nabla_t^2 \zeta_e) \right]. \tag{43}$$

These scalar Green's functions are valid for a continuously stratified media, as well as for multipart/multilayered media which has piecewise constant permittivity and permeability, ε_n and μ_n, respectivly, for the nth layer of thickness h_n. The results in Eq. (43) bear close resemblances with the x-, y- and z-components of the electric fields excited by a horizontal electric current element located at the air-dielectric interface of a PEC-backed substrate as in Ref. [65].

It is noted that the Green's functions components $G_{xx,yx,zx}$ in Eq. (43) are the scalar components of the general *dyadic* Green's functions for the electromagnetic problem [34; 38, chap. 2; 39]. In general, for an arbitrary source, the scalar components in Eq. (2) are nine in number, and all the nine scalar components need to be found for this general case. However, the *scalar* potential Green's functions are strictly related to an arbitrarily oriented electric or magnetic source. For the electric (or magnetic) Hertz potential, there is the corresponding electric plus magnetic potential Green's function [35, p. 573, Eqs. 1c, 1d]. Thus, for an arbitrarily oriented electric source there are 3×3 scalar components of the dyadic Green's function. But, regardless of the source, there always exists only two types of potential Green's functions which are, of course, scalar. The nine scalar components of the dyadic Green's functions are expressed in terms of the two Hertz potentials or equivalently the two potential Green's functions. This fact is to be borne in mind to avoid confusion while seeking relationship between Eqs. (38) and (2).

What we next need to calculate are the $\mathcal{G}_{e,m}$ Green's Functions in Eq. (40) and the $\zeta_{e,m}$ scalar potential functions in Eq. (38). The outline of the solution to $\mathcal{G}_{e,m}$ Green's functions is described below, along with the corresponding calculations for $\zeta_{e,m}$. No attempt is made to solve the electromagnetic boundary value problem for a continuously stratified media in the most complete fashion. However, the general outline of the overall solution is described here. The solution procedure for the continuously stratified media problem is for the major part obtained from Ref. [35, chaps. 3, 5] and for the minor part from Ref. [38, chap. 2].

One of the main reasons for the above is that the profiles for $\varepsilon(z)$ and $\mu(z)$ are unknown. Additionally, the general solution approach would still need to be validated and numerically implemented with the state-of-art analysis techniques. This in itself is a formidable effort because of the various constraints that need to be met for the practical utility of the of the proposed solution approach. Thus, such specific investigations are best left for future work in this area.

3.2   Contour Integral Representations of 3-Dimensional $\mathcal{G}_{e,m}$ Green's Functions in Eq. (40)

From Ref. [35, chap. 3, pp. 284-288, Eq. 37] the electric or magnetic potential Green's functions can be synthesized in terms of three one-dimensional (transmission line) characteristic Green's functions,

$G_x^{e,m}(x,x';\lambda_x)$, $G_y^{e,m}(y,y';\lambda_y)$ and $G_z^{e,m}(z,z';\lambda_z)$, as follows

$$\mathscr{G}_{e,m}(r,r') = \frac{-1}{4\pi^2} \oint_{C_x} G_x^{e,m}(x,x';\lambda_x)d\lambda_x \oint_{C_y} G_y^{e,m}(y,y';\lambda_y)G_z^{e,m}(z,z';\lambda_z)d\lambda_y. \tag{44}$$

In Eq. (44), $\lambda_z = k^2(z) - \lambda_x - \lambda_y$ for a continuously layered media, as evidenced by the continuous variation of the wavenumber k(z). The contours $C_{x,y}$ in the complex $\lambda_{x,y}$ planes are explicitly defined in accordance with the singularities of the individual $G_{x,y}^{e,m}$ functions [35, p. 284 ; 38, chap. 2, p. 86]. The various $\lambda_{x,y}$ are the spectral wavenumbers whose explicit relationship to the one-dimensional Green's functions are defined via the one-dimensional Sturm-Liouville operator equation [35, p. 274, Eq. 1] as

$$\left[\frac{d}{ds}\left\{p(s)\frac{d}{ds}\right\} - q(s) + \lambda_s w(s)\right] g_s(s,s';\lambda_s) = -\delta(s-s'). \tag{45}$$

In Eq. (45) the generic variable $s \Longrightarrow (x,y)$ as appropriate, and the superscripts *e,m* have been dropped. It is emphasized that *x* and *y* coordinates are transverse to the direction of stratification. One notes that the continuously stratified media is in the semi-infinite domain along the z-axis. Boundary conditions are imposed along the direction of stratification. In the orthogonal, *i.e.*, x-y planes there are no boundary conditions to be met, and the solutions to Eq. (45) should physically represent outgoing plane waves. The determination of $G_z(z,z';\lambda_z)$ is presented in a separate section.

For the x- and y-component of the characteristic Green's function appearing in Eq. (44), a reduced form of Eq. (45) can be obtained by setting $p(x) \equiv p(y) \equiv p(s) = 1$, $w(s) \equiv w(x) \equiv w(y) = 1$ and $q(s) \equiv q(x) \equiv q(y) = 0$. The explicit forms for the reduced version of Eq. (45) are

$$\left(\frac{d^2}{dx^2} + k_x^2\right) g_x = -\delta(x-x'),$$

$$\left(\frac{d^2}{dy^2} + k_y^2\right) g_y = -\delta(y-y'), \tag{46}$$

for both x- and y- characteristic green's functions. Comparing Eq. (46) with Eq. (45) one notes that the "unspecified" eigenvalue $\lambda_{x,y} = k_x^2$ or k_y^2 as appropriate. Because of the absence of any boundary conditions, the spectrum is continuous, *viz.,* $-\infty \leq k_{x,y} \leq +\infty$, one can assume that this problem is of the type SLP3 [39, chap. 2, pp. 77-94], with a *limit point* or *limit circle* case. This involves solving the corresponding homogeneous equation and finding the basis solutions for the two regions on either side of $x = x'$ (or $y = y'$). For the corresponding homogeneous equation in Eq. (46), the relevant important details to obtain the g_x Green's function following Ref. [38, chap. 2, p. 64] are presented next. The modal eigenfunctions are

$$\Phi_1(x > x') = A_1 e^{-jk_x(x-x')},$$

$$\Phi_2(x < x') = A_2 e^{-jk_x(x'-x)},$$

where the Wronskian is

$$\mathscr{W}(x') = 2jk_x A_1 A_2,$$

and the one-dimensional characteristic Green's functions in Eq. (44) are

$$g_x(\mathrm{x},\mathrm{x}';\lambda_x = \mathrm{k}_x^2) = \frac{j}{2\mathrm{k}_x}e^{-j\mathrm{k}_x|\mathrm{x}-\mathrm{x}'|},$$

$$g_y(\mathrm{y},\mathrm{y}';\lambda_y = \mathrm{k}_y^2) = \frac{j}{2\mathrm{k}_y}e^{-j\mathrm{k}_y|\mathrm{y}-\mathrm{y}'|}. \tag{47}$$

We have not yet determined $G_z^{e,m}(\mathrm{z},\mathrm{z}';\lambda_z)$ in Eq. (44), and this is the subject of the next section. Before proceeding further, we note that $\lambda_z = k^2(\mathrm{z}) - k_x^2 - k_y^2 = \kappa^2 = k^2(\mathrm{z}) - \beta^2$. Moving further we note that the one dimensional x- and y-characteristic Green's functions in Eq. (47) are the indistinguishable for electric (superscript e) and magnetic (superscript m) cases, because the corresponding modal eigenfunctions are indistinguishable [35, chap. 3, p. 251, Eq. 40b]. The difference between the two arises in the calculation of $g_z^{e,m}(\mathrm{z},\mathrm{z}';\lambda_z)$ and will be discussed later.

Continuing with the completion of the calculation for $\mathscr{G}_{e,m}(r,r')$ in Eq. (44), substitute from Eq. (47) and noting that $d\lambda_{x,y} \equiv d(k_{x,y}^2) = 2k_{x,y}dk_{x,y}$, the final result reads

$$\mathscr{G}_{e,m}(r,r') = \frac{+1}{4\pi^2}\int\limits_{-\infty}^{+\infty}dk_y\int\limits_{-\infty}^{+\infty}dk_x e^{-j[k_x|\mathrm{x}-\mathrm{x}'|+k_y|\mathrm{y}-\mathrm{y}'|]}G_z^{e,m}(\mathrm{z},\mathrm{z}';\lambda_z) \tag{48}$$

Following Ref. [35], the polar transformations

$$\begin{aligned}
k_x &= \beta\cos\alpha, & \mathrm{x} &= \rho\cos\phi, & \mathrm{x}' &= \rho'\cos\phi', \\
k_y &= \beta\sin\alpha, & \mathrm{y} &= \rho\sin\phi, & \mathrm{y}' &= \rho'\cos\phi', \\
dk_x dk_y &= \rho\,d\rho\,d\phi, & & & &
\end{aligned} \tag{49}$$

are now used in Eq. (48) to obtain the following form

$$\mathscr{G}_{e,m}(r,r') = \frac{+1}{4\pi^2}\int\limits_0^{+\infty}\beta\,d\beta\,G_z^{e,m}(\mathrm{z},\mathrm{z}';\beta)\int\limits_0^{+2\pi}d\alpha\exp\{-j\beta\rho\cos(\alpha-\phi)\}\exp\{+j\beta\rho'\cos(\alpha-\phi')\} \tag{50}$$

where $0 \le \rho \le +\infty$ and $0 \le \phi \le 2\pi$. To simplify Eq. (50), without any loss of generality of the physics of the problem, one may conveniently choose the horizontal electric dipole at the origin of the coordinate system, so that $\rho' = 0$ in Eq. (50). In Eq. (50) it is emphasized that

$$G_z^{e,m}(\mathrm{z},\mathrm{z}';\beta) \equiv G_z^{e,m}(\mathrm{z},\mathrm{z}';\lambda_z) = \sqrt{k^2(\mathrm{z})-\beta^2}.$$

This means that $G_z^{e,m}$ is an even function of β. Thus $G_z^{e,m}(\mathrm{z},\mathrm{z}';-\beta) = G_z^{e,m}(\mathrm{z},\mathrm{z}';+\beta)$. Substituting the Bessel function identity

$$\exp[-j\beta\rho\cos(\alpha-\phi)] = \sum_{n=-\infty}^{+\infty}(j)^{-n}\mathrm{J}_n(\beta\rho)e^{+jn(\alpha-\phi)} \tag{51}$$

in Eq. (50) with $\rho' = 0$ therein, one can obtain the simplified result as shown in the following

$$\mathcal{G}_{e,m}(r,r') = \frac{+1}{4\pi^2} \sum_{n=-\infty}^{+\infty} (j)^{-n} e^{-jn\phi} \int_0^{+\infty} G_z^{e,m}(z,z';\beta) J_n(\beta\rho) \beta \, d\beta \int_0^{+2\pi} e^{+jn\alpha} \, d\alpha. \tag{52}$$

With the following result, *viz.*,

$$\int_0^{2\pi} e^{+jn\alpha} \, d\alpha = \begin{cases} 2\pi, & \text{when } n = 0 \\ 0, & \text{when } n \neq 0 \end{cases} \tag{53}$$

substituted in Eq. (52), only the $n = 0$ term survives in the series, and one finally obtains

$$\mathcal{G}_{e,m}(r,r') = \frac{+1}{2\pi} \int_0^{+\infty} G_z^{e,m}(z,z';\beta) J_0(\beta\rho) \beta \, d\beta. \tag{54}$$

Furthermore we make use of the following well-known relations for the cylindrical Bessel and Hankel functions

$$J_0(\beta\rho) = \frac{1}{2}[H_0^{(1)}(\beta\rho) + H_0^{(2)}(\beta\rho)]$$

$$H_0^{(1)}(-z) = -H_0^{(2)}(z) \tag{55}$$

in Eq. (54) to obtain the following form that reads as follows

$$\mathcal{G}_{e,m}(r,r') = \frac{+1}{4\pi} \left\{ \int_0^{+\infty} G_z^{e,m}(z,z';\beta) H_0^{(2)}(\beta\rho) \beta \, d\beta + \int_0^{+\infty} G_z^{e,m}(z,z';\beta) H_0^{(1)}(\beta\rho) \beta \, d\beta \right\}. \tag{56}$$

The last integral in Eq. (56) can be conveniently grouped with the first one by the substitution $\beta \to -\beta$ and further use of Eq. (55). This *final* reduced result for Eq. (56) reads

$$\mathcal{G}_{e,m}(r,r') = \frac{+1}{4\pi} \int_{-\infty}^{+\infty} G_z^{e,m}(z,z';\beta) H_0^{(2)}(\beta\rho) \beta \, d\beta$$

$$= \frac{+1}{4\pi} \int_{\infty e^{+j\pi}}^{+\infty} G_z^{e,m}(z,z';\beta) H_0^{(2)}(\beta\rho) \beta \, d\beta. \tag{57}$$

In Eq. (57) the lower limit of the last integral indicates that the original real axis path of integration has been slightly deformed to go anti-clockwise and also this change implies that the path of integration is slightly below the negative real axis to avoid the logarithmic branch point singularity of the $H_0^{(2)}(z)$ function near $z \approx 0$.

The result Eq. (57) allows one to calculate components of the dyadic Green's function in Eq. (43). However one still needs the explicit forms for potential functions $\zeta_{e,m}$ and from Ref. [35, pp. 573-574, Eqs. 5a, 5b] they read,

$$\zeta_{e,m} = \sum_i \frac{\Phi_i(\rho)\Phi_i^\star(\rho')}{\beta^2} g_z^{e,m}(z,z';\beta). \tag{58}$$

Thus, this completes the complete plan for calculating the fields due to a horizontal electric dipole in a layered media given by Eq. (35). The Phase-Integral method discussed next.

3.3   Application of the Phase-Integral Technique to the Green's Function in Eq. (57)

The complete solution to a continuously layered media, as provided in Eq. (57), needs to account for the radiation condition and the boundary condition at the PEC. To that end, these conditions are included in the z-stratification and hence in the determination of the one-dimensional $G_z^{e,m}(z,z';\beta)$ characteristic Green's function. Following Ref. [35, p. 574, Eqs. 5.87a, b], the differential equation

$$\left[\frac{d^2}{dz^2} + p(z)\frac{d}{dz} + q(z) \right] G_z(z,z';\beta) = -\delta(z-z') \tag{59}$$

needs to be solved, with appropriate boundary conditions, for $g_z(z,z';\beta)$. In Eq. (59) the superscripts have been dropped, and also

$$p(z) = \begin{cases} \frac{-\epsilon'(z)}{\epsilon(z)}, & \text{for electric type,} \\ \frac{-\mu'(z)}{\mu(z)}, & \text{for magnetic type} \end{cases} \tag{60}$$

Green's functions. The single primes in Eq. (60) are for first (single) derivatives and $q(z) = \kappa^2(z) = k^2(z) - \beta^2$ in Eq. (59). It is obvious that the solution to the one-dimensional $G_z(z,z';\beta)$ Green's function can be related to the eigenfunction solution to the corresponding homogeneous differential equation to Eq. (59) that reads

$$\left[\frac{d^2}{dz^2} + p(z)\frac{d}{dz} + q(z) \right] \mathscr{K}(z) = 0. \tag{61}$$

Once appropriate eigenfunction solutions to Eq. (61) are obtained, the $G_z(z,z';\beta)$ in Eq. (59) can be obtained via the method in Ref. [38, p. 64, Method II]. Thus, for the rest of this chapter our focus is on obtaining solutions to Eq. (61) rather than Eq. (59).

At this stage the complete solution to Eq. (61), and hence to Eq. (57) is not provided, because many issues in developing an engineering solution are yet to be specified. But, it is important to show how the continuous stratification of the wavenumber $k(z)$ enters the final calculation for either the electric or magnetic type Green's function in Eq. (57). With the use of the solution to Eq. (59), one can calculate the fields located *arbitrarily* inside or outside the layered medium. The advantage of the proposed Phase-Integral formulation is that it is a *single* formulation, and is valid at arbitrary locations. Unlike the piecewise continuous discretization formulation as in Ref. [11] for a two/three layer media, the present formulation does not require numerical evaluation of multiple Sommerfeld integrals for various combination of source

and observer locations. It can also be legitimately argued that the attendant algebraic complexities of using the Phase-Integral solution/representation of Eq. (57) does provide substantial savings in computational resources.

The solution to Eq. (59) are outlined from Ref. [17, chap. 14] because this reference provides a clear exposition of the WKB and Phase-Integral method (Langer transformation). The latter, can legitimately be called as a generalization of the conventional WKB method, since the conventional WKB method fails near the *turning points* [16]. The rigorous mathematical justification(s) of the Phase-Integral method is available in Refs. [18-20], and are omitted here for brevity.

Following Ref. [17, p. 360], to obtain a suitable form for solution, the following separability condition, *viz.*,

$$\mathscr{K}(z) \equiv \mathscr{P}(z)\mathscr{U}(z)$$

is substituted in Eq. (61) that, after some straightforward algebra, results in the following equations

$$\mathscr{P}(z) = \varepsilon(z)$$

$$\frac{d^2\mathscr{U}}{dz^2} + [k_0^2 q_1(z) + q_2(z)]\mathscr{U}(z) = 0 \tag{62}$$

where

$$q_1(z) = k_0^2 \left\{ \varepsilon(z)\mu(z) - \frac{\beta^2}{k_0^2} \right\}$$

$$q_2(z) = \frac{1}{2}\left[\frac{\varepsilon''(z)}{\varepsilon(z)}\right] - \frac{3}{4}\left[\frac{\varepsilon'(z)}{\varepsilon(z)}\right]^2. \tag{63}$$

The single and double primes in Eq. (63) refer to first and second derivatives, respectively. The solution for the differential equation in Eq. (62) when the free-space wavenumber $k_0 \to \infty$ is the central subject of the Phase-Integral or WKB method. Indeed this is essentially seeking an high-frequency asymptotic solution [19, 20] to the Green's function defined via Eq. (59). We follow Ref. [17, pp. 362-364] to elaborate the salient features of the methods. The algebraic details can be obtained by following Ref. [17], and hence the basic features of the solution are outlined next.

The solution is obtained by setting

$$\mathscr{U}(z) = \exp\{k_0\mathscr{F}(k_0, z)\},$$

$$\mathscr{F}(k_0, z) = \sum_{m=0}^{+\infty} \frac{f_m}{k_0{}^m}, \tag{64}$$

in the differential equation in Eq. (62). Incidentally the approach here, following Ref. [17], closely parallels Ref. [2, pp. 79-88]. The second equation in Eq. (64) is very much reminiscent of what is known as *Luneburg-Kline* series in geometrical optics [2, p. 90, Eqs. 4.108a, b]. Upon performing the usual substitutions as

shown in Ref. [17, p. 363], one obtains the following results after some routine lengthy algebra

$$f_0 = \pm j \int \sqrt{q_1(z)} dz, \qquad\qquad\qquad\qquad \text{if } q_1(z) > 0;$$

$$= \pm j \int \sqrt{-q_1(z)} dz, \qquad\qquad\qquad\quad \text{if } q_1(z) < 0;$$

$$\mathscr{U}(z) \approx \frac{C_1 \cos[k_0 \int \sqrt{q_1(z)} dz] + C_2 \sin[k_0 \int \sqrt{q_1(z)} dz]}{[q_1(z)]^{\frac{1}{4}}}, \qquad \text{if } q_1(z) > 0;$$

$$\approx \frac{C_3 \exp[k_0 \int \sqrt{-q_1(z)} dz] + C_4 \exp[-k_0 \int \sqrt{-q_1(z)} dz]}{[-q_1(z)]^{\frac{1}{4}}}, \qquad \text{if } q_1(z) < 0. \qquad (65)$$

We note that $\mathscr{U}(z)$ in Eq. (65) is the *first order* approximation, because we have not used the higher order terms as maybe apparent from Eq. (64). The result for $\mathscr{U}(z)$ in Eq. (65) is known as the classical *Wentzel-Kramers-Brillouin* (WKB) approximation [16-18]. The higher order approximations to $\mathscr{U}(z)$ can be obtained following Refs. [18-20], whose algebraic forms are increasingly complex in nature. Normally these are not necessary for a medium with moderately or slowly varying electrical parameters [2].

The WKB solution in Eq. (65) obviously fails when $q_1(z) = 0$, also known as the "*turning points*" or zeros. To circumvent this problem the Langer transformation [15; 17, pp. 375-379] is used. The feature of this approach is that one *single* solution can be obtained that would *qualitatively* match the WKB solutions in Eq. (65) on either sides of a turning point. Rather than elaborate the method with mathematical rigor, which is readily available in Refs. [19, 20], an intutitive physical approach is pursued here, following Ref. [17].

Examining the solution in Eq. (65) and the original differential equation in Eq. (62), we observe that when $q_1(z) < 0$, $\mathscr{U}(z)$ has a oscillatory (sinusoidal) behavior; when $q_1(z) > 0$ the character of $\mathscr{U}(z)$ changes such that it has exponential growth plus decay behavior. Because in the lowest order solution for $\mathscr{U}(z)$, $q_2(z)$ does not appear in Eq. (65), so we can examine the qualitative behavior by obtaining a simplified (reduced) form of the differential equation in Eq. (64) by setting $q_2(z) \equiv 0$ and $q_1(z) = \pm 1$. In that case we have two differential equations that are simplified versions of Eq. (64) and read

$$\frac{d^2 \mathscr{U}}{dz^2} + k_0^2 \mathscr{U}(z) = 0, \text{ for } q_1(z) = 1;$$

$$\frac{d^2 \mathscr{U}}{dz^2} - k_0^2 \mathscr{U}(z) = 0, \text{ for } q_1(z) = -1. \qquad (66)$$

The generic solutions to the two differential equations in Eq. (66) thus read

$$\mathscr{U}(z) = \begin{cases} a_0 \cos(k_0 z) + b_0 \sin(k_0 z), & \text{for } q_1(z) = 1 \\ a_1 \exp(k_0 z) + b_1 \exp(-k_0 z), & \text{for } q_1(z) = -1. \end{cases} \qquad (67)$$

The qualitative nature of the solutions in Eq. (67) is the same as in Eq. (65). By the fundamental theorem of algebra, if a function changes signs then it must vanish somewhere in between the two consecutive sign changes, and this vanishing point is the zero of the function. Thus when $q_1(z) = +1 \rightarrow -1$ it must vanish in some domain of *z*. Now either solution in Eq. (67) is *not* valid near $q_1(z) \approx 0$. This means that when $q_1(z)$

is > 0 and changes to < 0 in Eq. (65) it must vanish, and by the preceding (qualitative) discussion regarding the solutions in Eq. (67), the corresponding qualitatively similar solutions in Eq. (65) shall also be *invalid* near the zeros defined by $q_1(z) = 0$.

Examining the solution in Eq. (67) one notes that for a *uniform* solution valid near the zeros defined by $q_1(z) = 0$ and also when $q_1(z) = \pm 1$, the functional behavior of $\mathscr{U}(z)$ defined by Eq. (66) needs to be expressible in terms of *non-elementary functions* which would reduce to the corresponding elementary functions in the appropriate regions of validity. For the simplest differential equation defined in Eq. (66) a generalized form would be

$$\frac{d^2\mathscr{U}}{dz^2} - k_0^2 z\mathscr{U} = 0. \tag{68}$$

The preceding is Airy's differential equation and can be solved by using Laplace transforms [42, pp. 50-53]. The contour integral representation of the solution quoted from Ref. [42, p. 52, Eq. 2.5.9] reads

$$Ai(s) = \frac{1}{2\pi j}\int_C \exp(-\frac{\tau^3}{3} + s\tau)d\tau$$

$$Bi(s) = j[e^{-j2\pi/3}Ai(se^{-j2\pi/3}) - e^{j2\pi/3}Ai(se^{j2\pi/3})]. \tag{69}$$

The contour C in Eq. (69) begins at $\infty e^{-j2\pi/3}$ and ends at $\infty e^{+j2\pi/3}$ in the complex τ plane. The solution to Eq. (68) is then expressible in terms of Airy functions that read

$$\mathscr{U}(z) = A_0 Ai(z) + B_0 Bi(z). \tag{70}$$

The various formulas for numerical calculation of Airy functions can be found in Ref. [91]. In Eq. (70) the constants A_0, B_0 have absorbed the wavenumber k_0. The dominant (asymptotic) behavior of the Airy functions [17, p. 373; 91] are as below

$$Ai(z) \approx \frac{\exp(\frac{-2}{3}z^{3/2})}{2\sqrt{\pi}z^{1/4}}, \text{ when } z \to +\infty,$$

$$Bi(z) \approx \frac{\exp(\frac{+2}{3}z^{3/2})}{\sqrt{\pi}z^{1/4}}, \text{ when } z \to +\infty,$$

$$Ai(z) \approx \frac{1}{\sqrt{\pi}(-z)^{1/4}} \sin[\frac{2}{3}(-z)^{3/2} + \frac{\pi}{4}], \text{ when } z \to -\infty,$$

$$Bi(z) \approx \frac{1}{\sqrt{\pi}(-z)^{1/4}} \cos[\frac{2}{3}(-z)^{3/2} + \frac{\pi}{4}], \text{ when } z \to -\infty. \tag{71}$$

The preceding asymptotic expansions can be obtained [42, chap. 7] starting with the contour integral representation in Eq. (69). Observe that in light of Eq. (71) the result in Eq. (70) can exhibit both exponential and oscillatory behavior and hence qualitatively the two different solutions given in Eq. (67) appear as valid in their respective regions. However, the general solution in Eq. (70) is valid near the turning points while the various approximations in Eq. (71) are not. This suggests that the one-dimensional turning point problems for a continuously stratified media will contain non-elementary functions as a part of its solution. These

non-elementary functions are valid across turning points and rays in specific directions that pass through these turning points in a complex plane are known as "*Stokes lines*". Across the Stokes lines the WKB solution (which contains elementary functions only, as in Eq. (65)) changes discontinuously and the Phase-Integral solution, which apparently is a generalization of the conventional WKB solution, remains valid. These ideas are further pursued in Refs. [44, 88-90, 98] and there exists a whole new area of research in determination of numerically accurate solutions valid at and near Stokes lines. The results of this chapter are comprehensively discussed next.

3.4   Summary and Discussion

The one-dimensional Green's function, as a solution to Eq. (59), can be formally represented as

$$G_z(z, z'; \beta) = -\frac{\mathscr{K}_1(z_<)\mathscr{K}_2(z_>)}{p(z')\mathscr{W}(z')}$$

$$\mathscr{W}(z') = \mathscr{K}_1(t)\frac{d\mathscr{K}_2(t)}{dt} - \mathscr{K}_2(t)\frac{d\mathscr{K}_1(t)}{dt}\bigg|_{t \equiv z'} \tag{72}$$

following the general form given in Ref. [38, p. 65, Eq. 27]. The eigenfunctions $\mathscr{K}_{i=1,2}(z)$ and the Wronskian $\mathscr{W}(z')$ are assumed to be uniquely determined. Then, together with Eqs. (65), (59), the electric or magnetic potential Green's functions in Eq. (57) can be determined. Note that the feature of the overall solution given by Eq. (57) is that z-stratification is separated from the large lateral separations that are contained as arguments of the Hankel function in Eq. (57). This feature allows examining independent spatial approximations to the potential Green's function.

Normally, a Phase-Integral solution such as in Eq. (57), would need to be treated by asymptotic methods and this entails evaluation of integrals of the form [42, p. 252, Eq. 7.1.1]

$$I(\kappa) = \int_C g(z)e^{\kappa w(z)}dz. \tag{73}$$

The recent trends in research in uniform asymptotic analysis, reviewed comprehensively in Ref. [86], shows that resurgent analysis [90] and hyperasymptotic techniques [94, 95; 99, chap. 6] are the current state-of-art techniques that need to be applied to such electromagnetic problems. The earlier investigations available in Refs. [35, chap. 4; 41-44], which are currently being used do not have such sophistications. The main reason is that across Stokes lines that emanate through turning points, the "compound" asymptotic expansion [88] can be written *generically* as

Compound Asymptotic Expansion $\approx$ Dominant Asymptotic Expansion

$$+ \text{ Stokes Multiplier } \times \text{ Subdominant Asymptotic Expansion} \tag{74}$$

The aspect, useful for numerical calculations, is that across the Stokes lines the subdominant and dominant expansions interchange roles. The dominant term ceases to have any numerical significance while the subdominant term becomes numerically dominant. The Stokes multiplier, which in most cases is the Dawson integral, attains a maximum value of 1 in the neighborhood of the Stokes line. As the observation point

moves away, the subdominant term becomes insignificant again, because the (Stokes multiplier) Dawson integral becomes numerically small. These changes to the numerical value of the Dawson integral happens very rapidly at and around the Stokes lines.

Recent developments with error bounds [94] in steepest descent methods show that expansions to Eq. (73) give errors, $\mathscr{E}$, that are

$$\mathscr{E} \propto \frac{1}{|\kappa|^{N+1}} \qquad \text{for Poincaré type asymptotic expansions [42];}$$

$$\mathscr{E} \propto \exp(-|\kappa|A) \qquad \text{for Stokes type asymptotic expansions, and}$$

$$\mathscr{E} \propto \exp(-2.386|\kappa|A) \qquad \text{from Ref. [94].} \tag{75}$$

The information in Eqs. (74) and (75) is extremely critical for numerical work related to Green's functions in layered media.

4. QUALITATIVE REVIEW OF TECHNIQUES AND SCOPE FOR FURTHER WORK

In this chapter some of the state-of-art techniques for radiation of sources in a piecewise discrete multilayer or uniaxially continuously stratified media terminated in a PEC-backed groundplane, are discussed qualitatively. The features of the Sommerfeld and Phase-Integral approaches are also compared with the others.

4.1 Comparative Review of Some Methodologies

For calculating fields in a layered media, the integral equation approach normally takes preference over differential equation methods [33, 34] because of the stability of the integral equation operator. However, it appears that an analytic form of the Green's function is still necessary. The results in Chapter 2, in particular Eqs. (14–16), indicate that as the observation point moves across the layers the Green's function changes its mathematical form. As the numbers would increase, the nature of the Green's function would get more complicated. This observation also indicates that a straightforward application of the Finite Difference Time Domain (FDTD) method becomes almost impossible even for modest number of layers and at high frequencies. This is due to the fact that FDTD method typically uses the discretization of the layers into cubic cell sizes of $\lambda/20$ side. Smaller size cells would give better accuracy. Thus, as the frequency increases the number of cells can increase to a number which would render computations with FDTD impossible in practical terms. Alternate methods such as the Discrete Complex Image Method (DCIM) [66-68], real-axis integration schemes [56-58, 47-51], and asymptotic techniques [31, 32, 63-65, 80-85] form the major thrust of the research work. Other analytical techniques [69-73] have been gainfully utilized, but these are not very different from the ones cited above. In addition, some of the recent work such as Ref. [73] appear to solve the problem in terms of incomplete Hankel-Lipschitz integrals which are quite involved for numerical calculations. Furthermore, for the problem at hand, see Fig. 2, a reliable solution at extremely large (1000λ) and moderate (10λ) distances is required. It is not known whether the techniques in Refs. [69-73] would be directly applicable, and if they would have any advantage over the existing asymptotic methods. The features of some of the above-mentioned methods are discussed below:

Real-axis Integration [56-58, 47-51]: This method has been applied to the calculation of G_{zx} containing Sommerfeld integrals for single and double layer PEC-backed substrates in Chapter 2 (numerical results for single layer are included). The most important aspect is to calculate the pole locations on the proper Riemann sheet and evaluate the tail part of the spectral integral in closed-form. The method can be applied, in principle, to multiple layers. The primary difficulties are that if the number of layers increase beyond two, location of the poles and calculation of the residues become extremely cumbersome. However, the evaluation of the Sommerfeld integral mostly exact - with no approximations to the Bessel function, unlike in Refs. [51, 57]. Application of the method in Ref. [56] to continuously stratified media, with the Sommerfeld tail part evaluated in closed-form, appears feasible only if such a layered media is discretized into a finite number of layers with piecewise constant electrical parameters.

DCIM [66-68]: The feature of the DCIM is that it utilizes the Sommerfeld-Weyl identity and can express the Green's function in terms of some few exponentials including the image effects [66, Eqs. 12-14]. However, the number of surface waves poles increases as the substrate thickness increases and these effects need to be included [66, Eqs. 15-16]. The DCIM method's primary advantage is that it expresses the Green's function as a sum of finite number of terms. However, an examination of the recent work in Ref. [68] indicates that improvements in reducing the fill-time of the matrix in a MoM solution have been achieved and hence the new methodology of the 2D-DCIM appears very competitive to solve multilayer problems. It must be noted that to date there is no application of the DCIM to continuously stratified media. Indeed, continuously stratified media is discretized into a set of piecewise constant layers and then DCIM can be applied as shown in Ref. [68]. The extension to DCIM to continuously stratified media appears to be a challenging task.

Asymptotic Techniques [31, 32, 63-65, 80-85]: These are by far the most useful methods because they can result in significant reduction of computation times [63]. The difficulty is the limitation in applicability. For example, the results in Ref. [63] are for a single layer substrate, but they are valid for source and observer located at the air-dielectric interface. The reason for this limitation is the nature of the asymptotic reduction employed. In Ref. [63] the modified Sommerfeld integral, via approximation of the Hankel functions, are evaluated for the special case of "simple pole close to a saddle point". Now as the observation point moves from inside the substrate into the air, many other analytic singularities come into a coalescnce. The result is that such a reduction of the Sommerfeld integral as in Ref. [63] becomes invalid for arbitrary source and observer locations. Similar remarks apply to Ref. [64]. The situation is clearly depicted in Refs. [31, 32]. Here it is shown that due to existence of branch points and poles, which can come close to saddle points the resulting uniform asymptotic evaluation shall contain more complicated non-elementary functions such as Weber parabolic cylinder function. Regardless, application of some form of asymptotic techniques appear fruitful when relative geometrical locations between source and observer become very large.

Phase-Integral Methods [16-20] are a part of asymptotic techniques that can be applied to obtain the Green's function for a continuously stratified media (this has been discussed in Chapter 3). The method, when compared against a formulations for discretized layered media with piecewise constant characteristics, yields a *single* Green's function that is valid for *arbitrary* observation and source locations. However, while this technique has been successfully to problems of acoustic, optical and seismic waves propagation in layered media [2-5, 7, 28], its application to electromagnetic wave propagation in layered media with an emphasis on antenna problems appears to be limited [22, 24, 25]. The reason can perhaps be traced back to the apparent mathematical difficulties in accurately evaluating integrals across Stokes lines and caustics. However, with the advent of newly developed asymptotic

methods [86-100], the phase-integral solutions to the layered media Green's function should not be difficult to calculate numerically.

Ray-Mode Methods [80-85] are particularly useful for antenna array problems where the sources maybe embedded inside layered media - as in this situation. The method utilizes both mode and rays for a problem-matched Green's function [80]. The use of infinite or finite Poisson sum formula for the array Green's function is shown to reduce mode to rays and vice versa. Each description, ray and mode, is used in appropriate regions that finally yields best convergence. The method apparently can be applied to inhomogeneous media [83], and needs to be further examined in context of this problem.

4.2 Discussion and Scope for Further Investigations

Some of the important future tasks for this investigation are identified and itemized below. These are by no means exhaustive but appear relevant from the investigations.

Task 1: In this investigation, limited by resources, a method to calculate Sommerfeld integral by performing integration along the real axis has been carried out. However, as shown in Chapter 2, the Bessel function $J_0(\xi\rho)$ was not approximated to calculate the tail part. The Sommerfeld identity (derived in Appendix A) was used. The method of integration is an improvement over the techniques in Refs. [51, 57] but its full efficacy still needs to be realized. Because it can be applied to discretized, piecewise constant multilayer media this work needs to be carried out. This effort, in the least shall provide a reference solution against which results from many other techniques can be compared. Extension to a two-layer media appears straightforward, though the pole locations can cause severe problems.

Task 2: The 2D-DCIM needs to be applied to multilayered media and will also provide a useful parallel reference solution like the real-axis integration. There is no anticipated difficulty because it has been applied to two-layer media [68] (as a separate reference solution the FDTD, for limited cases, needs to be utilized to obtain reference solutions that can be compared against the 2D-DCIM and other methods).

Task 3: Asymptotic techniques, which can include straightforward uniform asymptotic expansions, phase-integral methods and ray-mode techniques appear to be the best approaches for both multilayered and continuously stratified media. In applying the asymptotic techniques, care must be exercised to incorporate recent research in this area such as accurate numerical evaluation of the Green's function across Stokes lines.

Task 4: Because asymptotic techniques, DCIM, and real-axis integration apply to discretized layered media, validation of the various techniques should consider the discretized layered media as an important benchmark problem. Next, the phase-integral method should be formulated for continuously stratified case and compared against the discretized case. Similar remarks apply for the ray-mode technique. As a consequence, a very critical task is to ascertain with some degree of accuracy the effects of rapidly varying permittivity, $\varepsilon(z)$, and permeability, $\mu(z)$, profiles when the continuous variation is discretized.

Task 5: In this report only the G_{zx} component was studied for a horizontal electric current element. The results for an arbitrarily oriented Hertzian current element needs to be found to complete the entire problem. All the preceding methods needs to be applied to obtain solutions for the arbitrarily oriented Hertzian dipole case.

In addition, the methods should also be applied to conformal arrays embedded inside such layered media. The survey of literature [9, ch. 4; 10] in this area indicates that there exists a paucity of useful numerical modeling techniques for such class of array radiators.

5. CONCLUSION

In this report radiation of sources inside layered media, backed by a perfect electric conductor were studied. This problem has practical applications to antennas embedded inside composite material media for many applications. The fields due to a horizontal electric current element were studied by calculating the single G_{zx} component of the dyadic Green's function due to a horizontal electric current element. The traditional real-axis integration method was employed with a new formulation for calculating the Sommerfeld integral tail. This new method contains effects of the intrinsic wavenumber of the layer and hence appears physically more suitable for understanding effects of the various layers when the observation point moves in a vertical direction from one layer to the other. In addition, a new algorithm was developed to calculate the proper surface wave poles for electrically thick substrates. The discontinuities in the integrand of the Sommerfeld integral were eliminated upon subtraction of the residues at these poles, and subsequent numerical integration posed no difficulties. The calculations were also performed via the computer software MATH-EMATICA through direct numerical integration without any preceding modifications. The results from the two approaches showed that the real-axis integration algorithm was at least several times faster compared to direct numerical integration via MATHEMATICA when the lateral separation between the source and observer points increased, with no loss of accuracy. Additionally the problem of stratified media was studied via the Phase-Integral method. It has been shown that the Phase-Integral method, with its attendant asymptotic expansions, has the potential for providing much improved solutions to the Green's functions for continuous media by including effects across the Stokes lines. Finally, some recommendations for further work, based on the present investigations, have been included.

REFERENCES

1.   J. R. Wait, *Electromagentic Waves in Stratified Media*. (Classic Reissue). NJ, USA: IEEE-Wiley Press, 1996.

2. G. Tyras, *Radiation and Propagation of Electromagenetic Waves*. NY, USA: Academic Press, 1969.

3. K. G. Budden, *The Waveguide Mode Theory of Wave Propagation*. NJ, USA: Prentice-Hall, 1961.

4. L. M. Brekhovskikh and O. A. Godin, *Acoustics of Layered Media II: Point Sources and Bounded Beams*. Berlin, Germany: Springer-Verlag, 1999.

5. G. V. Frisk, *Ocean and Seabed Acoustics*. NJ, USA: Prentice-Hall PTR, Inc., 1994.

6. A. K. Bhattacharyya, *Electromagnetic Fields in Multilayered Media: Theory and Applications*. Boston, MA, USA: Artech House, 1994.

7. P. Yeh, *Optical Waves in Layered Media*. Hoboken, NJ, USA: Wiley-Interscience, John-Wiley & Sons, 2005.

8. B. A. Munk, T. W. Kornbau and R. D. Fulton, "Scan Independent Phased Arrays," *Radio Science*, vol. 14, no. 6, pp. 979-990, Nov.-Dec. 1979.

9. L. Josefsson and P. Persson, *Conformal Array Antenna: Theory and Design*. NY, USA: Wiley-IEEE Press, 2006.

10. M. Bosiljevac, P. Persson and Z. Sipus, "Efficient of Aperture Antennas on Generally Shaped Convex Multilayered Surfaces Using a Hybrid SD-UTD Method," *IEEE Trans. Antennas Prop.*, vol. 57, no.5, pp. 1420-1431, May 2009.

11. V. W. Hansen, *Numerical Solution of Antennas in Layered Media*. NY, USA: John-Wiley and Sons, Inc., 1989.

12. J. R. Mosig, R. C. Hall and F. Gardiol, "Numerical Analysis of Microstrip Patch Antennas," (chapter 8) in *Handbook of Microstrip Antennas* (vol. 1), J. R. James and P. S. Hall (eds.). London, UK: IEE Press (Peter Peregrinus), 1989.

13. R. Garg, P. Bhartia, I. J. Bahl and A. Ittipiboon, *Microstrip Antenna Design Handbook*. Boston, MA, USA: Artech House, 2001.

14. T. L. Eckersley and G. Millington, "Application of the Phase Integral Method to the Analysis of Diffraction and Refraction of Wireless Waves Round the Earth," *Phil. Trans. Roy. Soc. Lond.*, series A, vol. 237, issue 778, pp. 273-309, 1938.

15. R. E. Langer, "Asymptotic Solutions of a Differential Equation in the Theory of Microwave Propagation," *Comm. Pure. Appl. Math.*, vol. III, issue 4, pp. 427-438, 1950.

16. J. Heading, *An Introduction to Phase Integral Methods*. NY, USA: John-Wiley and Sons, Inc., 1962.

17. Ali H. Nayfeh, *Introduction to Perturbation Methods*. NY, USA: John-Wiley and Sons, Inc., 1981, 1993 (classic reissue).

18. N. Fröman and P. Fröman, *Physical Problems Solved by the Phase Integral Method*. NY, USA: Cambridge University Press, 2002.

19. M. V. Fedoryuk, *Asymptotic Analysis: Linear Ordinary Differential Equations*. NY, USA: Springer-Verlag, 1993.

20. S. Yu. Slavyanov, *Asymptotic Solutions of the One-Dimensional Schrödinger Equation*. Providence, RI, USA: American Mathemaical Society, 1996.

21. R. Y. S. Lynn and J. B. Keller, "Uniform Asymptotic Solutions of Second Order Linear Differential Equations with Turning Points," *Comm. Pure and Appl. Math.*, vol. XXIII, pp. 379-408, 1970.

22. B. D. Seckler and J. B. Keller, "Asymptotic Theory of Diffraction in Inhomogeneous Media," *Jour. Acous. Soc. Am.*(JASA), vol. 31, no. 2, pp. 206-216, February 1959.

23. B. D. Seckler and J. B. Keller, "Geometrical Theory of Diffraction in Inhomogeneous Media," *Jour. Acous. Soc. Am.*(JASA), vol. 31, no. 2, pp. 192-205, February 1959.

24. E. Bahar, "Generalized WKB Method for Applications to Problems of Propagation in Inhomogeneous Media," *Jour. Math. Phys.*,vol. 8, no. 9, pp. 1735-1746, September 1967.

25. L. Levey and L. B. Felsen, "On Transition Functions Occuring in the Theory of Diffraction in Inhomogeneous Media," *Jour. Inst. Math. Applics.*, vol. 3, pp. 76-97, 1967.

26. Yu. A. Kravtsov, "Two New Asymptotic Methods in the Theory of Wave Propagation in Inhomogeneous Media," *Soviet Physics-Acoustics*, vol. 14, no. 1, pp. 1-17, July-Sept. 1968.

27. C. H. Chapman and R. Drummond, "Body-Wave Seismograms in Inhomogeneous Media Using Maslov Asymptotic Theory," *Bulletin of Seismological Society of America*, vol. 72, no. 6, pp. S277-S317, December 1982.

28. V. Cerveny, *Seismic Ray Theory*. Cambridge, UK: Cambridge University Press, 2001.

29. Richard K. Moore, "Theory of Radio Communication Between Submerged Submarines," *PhD Thesis*, Cornell University, Ithaca, NY, USA, 1951. (See also: R. K. Moore and W. E. Blair, "Dipole Radiation in Conducting Half-Space," *Jour. Res. Nat. Bur. Stands.*, vol. 65D, no. 6, pp. 547-563, Nov.-Dec. 1961.)

30. R. E. Collin,"Hertzian Dipole Radiating over Lossy Earth or Sea: Some Early and Late 20th Century Controversies," *IEEE Antennas and Prop. Mag.*, vol. 46, no. 2, pp. 64-79, April 2004.

31. W. C. Chew and J. A. Kong, "Electromagnetic Field of a Dipole on a Two-Layer Earth," *Geophysics*, vol. 46, no. 3, pp. 309-315, March 1981.

32. W. C. Chew and J. A. Kong, "Asymptotic Approximation of Waves due to a Dipole on a Two-Layer Medium," *Radio Science*, vol. 17, no.3, pp. 509-513, May-June 1982.

33. W. C. Chew, *Waves and Fields in Inhomogeneous Media* (classic reissue). NY, USA: IEEE-Wiley, 1995.

34. W. C. Chew, M. S. Tong and B. Hu, *Integral Equation Methods for Electromagnetic and Elastic Waves*. USA: Morgan & Claypool, 2009.

35. L. B. Felsen and N. Marcuvitz, *Radiation and Scattering of Waves* (classic reissue). NY, USA: IEEE-Wiley, 1994.

36. S. A. Schelkunoff, *Electromagnetic Waves*. NY, USA: D. Van Nostrand Co., Inc., 1943.

37. R. F. Harrington, *Time Harmonic Electromagnetic Fields* (classic reissue). NY: USA: IEEE-Wiley, 2001.

38. R. E. Collin, *Field Theory of Guided Waves*(classic reissue). NY, USA: IEEE-Wiley, 1991.

39. D. G. Dudley, *Mathematical Foundations of Electromagnetic Theory*. NY, USA: IEEE Press, 1994.

40. J. A. DeSanto, *Scalar Wave Theory: Green's Functions and Applications*. NY, USA: Springer, 1992.

41. D. Bouche, F. Molinet and R. Mittra, *Asymptotic Methods in Electromagnetics*. NY, USA: Springer, 1994.

42. N. Bleistein and R. A. Handelsman, *Asymptotic Expansions of Integrals*. NY, USA: Dover, 1986.

43. R. Wong, *Asymptotic Approximation of Integrals*. NY, USA: Academic Press, 1989.

44. V. M. Babich and V. S. Buldyrev, *Asymptotic Methods in Short-Wavelength Diffraction Theory*. Oxford, UK: Alpha Science International, 2009.

45. W. LePage, *Complex Variables and Laplace Transform for Engineers*. NY, USA: Dover, 1980.

46. M. J. Ablowitz and A. S. Fokas, *Complex Variables: Introduction and Applications*. NY, USA: Camridge University Press, 1997.

47. K. A. Michalski and J. R. Mosig, "Multilayered Media Green's Functions in Integral Equation Formulations," (invited paper), *IEEE Trans. Antennas Prop.*, vol. 45, no. 3,pp. 508-519, March 1997.

48. Y. L. Chow, J. J. Yang, D. G. Fang and G. E. Howard, "A Closed-Form Spatial Green's Function for the Thick Microstrip Substrate," *IEEE Trans. Microwave Theory Tech.*, vol. 39, no. 3, pp. 588-592, March 1991.

49. G. Dural and M. I. Aksun, "Closed Form Green's Functions for General Sources and Stratified Media," *IEEE Trans. Microwave Theory. Tech.*, vol. 43, no. 7, pp. 1545-1552, July 1995.

50. J. R. Mosig and A. A. Melcon, "Green's Functions in Lossy Layered Media: Integration Along Imaginary Axis and Asymptotic Behavior," *IEEE Trans. Antennas Prop.*, vol. 51, no. 12, pp. 3200-3208, December 2003.

51. Y. Ge and K. P. Esselle, "New Closed-Form Green's Functions for Microstrip Structures - Theory and Results," *IEEE Trans. Microwave Theory. Tech.*, vol. 50, no. 6, pp. 1556-1560, June 2002.

52. L. Tsang and B. Wu, "Electromagnetic Fields of Hertzian Dipoles in Layered Media of Moderate Thickness Including the Effects of All Modes," *IEEE Antennas and Wireless. Prop. Lett.*(AWPL), vol. 6, pp. 316-319, 2007.

53. B. Wu, L. Tsang and C. J. Ong, "Fast All Modes (FAM) Method Combined with NMSP for Evaluating Saptial Domain Layered Media Green's Function of Moderate Thickness," *Microwave and Optical Technology Letters* (MOTEL), vol. 49, no. 12, pp. 3112-3118, May 20, 2007.

54. B. Wu and L. Tsang, "Fast Computation of Layered Medium Green's Function of Multilayered and Lossy Medium Using Fast All-Poles Method and Numerical Modified Steepest Descent Path Method," *IEEE Trans. Microwave Theory Tech.*, vol. 56, no. 6, pp. 1446-1454, June 2008.

55. D. R. Jackson and N. Alexopoulos, "An Asymptotic Extraction Technique for Evaluating Sommerfeld-type Integrals," *IEEE Trans. Antennas Prop.*, vol. 34, no. 12, pp. 1467-1470, December 1986.

56. P. B. Katehi and N. G. Alexopoulos, "Real Axis Integration of Sommerfeld Inetgrals," *Jour. Math. Phys.*, vol. 24, no. 3, pp. 527-533, March 1983.

57. K. A. Michalski, "Extrapolation Methods for Sommerfeld Integral Tails," (invited review paper), *IEEE Trans. Antennas Prop.*, vol. 46, no. 10, pp. 1405-1418, October 1998.

58. M. Yuan and T. K. Sarkar, "Computation of Sommerfeld Integral Tails Using the Matrix Pencil Method," *IEEE Trans. Antennas Prop.*, vol. 54, no. 4, pp. 1358-1362, April 2006.

59. T. K. Sarkar and O. Pereira,"Using the Matrix Pencil Method to Estimate the Parameters of a Sum of Complex Exponentials," *IEEE Antennas and Prop. Mag.*, vol. 37, no. 1, pp. 48-55, February 1995.

60. I. S. Gradshteyn and I. M. Ryzhik, *Tables of Integrals, Series and Products* (6th ed.), A. Jeffrey and D. Zwillinger (eds.). NY, USA: Academic Press, 2000.

61. P. K. Kythe and M. R. Schäferkoter, *Handbook of Computational Methods for Integration*. Boca Raton, FL, USA: Chapman & Hall/CRC, 2005.

62. G. E. Roberts and H. Kaufman, *Table of Laplace Transforms*. Philadelphia, USA: W. B. Saunders & Co., 1966.

63. S. Barkeshli, P. H. Pathak and M. Marin, "An Asymptotic Closed-Form Microstrip Surface Green's Function for the Efficient Moment Method Analysis of Mutual Coupling in Microstrip Antennas," *IEEE Trans. Antennas Prop.*, vol. 38, no. 9, pp. 1374-1383, September 1990.

64. M. Marin and P. H. Pathak, "An Asymptotic-Closed Form Representation for the Grounded, Double-Layer Surface Green's Function," *IEEE Trans. Antennas Prop.*, vol. 40, no. 11, pp. 1357-1366, November 1992.

65. S. Barkeshli and P. H. Pathak, "Radial Propagation and Steepest Descent Path Integral Representations of the Planar Microstrip Green's Function," *Radio Science*, vol. 25, no. 2, pp. 161-174, March-April 1990.

66. D. G. Fang, J. J. Yang and G. Y. Delisle, "Discrete Complex Image Theory for Horizontal Electric Dipoles in a Multilayered Medium," *Proc. IEE*, Part H, vol. 135, no. 5, pp. 297-303, October 1988.

67. M. Yuan, T. K. Sarkar and M. Salazar-Palma, "A Direct Discrete Complex Image Method From the Closed-Form Green's Functions in Multilayered Media," *IEEE Trans. Antennas Prop.*, vol. 54, no. 3, pp. 1025-1032, March 2006.

68. M. Yuan, Y. Zhang, A. De, Z. Ji and T. K. Sarkar, "Two-Dimensional Discrete Complex Image Method (DCIM) for Closed Form Green's Function of Arbitrary 3D Structures in General Multilayered Media," *IEEE Trans. Antennas Prop.*, vol. 56, no. 5, pp. 1350-11357, May 2008.

69. E. Simsek, Q. H. Liu and B. Wei, "Singularity Subtraction for Evaluation of Green's Function for Multilayered Media," *IEEE Trans. Microwave Theory Tech.*, vol. 54, no. 1, pp. 216-225, January 2006.

70. M. Ayatollahi and S. Safavi-Naini, "A New Representation of the Green's Function for the Multilayer Media Based on Plane Wave Expansion," *IEEE Trans. Antennas Prop.*, vol. 52, no. 6, pp. 1548-1557, June 2004.

71. X. Di and K. E. Gilbert, "An Exact Laplace Transform Formulation of a Point Source Above a Ground Surface," *Journal of the Acoustical Society of America*, vol. 93, no. 2, pp. 714-720, February 1993.

72. K. Sarabandi, M. D. Casciato and I. S. Yoh, "Efficient Calculation of Radiation Fields Radiating Above an Impedance Surface," *IEEE Trans. Antennas Prop.*, vol. 50, no. 9, pp. 1222-1235, September 2002.

73. I. S. Koh and J. G. Yook, "Exact Closed-Form Expression of a Sommerfeld Integral for the Impedance Plane Problem," *IEEE Trans. Antennas and Prop.*, vol. 54, no. 9, pp. 2568-2576, September 2006.

74. M. Marin, S. Barkeshli and P. H. Pathak, "On the Location of Proper and Improper Surface Wave Poles for the Grounded Dielectric Slab," *IEEE Trans. Antennas and Prop.*, vol. 38, no. 4, pp. 570-573, April 1990.

75. S. A. Teo, M. S. Leong, S. T. Chew, and B. L. Ooi, "Complete Location of Poles for Thick Lossy Grounded Dielectric Slab," *IEEE Microwave Theory Tech.*, vol. 50, no. 2, pp. 440-445, January 2002.

76. Y. Wang, B. L. Ooi and M. S. Leong, "An Efficient and Fast Approach for Surface Wave Pole Extraction in a Two Layered Microstrip Geometry," *Microwave and Optical Technology Letters* (MOTEL), vol. 41, no. 4, pp. 253-258, May 20, 2004.

77. M. J. Neve and R. J. Paknys, "A Technique for Approximating Surface- and Leaky-Wave Poles for a Lossy Dielectric Slab," *IEEE Trans. Antennas Prop.*, vol. 54, no. 1, pp. 115-120, January 2006.

78. H. Rogier and D. V. Ginste, "A Fast Procedure to Accurately Determine Leaky Wave Modes in Multilayerd Planar Structures," *IEEE Trans. Microwave Theory Tech.*, vol. 56, no. 6, pp. 1413-1422, June 2008.

79. J. Hu, H-X Zhou, Z. Song and W. Hong, "Locating all the Modes of Green's Function for a Three-Layered Medium based on the Path Tracking Algorithm", *IEEE Trans. Antennas Prop.*, vol. 57, no. 8, pp. 2315-2322, August 2009.

80. L. B. Felsen, F. Akelman and L. Svegi, "Wave Propagation Inside a Two-Dimensional Perfectly Conducting Parallel-Plate Waveguide: Hybrid Ray-Mode Techniques and Their Visualizations," *IEEE Antennas and Prop. Mag.*, vol. 46, no. 6, pp. 69-89, December 2004.

81. L. B. Felsen, "Progressive and Oscillatory Waves for Hybrid Synthesis of Source Excited Propagation and Diffraction," *IEEE Trans. Antennas and Prop.*, vol. 32, no. 8, pp. 775-796, August 1984.

82. A. Kamel and L. B. Felsen, "On the Ray Equivalent of a Group of Modes," *Journal of the Acoustical Society of America* (JASA), vol. 71, no. 6, pp. 1445-1452, June 1982.

83. L. B. Felsen, "Hybrid Ray-Mode Fields in Inhomogeneous Waveguides and Ducts," *Journal of the Acoustical Society of America* (JASA), vol. 69, no. 2, pp. 352-361, February 1981.

84. L. B. Felsen, "Novel Ways of Tracking Rays," *Jour. Opt. Soc. Am.* (JOSA), ser. A, vol. 2, no. 6, pp. 954-963, June 1985.

85. L. Carin and L. B. Felsen, "Time Harmonic and Transient Scattering by Finite Periodic Flat Strip Arrays:Hybrid(ray)-(Floquet Mode)-MoM Algorithm," *IEEE Trans. Antennas and Prop.*, vol. 41, no. 4, pp. 312-321, April 1993.

86. N. M. Temme, "Uniform Asymptotic Expansions of Integrals: A Selection of Problems," *Jour. Comput. and Appl. Math.*, vol. 65, pp. 395-417, 1995.

87. A. Ciarkowski, "Uniform Asymptotic Expansion of a Integral with a Saddle Point, Pole and a Branch Point," *Proc. Roy. Soc. Lond.*, ser. A, vol. 426, no. 1871, pp. 273-286, December 1989.

88. M. V. Berry, "Uniform Asymptotic Smoothing of Stokes's Discontinuities," *Proc. Roy. Soc. Lond.*, ser. A, vol. 422, no. 1862, pp. 7-21, March 1989.

89. M. V. Berry, "Waves Near Stokes Lines," *Proc. Roy. Soc. Lond.*, ser. A, vol. 426, no. 1873, pp. 265-280, February 1990.

90. B. Y. Sternin and V. E. Shatalov, *Borel-Laplace Transform and Asymptotic Theory: Introduction to Resurgent Analysis*. Boca-Raton, FL, USA: CRC Press, December 1995.

91. Olivier Vallée and Manuel Soares, *Airy Functions and its Applications to Physics*. NJ, USA: World Scientific, 2004.

92. Yu. A. Kravtsov, *Geometrical Optics in Engineering Physics*. Middlesex, UK: Alpha Science International, Ltd., 2005.

93. I. Andronov, D. Bouche & F. Molinet, *Asymptotic and Hybrid Methods in Electromagnetics*. London, UK: IEE Press, 2005.

94. R. B. Dingle, *Asymptotic Expansions: Their Derivation and Interpretation*. London, UK: Academic Press, 1973.

95. M. V. Berry and C. J. Howls, "Hyperasymptotics for Integrals with Saddles," *Proc. Roy. Soc. Lond.*, ser. A, vol. 434, pp. 657-675, 1991.

96. C. J. Howls, "Hyperasymptotics for Integrals with Finite Endpoints," *Proc. Roy. Soc. Lond.: Mathematical and Physical Sciences*, ser. A, vol. 439, no. 1906, pp. 373-396, Nov. 1992.

97. W. G. C. Boyd, "Error Bounds for the Method of Steepest Descents," *Proc. Roy. Soc. Lond.: Mathematical and Physical Sciences*, ser. A, vol. 440, no. 1910, pp. 493-518, Mar. 1993.

98. J. P. Boyd, "The Devil's Invention: Asymptotic, Superasymptotic and Hyperasymptotic Series," *Acta Applicande Mathematicae*, vol. 56, pp. 1-98, 1999.

99. R. B. Paris and D. Kaminski, *Asymptotics and Mellin-Barnes Integrals*. Cambridge, UK: Cambridge University Press, 2001.

100. R. Borghi, "Joint Use of the Weniger Transformation and Hyperasymptotics for Accurate Asymptotic Evaluation of a Class of Saddle-Point Integrals," *Physical Review E*, vol. 78, pp. 026703-1 to 11, August 2008.

Appendix A

CONVERSION OF TWO-DIMENSIONAL SPECTRAL INTEGRALS TO SOMMERFELD FORMS

Shaun Walker

In this appendix, the conversion of the two-dimensional plane-wave spectral (PWS) integral from Ref. [A1, p. 188, Eq. 4-124] is converted to the well-known Sommerfeld identity. Following the Sommerfeld identity, some algebraic manipulations are further performed to obtain the desired relationships for evaluating the "tail" part of the Sommerfeld integral in exact, closed form. These details are included in this appendix. The PWS spectral integral reads

$$\frac{e^{-jkr}}{r} = \frac{1}{2\pi j} \int\limits_{-\infty}^{+\infty}\int\limits_{-\infty}^{+\infty} \frac{e^{-jz\sqrt{k^2-k_x^2-k_y^2}}}{\sqrt{k^2-k_x^2-k_y^2}} e^{+jk_x x} e^{+jk_y y} dk_x dk_y \tag{A1}$$

The following polar transformations on the spectral and spatial variables are utilized: $k_x = \xi\cos\alpha$, $k_y = \xi\sin\alpha$ and $x = \rho\cos\phi$, $y = \rho\sin\phi$. This transformation yields $dk_x dk_y = \xi d\xi d\alpha$. The region defined by $-\infty \le (k_x, k_y) \le +\infty$ is mapped onto the region $0 \le \alpha \le 2\pi$ and $0 \le \xi \le +\infty$. Consequently Eq. (A1) reduces to the form

$$\int\limits_{-\infty}^{+\infty}\int\limits_{-\infty}^{+\infty} \frac{e^{-jz\sqrt{k^2-k_x^2-k_y^2}}}{\sqrt{k^2-k_x^2-k_y^2}} e^{+jk_x x} e^{+jk_y y} dk_x dk_y = \int\limits_{0}^{+\infty} \frac{e^{-jz\sqrt{k^2-\xi^2}}}{\sqrt{k^2-\xi^2}} \xi d\xi \int\limits_{0}^{2\pi} e^{j\xi\rho\cos(\alpha-\phi)} d\alpha \tag{A2}$$

In Eq. (A2) the following relationship for the generating function for Bessel function

$$e^{jw\cos\theta} = \sum_{m=-\infty}^{+\infty} (j)^m J_m(w) e^{+jm\theta} \tag{A3}$$

is used to perform the following reduction

$$\int\limits_{0}^{2\pi} e^{j\xi\rho\cos(\alpha-\phi)} d\alpha = \sum_{m=-\infty}^{+\infty} (j)^m J_m(\xi\rho)$$

$$\times \int\limits_{0}^{2\pi} e^{+jm(\alpha-\phi)} d\alpha \tag{A4}$$

Since

$$\int_0^{2\pi} e^{+jm(\alpha-\phi)}d\alpha = \begin{cases} 0, & \text{when } m \neq 0, \\ 2\pi, & \text{when } m = 0 \end{cases} \tag{A5}$$

it follows, using Eqs. (A5) and (A4) into Eq. (A2) that

$$\int_{-\infty}^{+\infty}\int_{-\infty}^{+\infty} \frac{e^{-jz\sqrt{k^2-k_x^2-k_y^2}}}{\sqrt{k^2-k_x^2-k_y^2}} e^{+jk_x x}e^{+jk_y y}dk_x dk_y = 2\pi \int_0^{+\infty} \frac{e^{-jz\sqrt{k^2-\xi^2}}}{\sqrt{k^2-\xi^2}}\xi J_0(\xi\rho)d\xi \tag{A6}$$

Next, it follows readily from Eqs. (A6) and (A1) the well-known Sommerfeld identity

$$j\frac{e^{-jkr}}{r} = \int_0^{+\infty} \xi J_0(\xi\rho)\frac{e^{-jz\sqrt{k^2-\xi^2}}}{\sqrt{k^2-\xi^2}}d\xi \tag{A7}$$

When $\xi > k$, then $\sqrt{k^2-\xi^2} \Longrightarrow -j\sqrt{\xi^2-k^2}$ in Eq. (A7). In both Eqs. (A1) and (A7), $r=\sqrt{x^2+y^2+z^2}=\sqrt{\rho^2+z^2}$. With the above changes in Eq. (A7) and alternate form of the Sommerfeld identity reads

$$\frac{e^{-jkr}}{r} = \int_0^{+\infty} \xi J_0(\xi\rho)\frac{e^{-z\sqrt{\xi^2-k^2}}}{\sqrt{\xi^2-k^2}}d\xi \tag{A8}$$

Eq. (A8) is known as the classical form. In Eqs. (A1), (A7), and (A8) it is assumed that $z \geq 0$ for the integrals to converge. Next we derive the identities/relationships used for calculating the "tail" part of the Sommerfeld integral along real axis.

Differentiating both sides of Eq. (A7) w.r.t ρ, and using the relationships

$$\frac{d}{d\rho}[J_0(\xi\rho)] = -\xi J_1(\xi\rho) \qquad \frac{d}{d\rho}\left[\frac{e^{-jk\sqrt{\rho^2+z^2}}}{\sqrt{\rho^2+z^2}}\right] = -\frac{\rho e^{-jkr}}{r^3}[1+jkr]$$

we obtain

$$\int_0^{+\infty} \xi^2 J_1(\rho\xi)\frac{e^{-jz\sqrt{k^2-\xi^2}}}{\sqrt{k^2-\xi^2}}d\xi = j\rho\frac{e^{-jkr}}{r^3}(1+jkr) \tag{A9}$$

In Eq. (A9), it maybe recalled that $r=\sqrt{\rho^2+z^2}$. Next, we differentiate Eq. (A9) w.r.t z, and substitute the following relationship

$$\frac{d}{dz}\left[j\rho\frac{e^{jkr}}{r^3}(1+jkr)\right] = \frac{-j\rho z e^{-jkr}}{r^5}[3+3jkr-(kr)^2]$$

to obtain the following

$$\rho z \frac{e^{-jkr}}{r^5}[3+3jkr-(kr)^2] = \begin{cases} \int\limits_0^{+\infty} \xi^2 J_1(\xi\rho)e^{-jz\sqrt{k^2-\xi^2}}d\xi; & \text{when } \xi \leq k, \\ \int\limits_0^{+\infty} \xi^2 J_1(\xi\rho)e^{-z\sqrt{\xi^2-k^2}}d\xi; & \text{when } \xi \geq k \end{cases} \tag{A10}$$

A slightly different variant of Eq. (A10) was used in Ref. [A2, Eq. A4]. This form can also be obtained from Ref. [A3, p. 694, Eq. 6.623.2] and reads

$$\int\limits_0^{+\infty} \xi^2 J_1(\xi\rho)\exp(-\xi z)d\xi = \frac{3\rho z}{r^5}. \tag{A11}$$

This form can be used to calculate a different, final asymptotic form for the slab function $\overline{\mathscr{F}}_{zx}^{\,m}(\xi \geq \xi_A^m)$ given explicitly in Eq. (13). The form in Eq. (A11) can be obtained as a special case from Eq. (A10) by setting $k = 0$ therein for $\xi \geq k$ case. The accuracy of using both forms in numerical calculation of Sommerfeld integral tails, however, remains an open question.

REFERENCES

A1. W. C. Chew, M. S. Tong and B. Hu, *Integral Equation Methods for Electromagnetic and Elastic Waves*. USA: Morgan & Claypool, 2009.

A2. K. A. Michalski and J. R. Mosig, "Multilayered Media Green's Functions in Integral Equation Formulations," (invited paper), *IEEE Trans. Antennas Prop.*, vol. 45, no. 3, pp. 508-519, March 1997.

A3. I. S. Gradshteyn and I. M. Ryzhik, *Tables of Integrals, Series and Products* (6th ed.), A. Jeffrey and D. Zwillinger (eds.). NY, USA: Academic Press, 2000.

This page intentionally left blank.

Appendix B

ADDITIONAL RESULTS FOR THE INTEGRAND IN THE G_{ZX} GREEN'S FUNCTION FOR SINGLE LAYER PEC-BACKED SUBSTRATE
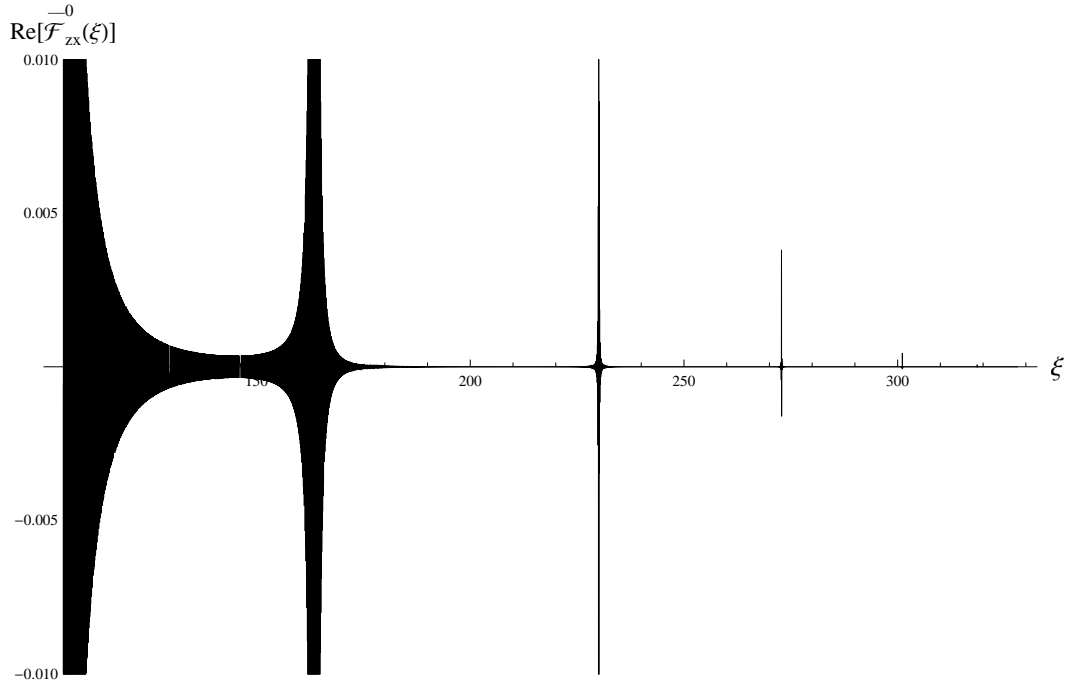

Fig. B1 — Behavior of integrand in Eq. (3) for observation point in air (region # 0) in Fig. 3 for $\rho = 1000\lambda$, $z = +\frac{\lambda}{2}$, $\tan\delta = 0.0001$, $d = \lambda$ and $|\varepsilon_{r1}| = 9.8$
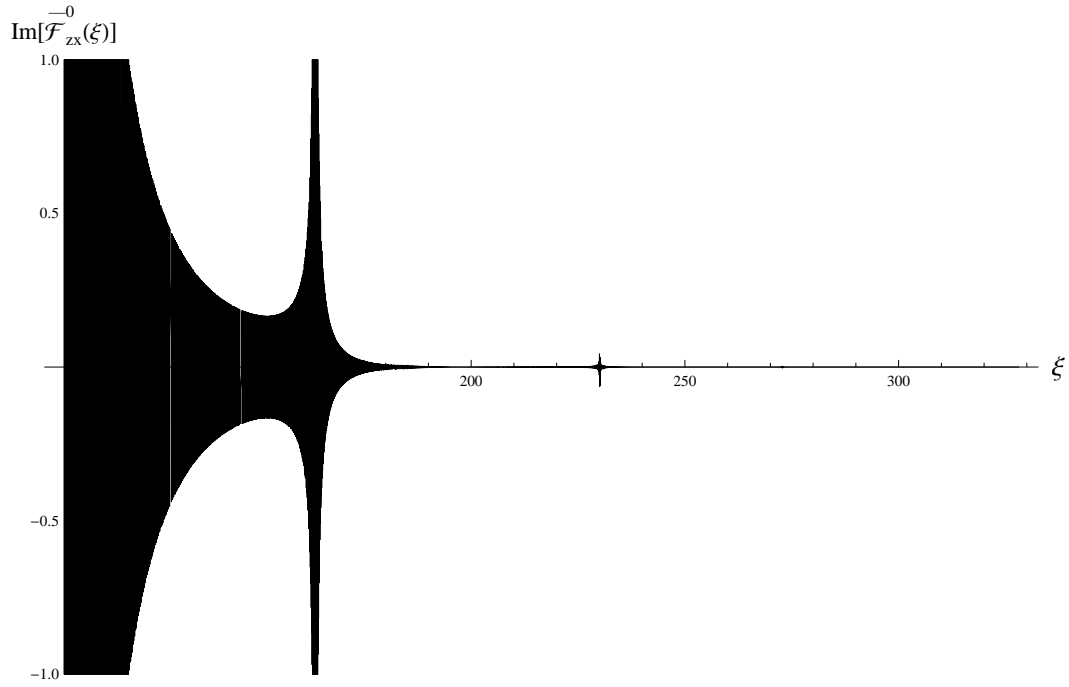
Fig. B2 — Behavior of integrand in Eq. (3) for observation point in air (region # 0) in Fig. 3 for
$\rho = 1000\lambda$, $z = +\frac{\lambda}{2}$, $\tan\delta = 0.0001$, $d = \lambda$ and $|\varepsilon_{r1}| = 9.8$
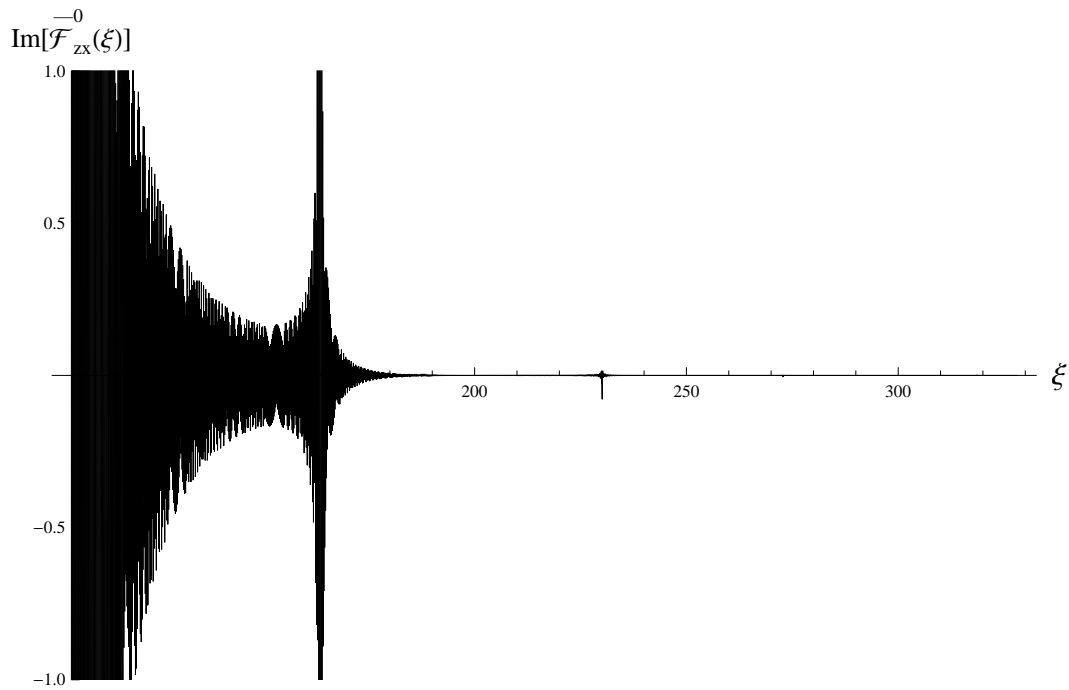

Fig. B3 — Behavior of integrand in Eq. (3) for observation point in air (region # 0) in Fig. 3. All data
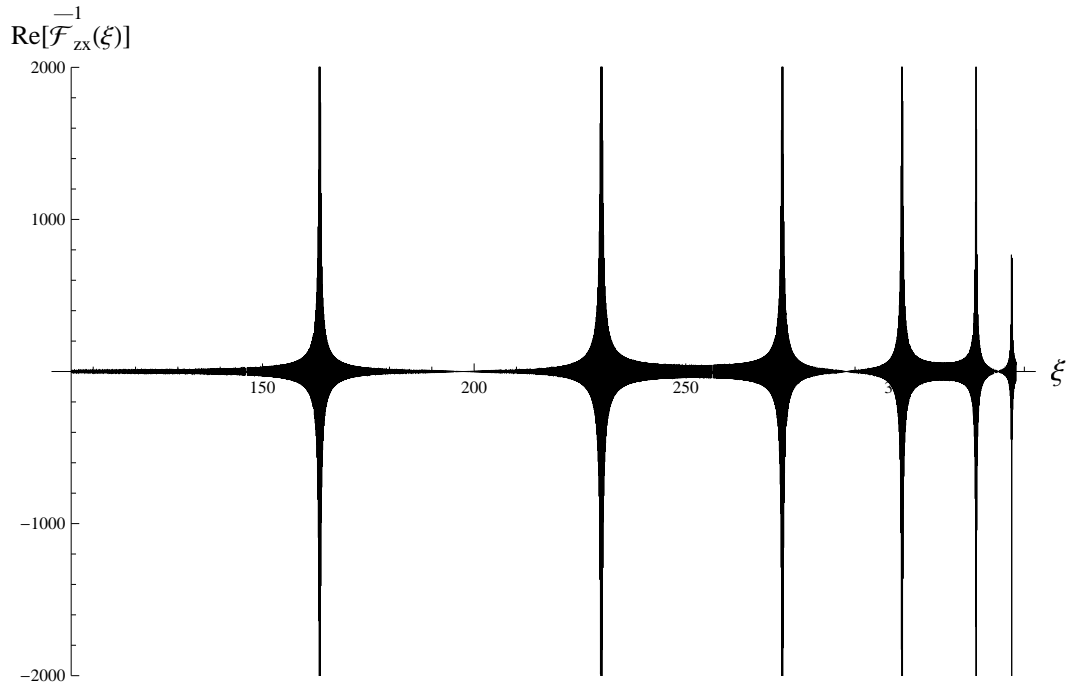same as in Fig. B2, except for the lossless case $\tan\delta = 0$.

Fig. B4 — Behavior of integrand in Eq. (4) for observation point in substrate (region # 1) in Fig. 3
for $\rho = 1000\lambda$, $z = -\frac{\lambda}{2}$, $\tan\delta = 0.0001$, $d = \lambda$ and $|\varepsilon_{r1}| = 9.8$
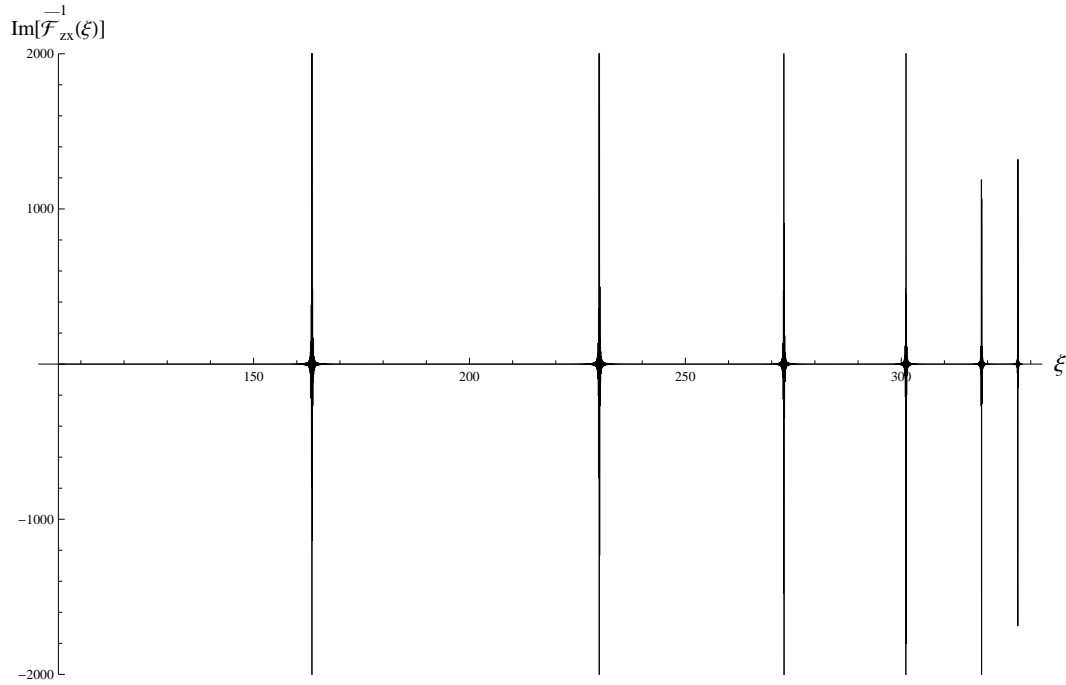

Fig. B5 — Behavior of integrand in Eq. (4) for observation point in substrate (region # 1) in Fig. 3
for $\rho = 1000\lambda$, $z = -\frac{\lambda}{2}$, $\tan\delta = 0.0001$, $d = \lambda$ and $|\varepsilon_{r1}| = 9.8$.

Fig. B6 — Behavior of the integrand in the Sommerfeld integral for the $G_{zx}(\rho, z, \phi)$ Green's function in Eqs. (32) and (33). Here $d = \lambda$, $\rho = 1000\lambda$, $z = -\frac{\lambda}{2}$, $\tan \delta = 0$, and $|\varepsilon_{r1}| = 9.8$. The observation point is inside the substrate. The imaginary part of the integrand identically vanishes.
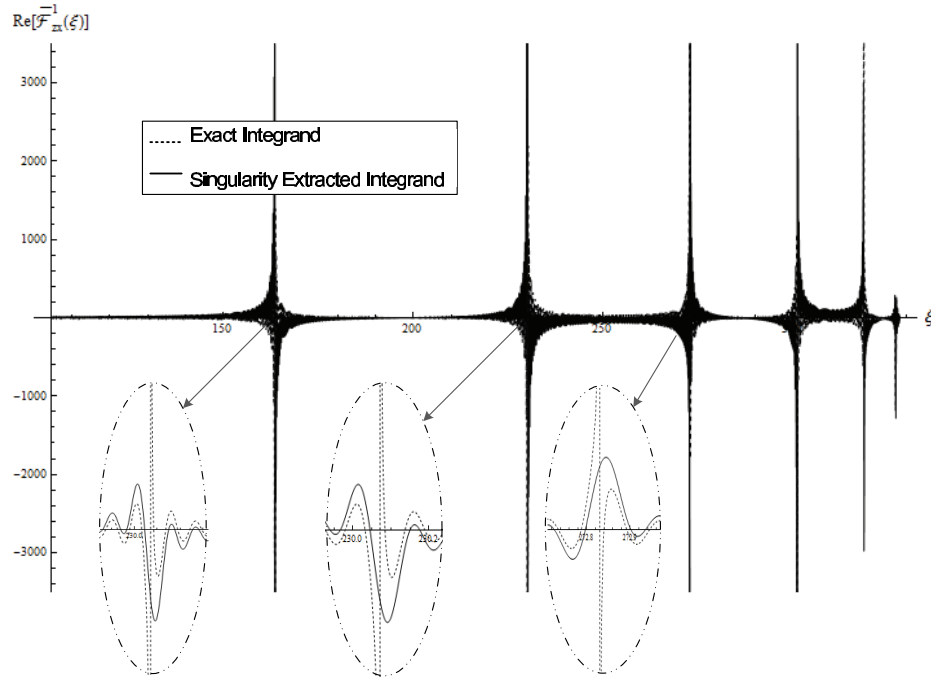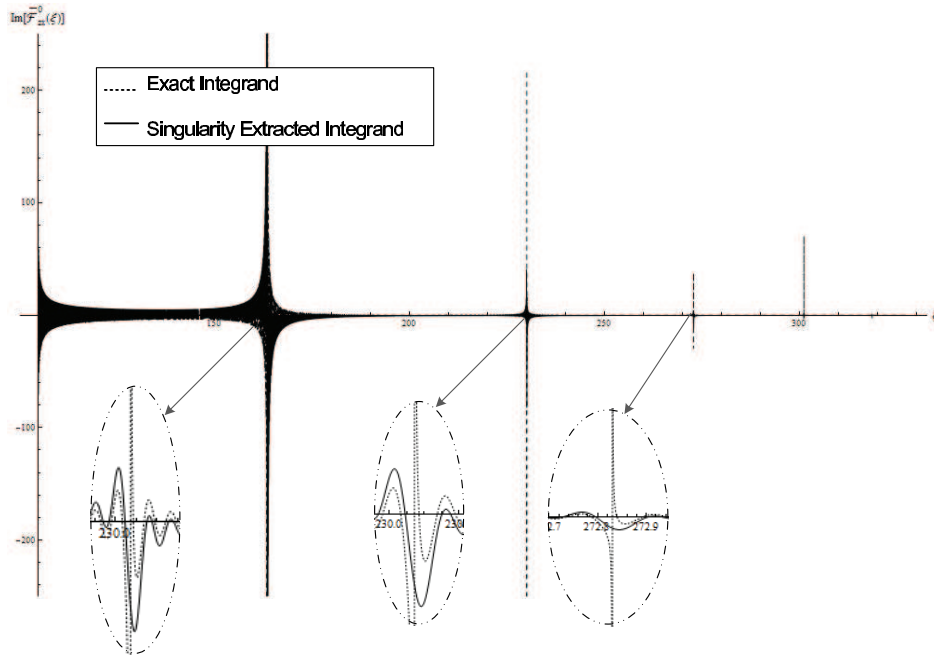

Fig. B7 — Behavior of the integrand in the Sommerfeld integral for the $G_{zx}(\rho, z, \phi)$ Green's function in Eqs. (32) and (33). Here $d = \lambda$, $\rho = 1000\lambda$, $z = +\frac{\lambda}{2}$, $\tan \delta = 0$, and, $|\varepsilon_{r1}| = 9.8$. The observation point is outside the substrate. The real part of the integrand identically vanishes.

Appendix C

MATHEMATICA SCRIPTFILE (CODE LISTING) FOR PROPER SURFACE TM WAVE POLE LOCATIONS

Shaun Walker

```
(*
List of physcal constants
=====================================
c0 – Speed of light in vacuum
f – operating frequency
lam – wavelength
k0 – free-space wavenumber
tand – dielectric loss
er – relative permittivity of slab
d – thickness of slab
k1 – wavenumber in slab
=====================================
OtherVariables
=====================================
numZEROS     – number of zero locations of the denominator
in the integrand (i.e. number of zeros of DTM)
orderOfTS    – order of the Taylor series used
correctZEROS – this is used inside of a loop to count the
number of correct zeros found by the algorithm, when variable
is equal to numZEROS then this means that all roots where found
zeroLIST     – list of zeros that contains the zeros of the
Taylor series that correspond to the proper surface wave poles
testROOTS    – a list of length orderOfTS, it contains roots
taken from the zeros of the truncated Taylor polynomial which
include the effects of all modes, these roots will be tested to see
which ones correspond to the surface wave poles
=====================================
Built-in Mathematica subroutines
=====================================
Sqrt[]     – takes the square root of its argument
Floor[]    – truncates the decimal portion of a real number
Re[]       – takes the real part of a complex number
Im[]       – takes the imaginary part of a complex number
Abs[]      – takes the absolute values of a complex number
NRoot[]    – numerically finds roots of a polynomial
```

```
FindRoot[] - numerically finds root of a user defined function
=====================================
Mathematica Constants
=====================================
Pi  - pi=3.1415459045
I   - square root of -1
*)
(* Subroutine used to evaluate the mode function *)
DTM[d_, er_, k0_, v_] := Module[{D},
D = er*v*Cos[Sqrt[(d*k0)^2*(er-1)-v^2]]
- Sqrt[(d*k0)^2*(er-1)-v^2]*Sin[Sqrt[(d*k0)^2*(er-1)-v^2]];
  D]
(* define constants *)
c0    = 2.997924*10^8;
f     = 5*10^9;
lam   = c0/f;
k0    = 2 Pi/lam;
tand  = 0.0001;
er    = 9.8 (1 - I tand);
d     = lam;
k1    = Sqrt[er] k0;
numZEROS     = Floor[d k0 Sqrt[Re[er]-1]/Pi]+1;
orderOfTS    = 0;
correctZEROS = 0;
(*
while the number of correct zeros found by the algorithm is less
than the number of zeros of DTM due to proper surface wave poles,
then keep looking
*)
While[correctZEROS < numZEROS,
(* reset the number of correct zeros found & list of zeros *)
correctZEROS = 0;
zeroLIST = Table[0, {i, numZEROS}];
(*
increase the order of the Taylor series, and insure that the order
of the Taylor series taken will be greater than the number of
surface wave poles that need to be found
*)
If[(orderOfTS++) < numZEROS, orderOfTS = numZEROS];
(* get Taylor series of DTM and find all zeros of the series *)
testROOTS = NRoots[Normal[Series[DTM[d,er,k0,v],{v,0,orderOfTS}]]
==0,v];
(* for each of the test roots found from the truncated Taylor series *)
For[q = 1, q <= Length[testROOTS], q++,
(* gets the next test root *)
If[orderOfTS > 1, vr = testROOTS[[q]][[2]], vr = testROOTS[[1]]];
```

```
(* evaluate DTM for test root*)
test = DTM[d, er, k0, vr];
(* is the test close enough to zero and is this a proper SWP ? *)
If[Abs[test]<=1 && Re[vr]>=0 && Re[vr]<=d k0 Sqrt[Re[er]-1] &&
Im[vr]<=0,
(* then increment the number of correct zeros that have been found *)
correctZEROS++;
(* add the test root to the list of correct zeros found *)
zeroLIST[[correctZEROS]] = vr
];
]
];
(* use the inital guess for each root to find the exact root *)
exactZEROS = FindRoot[DTM[d,er,k0,v],{v,zeroLIST},AccuracyGoal->10];
exactZEROS = Sqrt[(exactZEROS[[1]][[2]]/(d k0))^2 + 1];
Print["Number of zeros is ", numZEROS, "."]
Print["Order of the Taylor series taken is ", orderOfTS, "."];
Print["Zero locations are: ", exactZEROS];
```

This page intentionally left blank.

Appendix D

MATHEMATICA SCRIPTFILE (CODE LISTING) FOR CALCULATING THE G_{ZX} GREEN'S FUNCTION FOR PEC-BACKED SINGLE LAYER MEDIA

Shaun Walker

```
(*
There are 6 subroutines, two of these functions are for the
evaluation of the residues, and the other 4 equations are
for the calculation of Gzx.
Rp0 - Calculates the pth residue in region 0
Rp1 - Calculates the pth residue in region 1
zLessThanZero - Computation of Gzx for z<0, in Region 0
zEqualZeroR1 - Computation of Gzx for z=0 using region 1 expression
zEqualZeroR0 - Computation of Gzx for z=0 using region 0 expression
zGreaterThanZero - Computation of Gzx for z>0, in Region 1
*)
Rp0[Rho_,z_,d_,er_,k0_,Xi_] := Module[{R}, k1=Sqrt[er]*k0;
Num = Xi^2 * BesselJ[1,Rho*Xi] * Sqrt[k1^2-Xi^2] *
Sin[d*(Sqrt[k1^2-Xi]^2])]* E^(-z*Sqrt[Xi^2-k0^2]);
Dp = -I*Xi*Cos[d*Sqrt[k1^2-Xi^2]]*(d+er/Sqrt[Xi^2-k0^2])
  - I*Xi*Sin[d*Sqrt[k1^2-Xi^2]] * (1+d*er*Sqrt[Xi^2-k0^2])
  /Sqrt[k1^2-Xi^2];
R=Num/Dp;
R]
Rp1[Rho_,z_,d_,er_,k0_,Xi_] := Module[{R}, k1=Sqrt[er]*k0;
Num = Xi^2*BesselJ[1,Rho*Xi] * (-I*Sqrt[Xi^2-k0^2])
    * Cos[(d-Abs[z])*Sqrt[k1^2-Xi^2]];
Dp = -I*Xi*Cos[d*Sqrt[k1^2-Xi^2]] * (d+er/Sqrt[Xi^2-k0^2])
  - I*Xi*Sin[d*Sqrt[k1^2-Xi^2]]/Sqrt[k1^2-Xi^2] *
  (1+d*er*Sqrt[Xi^2-k0^2]);
R=Num/Dp;
R]
zLessThanZero[Rho_,z_,d_,er1_,k0_,XiA_] := Module[{Integral},
k1 = Sqrt[er1]*k0;
r  = Sqrt[Rho^2+z^2];
I0toK0 = NIntegrate[Xi^2*BesselJ[1,Rho*Xi]*Sqrt[k0^2-Xi^2]
* Cos[(d-Abs[z])*Sqrt[k1^2-Xi^2]] / (er1*Sqrt[k0^2-Xi^2]
* Cos[d*Sqrt[k1^2-Xi^2]]+I*Sqrt[k1^2-Xi^2]*Sin[d*Sqrt[k1^2-Xi^2]])
- Exp[-I*Abs[z]*Sqrt[k1^2-Xi^2]]/(er1+1)),
{Xi,0,k0},
```

```
AccuracyGoal->6,
MaxRecursion->1000,
Method->{GlobalAdaptive,
MaxErrorIncreases->200000}];
IK0toK1 = NIntegrate[Xi^2*BesselJ[1,Rho*Xi]*(-I*Sqrt[Xi^2-k0^2])
* Cos[(d-Abs[z])*Sqrt[k1^2-Xi^2]] / (er1*(-I*Sqrt[Xi^2-k0^2])
* Cos[d*Sqrt[k1^2-Xi^2]]+I*Sqrt[k1^2-Xi^2]*Sin[d*Sqrt[k1^2-Xi^2]])
    - Exp[-I*Abs[z]*Sqrt[k1^2-Xi^2]]/(er1+1))
- Sum( Rp1[Rho,z,d,er1,k0,Xip[[p]]] / (Xi-Xip[[p]] , {p=1,P}),
  {Xi,k0,Re[k1]},
AccuracyGoal->6,
MaxRecursion->1000,
Method->{GlobalAdaptive,
MaxErrorIncreases->200000}]
+ Sum[ Rp1[Rho,z,d,er1,k0,Xip[[p]]]
* Log[(k1-Xip[[p]])/(Xip[[p]]-k0)]-I*Pi , {p=1,P}];
IK1toXiA = NIntegrate[Xi^2*BesselJ[1,Rho*Xi] * (-I*Sqrt[Xi^2-k0^2])
* Cos[(d-Abs[z])*(-I*Sqrt[Xi^2-k1^2])]]
/ ( er1*(-I*Sqrt[Xi^2-k0^2]) * Cos[d*(-I*Sqrt[Xi^2-k1^2])]
    + I*(-I*Sqrt[Xi^2-k1^2])*Sin[d*(-I*Sqrt[Xi^2-k1^2])] )
- Exp[-Abs[z]*Sqrt[Xi^2-k1^2]]/(er1+1),
{Xi,Re[k1],XiA},
AccuracyGoal->6,
MaxRecursion->1000,
Method->{GlobalAdaptive,MaxErrorIncreases->200000}];
Itail = 1/(er1+1) * Rho*z *(3+I*3*k1*r-(k1*r)^2)
* Exp[-I*k1*r]/r^5;
Integral = I0toK0 + IK0toK1 + IK1toXiA + Itail;
Integral]
zEqualZeroR1[Rho_,z_,d_,er1_,k0_,XiA_] := Module[{Integral},
k1=Sqrt[er1]k0;
I0toK0 = NIntegrate[(Xi^2 * BesselJ[1,Rho*Xi] * Sqrt[k0^2-Xi^2]
* Cos[d*Sqrt[k1^2-Xi^2]] / (er1*Sqrt[k0^2-Xi^2]
    *Cos[d*Sqrt[k1^2-Xi^2]]
    +I*Sqrt[k1^2-Xi^2]*Sin[d*Sqrt[k1^2-Xi^2]],
{Xi,0,k0},
AccuracyGoal->6,
MaxRecursion->1000,
Method->{GlobalAdaptive,
MaxErrorIncreases->200000}];
IK0toK1 = NIntegrate[Xi^2 * BesselJ[1,Rho*Xi] * (-I*Sqrt[Xi^2-k0^2])
* Cos[d*Sqrt[k1^2-Xi^2]] / (er1*(-I*Sqrt[Xi^2-k0^2])
* Cos[d*Sqrt[k1^2-Xi^2]] +I*Sqrt[k1^2-Xi^2]*Sin[d* Sqrt[k1^2-Xi^2]])
- Sum[ Rp1[Rho,z,d,er1,k0,Xip[[p]]] / (Xi-Xip[[p]]), {p=1,P}],
{Xi,k0,Re[k1]},
AccuracyGoal->6,
```

```
MaxRecursion->1000,
Method->{GlobalAdaptive,MaxErrorIncreases->200000}]
+ Sum[ Rp1[Rho,z,d,er1,k0,Xip[[p]]]*Log[(k1-Xip[[p]])/(Xip[[p]]-k0)]
      - I*Pi, {p=1,P} ];
IK1toXiA = NIntegrate[(Xi^2 * BesselJ[1,Rho*Xi]*(-I*Sqrt[Xi^2-k0^2])
* Cos[d*(-I*Sqrt[Xi^2-k1^2])]]/(er1*(-I*Sqrt[Xi^2-k0^2])
* Cos[d*(-I*Sqrt[Xi^2-k1^2])]+I*(-I*Sqrt[Xi^2-k1^2])
* Sin[d*(-I Sqrt[Xi^2-k1^2])]),
{Xi,Re[k1],XiA},
AccuracyGoal->6,
MaxRecursion->1000,
Method->{GlobalAdaptive,
MaxErrorIncreases->200000}];
Itail = -1/(er1+1) * (XiA^2*BesselJ[2,XiA*Rho]) / Rho;
Integral = I0toK0 + IK0toK1 + IK1toXiA + Itail;
Integral]
zEqualZeroR0[Rho_,z_,d_,er1_,k0_,XiA_] := Module[{Integral},
k1 = Sqrt[er1]k0;
I0toK0 = NIntegrate[(k0*Sech[u])^2 * BesselJ[1,Rho*(k0*Sech[u])]
* Sqrt[k1^2-(k0*Sech[u])^2] * Sin[d*Sqrt[k1^2-(k0*Sech[u])^2]]
* (-k0*Sech[u]*Tanh[u]) / (  er1*Sqrt[k0^2-(k0*Sech[u])^2]
* Cos[d*Sqrt[k1^2-(k0*Sech[u])^2]] + I*Sqrt[k1^2-(k0 Sech[u])^2]
* Sin[d*Sqrt[k1^2-(k0*Sech[u])^2]]  ),
{u,(k0 Sech[0]),(k0 Sech[k0])},
AccuracyGoal->6,
MaxRecursion->1000,
Method->{GlobalAdaptive,
MaxErrorIncreases->200000}];
IK0toK1 = NIntegrate[(Xi^2 * BesselJ[1,Rho*Xi] * Sqrt[k1^2-Xi^2]
* Sin[d*Sqrt[k1^2-Xi^2]]/(er1*(-I*Sqrt[Xi^2-k0^2])
* Cos[d*Sqrt[k1^2-Xi^2]]+I*Sqrt[k1^2-Xi^2]*Sin[d*Sqrt[k1^2-Xi^2]])
  - Sum[ Rp0[Rho,z,d,er1,k0,Xip[[p]]]/(Xi-Xip[[p]]),{p=1,P}],
{Xi,k0,Re[k1]},
AccuracyGoal->6,
MaxRecursion->1000,
Method->{GlobalAdaptive,MaxErrorIncreases->200000}]
+ Sum[Rp0[Rho,z,d,er1,k0,Xip[[p]]]*Log[(k1-Xip[[p]])/(Xip[[p]]-k0)]
-I*Pi, {p=1,P} ];
IK1toXiA = NIntegrate[(Xi^2*BesselJ[1,Rho*Xi]*(-I*Sqrt[Xi^2-k1^2])
* Sin[d*(-I*Sqrt[Xi^2-k1^2])]]/(er1(-I*Sqrt[Xi^2-k0^2])
* Cos[d*(-I*Sqrt[Xi^2-k1^2])]+I*(-I*Sqrt[Xi^2-k1^2])
* Sin[d*(-I Sqrt[Xi^2-k1^2])]),
{Xi,Re[k1],XiA},
AccuracyGoal->6,
MaxRecursion->1000,
Method->{GlobalAdaptive,MaxErrorIncreases->200000}];
```

```
Itail = -(-I/(er1+1)) * (XiA^2*BesselJ[2,XiA*Rho]) / Rho;
Integral = I0toK0 + IK0toK1 + IK1toXiA + Itail;
Integral]
zGreaterThanZero[Rho_,z_,d_,er1_,k0_,XiA_] := Module[{Integral},
k1 = Sqrt[er1]k0;
r  = Sqrt[Rho^2+z^2];
I0toK0=NIntegrate[Xi^2*BesselJ[1,Rho*Xi]*Exp[-I*z*Sqrt[k0^2-Xi^2]]
* (Sqrt[k1^2-Xi^2]*Sin[d*Sqrt[k1^2-Xi^2]]/(er1*Sqrt[k0^2-Xi^2]
* Cos[d*Sqrt[k1^2-Xi^2]]+I*Sqrt[k1^2-Xi^2]*Sin[d*Sqrt[k1^2-Xi^2]])
  + I/(er1+1)),{Xi,0,k0},AccuracyGoal->6,
MaxRecursion->1000,
Method->{GlobalAdaptive,
MaxErrorIncreases->200000}];
IK0toK1 = NIntegrate[Xi^2 *BesselJ[1,Rho*Xi]*Exp[-z*Sqrt[Xi^2-k0^2]]
* ( Sqrt[k1^2-Xi^2]*Sin[d*Sqrt[k1^2-Xi^2]]/(er1*(-I*Sqrt[Xi^2-k0^2])
* Cos[d*Sqrt[k1^2-Xi^2]]+I*Sqrt[k1^2-Xi^2]*Sin[d*Sqrt[k1^2-Xi^2]])
+ I/(er1+1) )- Sum[Rp0[Rho,z,d,er1,k0,Xip[[p]]]/(Xi-Xip[[p]]),{p=1,P}],
{Xi,k0,Re[k1]},
AccuracyGoal->6,
MaxRecursion->1000,
Method->{GlobalAdaptive,MaxErrorIncreases->200000}]
+ Sum[Rp0[Rho,z,d,er1,k0,Xip[[p]]]*(Log[(k1-Xip[[p]])/
     (Xip[[p]]-k0)]-I*Pi),{p=1,P}];
IK1toXiA = NIntegrate[Xi^2*BesselJ[1,Rho*Xi]*Exp[-z*Sqrt[Xi^2-k0^2])
*(-I*Sqrt[Xi^2-k1^2]*Sin[d*(-I*Sqrt[Xi^2-k1^2])]
/( er1*(-I*Sqrt[Xi^2-k0^2])*Cos[d*(-I*Sqrt[Xi^2-k1^2])]
+ I*(-I*Sqrt[Xi^2-k1^2])*Sin[d*(-I*Sqrt[Xi^2-k1^2])])
+ I/(er1+1)),
{Xi,Re[k1],XiA},
AccuracyGoal->6,
MaxRecursion->1000,
Method->{GlobalAdaptive,
MaxErrorIncreases->200000}];
Itail = -(I/(er1+1))*Rho*z*(3+I*3*k0*r-(k0*r)^2)*Exp[-I*k0*r]/r^5;
Integral = I0toK0 + IK0toK1 + IK1toXiA + Itail;
Integral]
Mu0=1.256637*10^-6;
Epsilon0=8.854187*10^-12;
c0=2.997924*10^8;
f=5*10^9; (* operating frequency *)
Lambda=c0/f; (* wavelength *)
k0=2*Pi/Lambda; (* free-space wavenumber *)
tanDelta=0.0001; (* dielectric loss of slab *)
er1=9.8*(1-I*tanDelta); (* relative perm. in region 1 *)
k1=k0*Sqrt[er1];  (* wavenumber in region 1 *)
d=Lambda;  (* slab thicknes *)
```

```
XiA=Re[k1];  (* breakpoint *)
Rho = 100*Lambda;
Phi = 0;
(* zeros for tand=0.0001, er1=9.8, and d=1*Lambda *)
Xip = k0*{1.560465260348978-I*0.00028915689324715506,
2.1955007373508435-I*0.00021901803692256456,
2.6035344541354384-I*0.00018677914895957531,
2.8733530563113567-I*0.00016999491295840665,
3.040363182302955- I*0.0001610010843909009,
3.1206058917706754-I*0.00015700389753638654
};
(*number of SWP is equal to the length of the list of
zeros of Xip *)
P = Length[Xip];
(*list of z values used to compute Gzx *)
zLIST={-1,-.95,-0.9,-.85,-.8,-.75,-.7,-.65,-.6,-.55,-.5,-.45,-.4,
-.35,-.3,-.25,-.2,-.15,-.1,-.08,-.06,-.04,-.02,-.01,0,.01,.02,.04,
.06,.08,.1,.15,.2,.25,.3,.4,.5,.6,.7,.8,.9,1,1.25,1.5,1.75,2,2.5,
3,3.5,4,4.5,5,5.5,6,6.5,7,7.5,8,8.5,9,9.5,10} * Lambda;
(* number of times that Gzx needs to be computed *)
zLENGTH=Length[zLIST];
(* initialize Gzx to all zeros *)
GzxA=Table[0,{i,zLENGTH+1}];
(* for each values of z *)
For[m=1,m<=zLENGTH,m++, Print["Loop ",m," of ",zLENGTH];
z = zLIST[[m]]; (* get next value of z *)
If[z<0,
GzxA[[m]] = (-I*er1)/(2*Pi*k0^2) * Cos[Phi]
* zLessThanZero[Rho,z,d,er1,k0,XiA];
];
If[z==0,
GzxA[[m]] = (-I er1)/(2*Pi*k0^2) * Cos[Phi]
* zEqualZeroR1[Rho,z,d,er1,k0,XiA];
GzxA[[m+1]] = I/(2*Pi*k0^2) * Cos[Phi]
 * zEqualZeroR0[Rho,z,d,er1,k0,XiA];
];
If[z>0,
GzxA[[m+1]] = I/(2*Pi*k0^2) * Cos[Phi]
 * zGreaterThanZero[Rho,z,d,er1,k0,XiA];
]
]//Timing
```